Enclosure 3

CALIBRATION AND PREDICTION OF PNEUMATIC RESPONSE AT YUCCA MOUNTAIN, NEVADA USING THE UNSATURATED ZONE FLOW MODEL

C.F. Ahlers, C. Shan, C. Haukwa,
A.B.J. Cohen, G.S. Bodvarsson

August 1996

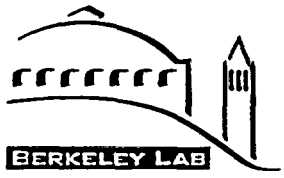

ERNEST ORLANDO LAWRENCE
BERKELEY NATIONAL LABORATORY
EARTH SCIENCES DIVISION
1 Cyclotron Road, Mailstop 90-1116
Berkeley, CA 94720

Table of Contents

List of Figures

List of Tables

1. Introduction

Characterization of gas flow at Yucca Mountain, Nevada is important. Some radionuclides, that are produced by spent fuel, are present and can be transported in the gas phase. The thermal response of the system to heating from a repository depends significantly on gas circulation. Gas outflow may occur during heating from the repository, and near surface temperature change could alter the ecosystem.

In response to the NRC, the DOE initiated a pneumatic monitoring program. Boreholes are instrumented to monitor the pneumatic response in the subsurface to barometric pressure fluctuations at the surface of the mountain and in the ESF. Barometric pressure fluctuations occur due to daily changes in temperature and due to passing weather systems. Monitoring of pneumatic response to the surface signal allows estimation of vertical pneumatic diffusivity. With the response to the barometric signal in the ESF also monitored, horizontal pneumatic diffusivity can also be estimated. Very good quality data has been obtained from boreholes instrumented and monitored by the USGS (Rousseau and Patterson, 1996a). Nye County has also instrumented and monitored boreholes.

Successful data analysis has been performed with the unsaturated zone flow model. One and two-dimensional simulations are used as the first step of pneumatic characterization. Use of three-dimensional, site-scale simulations allows fully three-dimensional characterization. Blind predictions using recorded surface signals have been performed with calibrated simulations to build confidence in the models. The pneumatic characterization has given much useful information about the pneumatic diffusivity of fractures, effects of faults as pneumatic pathways, and the role of the PTn.

The objectives of this work are to

1) analyze the pneumatic data in order to determine pneumatic diffusivity,
2) determine the roles of faults with respect to pneumatics,
3) determine global gas flow patterns and characteristics at Yucca Mountain,
4) develop a predictive history for pneumatic response in order to build comfidence in the models of pneumatics at Yucca Mountain, and
5) provide the basis for integrating the three-dimensional model of liquid flow in the unsaturated zone with a calibrated model of gas flow.

Conditions near the ESF due to tunnel ventilation are also investigated with respect to moisture flow from the tunnel walls.

1.1. QA status of data used in preparation of this report.

Data used for this report include non-Q borehole logs that are used to create a three-dimensional model of the lithostratigraphy of Yucca Mountain (Bandurraga et al., 1996a). All but one of the models used to perform the numerical simulations in this report are partially based on that three-dimensional lithostratigraphic

model. The two-dimensional model of SD-12 exclusively uses borehole log data from SD-12 which is a Q borehole log. Conclusions based on numerical simulations at all other boreholes are considered non-Q until such time as the borehole logs used in creation of the three-dimensional model of the lithostratigraphy are Q. For the purpose of dividing conclusions in this report into Q and non-Q, the QA status fo the lithostratigraphic model will not be addressed. It is assumed that this model will be Q at some future time. This is done so that conclusions made with Q and non-Q pneumatic monitoring data may be easily and succinctly separated. Similarly conclusions based on pneumatic data which has been collected under a YMP approved QA program but which has not, at the time of writing this report, been officially submitted to the program will be classified as Q. All but a small portion of the monitoring data from NRG-6 and NRG-7a fall into this catagory. Conclusions based on pneumatic monitoring data not collected under a YMP approved QA program will be classified as non-Q. The QA status of data and reports and conclusions based on these data and reports should not be taken as representative of their scientific validity. Table 1.1.1 summarizes the QA status of data used in preparation of this report.

Table 1.1.1
QA status and data tracking numbers (DTN) for data used in preparation of this report.

DTN & ACCN	Explanation	QA
GS950508312232.001 N/A	Rousseau et al., In situ borehole instrumentation and monitoring data (October 25, 1994 through April 12, 1995) USW NRG-7a and USW NRG-6, 1995.	Y
MO9506NYE-CNTY.001 N/A	In situ borehole monitoring data for UE-25 UZ#4, UE-25 UZ#5, USW NRG-6, USW NRG-7a, USW SD-12, USW UZ-7a, and experiment at HRF.	WS
GS950808312261.003 GS960208312261.001	Monitoring data for boreholes UE-25 NRG#4 and UE-25 ONC#1.	N
N/A N/A	Patterson, G. L., Monitoring data for borehole USW SD-9, USGS.	Y
N/A N/A	Patterson, G. L., Shut in pressure test data from UE25 NRG#5 and USW SD-7 from November 1995 through July 1996, USGS, September 1996.	WS
N/A N/A	LeCain, G. D., In-situ pneumatic testing of boreholes, 1996. (NRG-7a, NRG-6)	WS
N/A N/A	LeCain, G. D., Analysis of air injection testing at boreholes USW NRG-6, USW NRG-7a, USW UZ-16, and USW SD-12, 1996.	WS
GS940608312261.003 N/A	Weeks, Does the wind blow through Yucca Mountain?, 1993.	N
GS930408312271.021 N/A	Yang et al., Analysis of gaseous-phase stable and radioactive isotopes in the unsaturated zone, Yucca Mountain, Nevada, 1985.	N
N/A N/A	Flint, L. E., Pneumatic properties derived from core analysis, 1996. (RBT1, RBT2, RBT3)	WS
GS920108312231.006 N/A	Flint, L. E. and A. L. Flint, Preliminary permeability and water-retention data for non-welded and bedded tuff samples, Yucca Mountain area, Nye County, Nevada, USGS OFR-90-569, 1990. (UZ#4, UZ#5, a#1, a#4, and a#6)	N
GS940408314211.020 NNA.19940629.0032	Geslin, J. K. and T. C. Moyer, Summary of lithologic logging of new and existing boreholes at Yucca Mountain, Nevada, March 1994 to June 1994, US Geologic Survey Open-File Report 94-451, 1994. (USW NRG-7a)	Y
GS940308314211.009 MOL.19940810.0011	Geslin, J. K., T. C. Moyer and D. C. Buesch, Summary of lithologic logging of new and existing boreholes at Yucca Mountain, Nevada, August 1993 to February 1994, US Geologic Survey Open-File Report 94-342, 1994. (USW NRG-6)	Y

Table 1.1.1
QA status and data tracking numbers (DTN) for data used in preparation of this report.

DTN & ACCN	Explanation	QA
GS921008312211.008 NNA.19911219.0001	Loskot, C. L. And D. P. Hammermeister, Geohydrologic data from test holes UE-25 UZ#4 and UE-25 UZ#5, Yucca Mountain area, Nye County, Nevada, US Geologic Survey Open-File Report 90-369, 1992.	N
N/A N/A	Lugo, C. L., Distribution of field borehole summary for UE-25 ONC#1, Letter: Lugo, C. L. (SAIC) to Gridley, W. A. (DOE), January 6, 1995.	N
GS940808314211.041 MOL.19950522.0208	Moyer, T. C. and G. Mongano, Graphical lithologic log of borehole USW SD-9 from base of Paintbrush Group, 1994.	Y
GS940808314211.052 MOL.19950505.0057	Moyer, T. C. and G. Mongano, Graphical lithologic log of borehole USW SD-9 from base of Paintbrush Group to total depth, 1994.	Y
GS950908314211.034 N/A	Zimmerman, C. L. And D. C. Buesch, Graphical lithologic log of borehole USW UZ-7a, 1995.	Y
N/A N/A	Rautman, R. A. and D. A. Engstrom, Geology for the USW SD-7 Drill Hole, Yucca Mountain, Nevada, Sandia National Laboratory Letter Report SLTR-96-000X, SNL Report SAND96-1474, 1996.	WS
N/A N/A	Rautman, R. A. and D. A. Engstrom, Geology for the USW SD-12 Drill Hole, Yucca Mountain, Nevada, Sandia National Laboratory Letter Report SLTR-96-000X, SNL Report SAND96-1368, 1996.	WS
N/A N/A	Pruess, K., A. Simmons, Y. S. Wu, and G. Moridis, TOUGH2 software qualification, LBL-38383, UC-814, 1996.	Y
N/A N/A	Wu, Y.S. , S. Finsterle, P. Frazer, and A. Simmons, Software qualification for ITOUGH2 and various equation-of-state (EOS) modules and auxiliary modules for TOUGH2 and ITOUGH2, Report Lawrence Berkeley National Laboratory, Berkeley, CA, August 1996 (draft).	Y
In the QA column, WS indicates that the data has been collected under a YMP approved QA program and will be Q when it is officially submitted to the project.		

2. Pneumatic Data

Several different types of data are available for analyzing gas flow at Yucca Mountain. Pneumatic pressure at the surface and within the mountain has been monitored at twelve boreholes (Rousseau et al., 1995, Rousseau and Patterson, 1996, Multimedia Environmental Technology Inc., 1995, Patterson, 1996). Pneumatic injection tests have been performed on four boreholes (LeCain, 1996a, 1996b). Radioactive isotope data related to travel times from the surface have been collected from five boreholes (Thorstenson et al., 1989; Yang et al., 1985; Yang et al., 1993). Unlined boreholes at Yucca Mountain have been observed to inhale and exhale gas. At two boreholes at Yucca Crest this gas flow has been measured and correlated with atmospheric conditions, and one borehole has been surveyed with an anemometer to give flow with depth (Weeks, 1987; Thorstenson et al., 1989; Weeks, 1991).

2.1 Pneumatic pressure monitoring

Pneumatic pressure has been monitored at boreholes NRG#4, NRG#5, UZ#4, UZ#5, NRG-6, NRG-7a, SD-9, UZ-1, SD-12, UZ-7a, SD-9, and ONC#1. For this report data were available for all boreholes except NRG#5 and UZ-1. Four different systems are being or have been used to isolate and monitor portions of the boreholes. The USGS is using a series of grout lifts to isolate in-situ instrument stations in boreholes UZ#4, UZ#5, NRG-6, NRG-7a, SD-12, and UZ-7a (Rousseau et al., 1995). The USGS is using a Seamist liner system in boreholes NRG#5 and SD-7. The USGS has monitored the pressures in the annular spaces outside two of the cased intervals in SD-9. Nye County is using a multi-probe packer system in boreholes NRG#4 and ONC#1 (Multimedia Environmental Technology Inc., 1995). Data from boreholes NRG-6 and NRG-7a are Q through April 12, 1995. Later data from NRG-6 and NRG-7a and data from UZ#4, UZ#5, SD-9, SD-12, UZ-7a, NRG#5, and SD-7 are expected to be Q. Data from UZ-1, NRG#4 and ONC#1 are non-Q. Tables 2.1.1 through 2.1.10 show depth and stratigraphic location of pressure monitoring. Table 1.1.1 shows references for lithologic data.

Uncertainty in the pneumatic monitoring data has only been reported for the USGS pressure transducer type used in boreholes UZ#4, UZ#5, NRG-6, NRG-7a, SD-12, and UZ-7a. Rousseau et al. (1995) state that, "the minimum acceptable calibration accuracy for these sensors is ±0.035 kPa (95 percent confidence level), over full scale." Uncertainties for other pneumatic monitoring data from boreholes NRG#4, SD-9, SD-7, and ONC#1 are assumed to be greater.

Table 2.1.1.
Location of instrument stations in borehole NRG#4

NRG#4		
Surface Elevation = 1249.5 m		
Instrument Station	Depth of Packer Interval	Stratigraphic Sub-Unit(s)
Probe 0	0 m	Surface
Probe 1	72.5 m – 86.0 m	Tpcpln
Probe 2	86.0 m –95.0 m	Tpcpln
Probe 3	95.0 m –140.0 m	Tpcpv2, Tpcpv1, Tpbt4, Tpy, Tpbt3, Tpp, Tpbt2
Probe 4	140.0 m – 155.0 m	Tpbt2; Tptrn
Probe 5	155.0 m – 165.5 m	Tptrn
Probe 6	165.5 m –197.0 m	Tptrn
Probe 7	197.0 m – 221.3 m	Tptrn - Tptpul

Table 2.1.2.
Location of instrument stations in borehole UZ#4.

UZ#4		
Surface Elevation = 1200.5 m		
Instrument Station	Depth	Stratigraphic Sub-Unit(s)
M	0 m	Surface
H	10.7 m	Qac
G	24.1 m	Tpcpv1
F	34.7 m	Tpy
E	44.5 m	Tpy
D	55.5 m	Tpp
C	87.8 m	Tpp
B	103.6 m	Tptrv3
A	111.6 m	Tptrn
Information on instrument station interval was not available for this report.		

Table 2.1.3.
Location of instrument stations in borehole UZ#5.

UZ#5		
Surface Elevation = 1204.5 m		
Instrument Station	Depth	Stratigraphic Sub-Unit(s)

Table 2.1.3.
Location of instrument stations in borehole UZ#5.

M	0 m	Surface
H	25.4 m	Tpcpln
G	34.0 m	Tpcpv1
F	39.7 m	Tpy
E	48.5 m	Tpy
D	60.3 m	Tpp
C	92.6 m	Tpp
B	104.5 m	Tptrv3
A	111.6 m	Tptrn
Information on instrument station interval was not available for this report.		

Table 2.1.4.
Location of instrument stations in borehole NRG-6

NRG-6		
Surface Elevation = 1247.5 m		
Instrument Station	Depth of Interval	Stratigraphic Sub-Unit(s)
M	0 m	Surface
G	36.0 m –42.4 m	Tpcpln, Tpcpv2
F	50.6 m – 57.6 m	Tpbt3, Tpp
E	78.3 m – 92.4 m	Tptrv1, Tptrn
D	101.5 m – 113.7 m	Tptrn
C	135.3 m –146.3 m	Tptrl, Tptpul
B	158.5 m – 168.6 m	Tptpul
A	213.7 m –226.8 m	Tptpul, Tptpmn

Table 2.1.5.
Location of instrument stations in borehole NRG-7a.

NRG-7a		
Surface Elevation = 1282.2 m		
Instrument Station	Depth of Interval	Stratigraphic Sub-Unit(s)
M	0 m	Surface
E	4.9 m –10.7 m	Tpcpln
D	34.4 m – 49.7 m	Tpy, Tpbt3
C	96.9 m –123.4 m	Tptrn
B	135.6 m –157.3 m	Tptrn, Tptrl
A	199.0 m –212.8 m	Tptpul

Table 2.1.6.
Location of instrument stations in borehole SD-9.

SD-9		
Surface Elevation = 1282.2 m		
Instrument Station	Depth of Interval	Stratigraphic Sub-Unit(s)
Zone 0	0 m	Surface
Zone 1	N/A	PTn, TSw
Zone 2	N/A	Below perched water
Information on instrument station depth or interval was not available for this report.		

Table 2.1.7.
Location of instrument stations in borehole SD-12.

SD-12		
Surface Elevation = 1323.7 m		
Instrument Station	Depth	Stratigraphic Sub-Unit(s)
M	0 m	Surface
P	24.4 m	Tpcpmn
O	43.9 m	Tpcplnh
N	65.5 m	Tpcplnc
M	76.8 m	Tpcpv2
L	92.0 m	Tptrv1

Table 2.1.7.
Location of instrument stations in borehole SD-12.

K	107.3 m	Tptm
J	128.6 m	Tptm
I	170.7 m	Tptpul
H	208.5 m	Tptpmn
G	236.5 m	Tptpmn
F	256.6 m	Tptpll
E	285.0 m	Tptpll
D	325.5 m	Tptpln
C	385.6 m	Tptpln
B	406.9 m	Tptpv2
A	435.9 m	Tac
Information on instrument station interval was not available for this report.		

Table 2.1.8.
Location of instrument stations in borehole UZ-7a.

UZ-7a		
Surface Elevation = 1289.3 m		
Instrument Station	Depth	Stratigraphic Sub-Unit(s)
M	0 m	Surface
J	14.9 m	Tpcpll
I	29.3 m	Tpcplnc
H	46.3 m	Tpcplnc
G	57.6 m	Tpcpv1

Table 2.1.8.
Location of instrument stations in borehole UZ-7a.

F	68.6 m	Tpbt2
E	76.5 m	Tptrn
D	112.2 m	Tptrn
C	151.2 m	Tptpmn
B	179.5 m	Tptpmn
A	195.4 m	Tptpll
Information on instrument station interval was not available for this report.		

Table 2.1.9.
Location of instrument stations in borehole SD-7

SD-7		
Surface Elevation = 1362.5 m		
Instrument Station	Depth	Stratigraphic Sub-Unit(s)
barometer	0 m	Surface
300	91.4 m	Tpcplnc
350	106.7 m	Tpp
400	121.9 m	Tptrn
500	152.4 m	Tptpul
550	167.6 m	Tptpul
600	182.9 m	Tptpul
650	198.1 m	Tptpul
700	213.4 m	Tptpmn
800	243.8 m	Tptpmn

Table 2.1.10. Location of instrument stations in borehole ONC#1.

ONC#1		
Surface Elevation = 1249.5 m		
Instrument Station	Depth of Packer Interval	Stratigraphic Sub-Unit(s)
Probe 0	0 m	Surface
Probe 1	140.5 m –158.5 m	Tpcpll, Tpcplnh, Tpcplnc
Probe 2	197.5 m –238.0 m	Tptrn

Table 2.1.10. Location of instrument stations in borehole ONC#1.

Probe 3	281.5 m –314.5 m	Tptpul, Tptpmn
Probe 4	314.5 m –356.5 m	Tptpmn, Tptpll, fault zone
Probe 5	356.5 m –367.0 m	fault zone, Tptpv, Tpbt1
Probe 6	367.0 m –376.0 m	Tpbt1, Tac
Probe 7	376.0 m –407.5 m	Tac

Prior to ESF interference, the pneumatic records at all boreholes show common characteristics. Sensors in the TCw record little to no amplitude attenuation and phase lag with respect to the surface barometric signal. Sensors in the PTn record increasing attenuation and lag with depth below the top of the PTn. Sensors in the TSw record the same amount of attenuation and lag over the entire thickness of the TSw at any one borehole. From borehole to borehole the attenuation and lag observed in the TSw appears to be governed by the thickness of the overlying PTn (see section 5.3). Only boreholes SD-9, SD-12 and ONC#1 are instrumented below the bottom of the TSw. In SD-9 and SD-12 the pneumatic response below the TSw appears to be governed by zones of perched water. Details of individual borehole records, including ESF interference, are discussed below.

All but two of the boreholes which are instrumented to record pneumatic pressures have recorded the effect of the barometric pressure signal transmitted from the ESF as the TBM neared and passed their location. NRG#4, UZ#4 & UZ#5, NRG-6, NRG-7a, SD-9, SD-12, and SD-7 have all recorded the presence of the ESF in the Topopah Spring unit. Rousseau and Patterson (1996b) show that NRG#5 has also recorded ESF interference. Boreholes which do not appear to have recorded ESF interference are UZ-7a and ONC#1. Borehole UZ-1 was taken off line before construction of the ESF was begun. Figure 2.1.1 shows borehole locations with respect to the ESF and major faults.

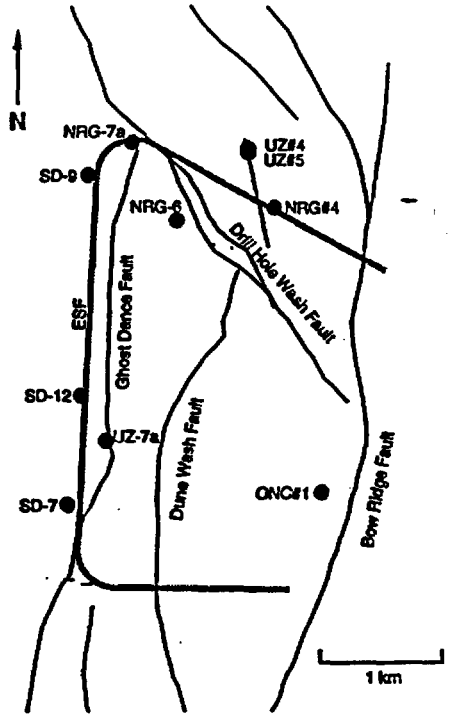

Figure 2.1.1. Plan view of ESF alignment, pneumatic monitoring boreholes and traces of major faults.

The face of the ESF (at the front of the TBM) passed closest to NRG#4 on June 16, 1995, and the TBM penetrated into the Topopah Spring unit on June 20, 1995. NRG#4 is approximately 16 m from the ESF. NRG#4 recorded the ESF barometric signal as the TBM was penetrating the partial gas barrier of the PTn and has continued to record the ESF barometric signal clearly. The signal is slightly attenuated when it reaches the sensor in NRG#4 at the same elevation as the ESF, and attenuation increases with sensor depth below the ESF elevation near NRG#4. The signal recorded in the TSw is in phase with the atmospheric signal and the diurnal component of the signal is very apparent.

The face of the ESF passed closest to UZ#4 & UZ#5 on September 2, 1995. UZ#4 and UZ#5 are approximately 350 m and 315 m respectively from the ESF. UZ#4 & UZ#5, which have been on line since June 29, 1995 and June 21, 1995, respectively, both show a daily component to their signals throughout their records though it is not apparent that this is due to the ESF barometric signal at all times. Lagging of the barometric signal is apparent until approximately August 27, 1995 when an increase in the daily signal amplitude in the Topopah Spring sensors is noted. At this point there is little or no phase lag between the barometric signal and the Topopah Spring signal, though there is attenuation of

the signal. Note that ESF interference began before the point of closest approach. A fault has been mapped at the surface and identified in the ESF that appears to connect to UZ#4 & UZ#5 (Rousseau and Patterson, 1996).

The face of the ESF passed closest to NRG-6 on September 15, 1995. NRG-6 is approximately 460 m from the ESF. Note that the Drill Hole Wash fault passes between the ESF and NRG-6 until approximately 300m after the closest point of approach. This fault may be responsible for blocking some or all of the signal from the ESF. After the ESF penetrates the Drill Hole Wash fault on September 29, 1995 there appears to be a slight change in amplitude attenuation of the TSw signal that is due to ESF interference via the Drill Hole Wash fault.

The face of the ESF passed closest to NRG-7a on October 25, 1995. NRG-7a is approximately 18 m from the ESF. NRG-7a shows little or no evidence of the ESF until approximately October 15, 1995 when the phase lag between the barometric signal and the Topopah Spring signal begins to decrease. At this point the ESF is approximately 140m along the tunnel alignment from its closest point to the borehole (the ESF is turning from the north ramp to the main drift). Note that the TBM crossed the Drill Hole Wash fault on September 29, 1995.Shortly thereafter the daily component of the barometric signal is observed in the Topopah Spring signal. By October 20, 1995 the barometric signal and the Topopah Spring signal are nearly in phase, and the ESF is 60m from its closest point to the borehole. The attenuation of the barometric signal is approximately 40% in the bottom most Topopah Spring instrument station (A), which is at the same elevation as the ESF, and increases to 60% in the upper most Topopah Spring instrument station (C, 85 m above A).

The face of the ESF passed closest to SD-9 on November 16, 1995. SD-9 is approximately 67m from the ESF. SD-9 shows evidence of the ESF barometric signal from November 5, 1995 onward. The ESF is approximately 140m along the tunnel alignment from its closest point to the borehole on November 5, 1995. Though the daily signal in the Topopah Springs sensor is masked in noise, other high frequency signals are more apparent during and after passage of the TBM. Lagging and attenuation of the Topopah Spring signal with respect to the barometric signal also decreases during and after passage of the TBM.

The TBM passed SD-12 on April 4, 1996. Borehole SD-12 is approximately 67 m from the ESF. As early as March 5, 1996 there is a diurnal component detected in the TSw response that was not there previously. This may be the first response to ESF interference in this borehole. On March 5, 1996 the TBM is approximately 300 m from SD-12 along the ESF alignment. If this is truely ESF interference, then it is the earliest that it has been detected in any borehole so far. Also of interest is the signal from the lower most Topopah Spring instrument station (C), 385.5 m below ground surface. Though the signal shows the same attenuation as the other TSw stations there is little or no phase lag with respect to the surface signal. This may indicate the presence of a fault pathway

from the surface with volumetric expansion accounting for the attenuation without any phase lag (see sections 3 and 6.4).

The TBM passed UZ-7a on May 2, 1996. The borehole is approximately 180 m from the ESF. No effect from the ESF has been observed in pneumatic pressure records from UZ-7a. UZ-7a is situated in the Ghost Dance fault zone at the surface. The effect of the fault as a preferential pneumatic pathway is observed in the data. Instrument stations down to D (112.2m below ground surface and in the TSw) record little phase lag compared to the atmospheric signal. The next instrument station in the TSw, C (151.2m below ground surface), shows a significant change in phase lag and attenuation compared to D. This indicates that between C and D the borehole leaves the Ghost Dance fault due to the dip angle of the fault.

The TBM passed SD-7 on June 5, 1995. SD-7 is approximately 100 m from the ESF at the closest point of approach. ESF interference in the borehole is not detected prior to May 25, 1996 when the TBM is approximately 125 m from the borehole along the ESF alignment. Borehole monitoring was off line from May 25 through May 31, 1996. On May 31 there appears to be ESF interference recorded in the borehole. This interference strengthens through June 5 as the TBM passes the borehole.

ONC#1 is not near the ESF. It is approximately 1 km north of the planned south portal of the ESF. No ESF interference has been observed in this borehole. The effect of a pneumatic pathway in the Bow Ridge fault zone is observed in the pneumatic response at station 5. The amplitude of the pneumatic response at this station is larger than the other stations in the TSw.

2.2. Air injection testing and analysis

The USGS has performed air injection tests on four boreholes at Yucca Mountain, NRG-6, NRG-7a, UZ-16, and SD-12 (LeCain and Walker, 1994, LeCain, 1996a, 1996b). Many three to five meter intervals in each borehole were tested using a four packer system. The packer system consists of a variable length injection interval with guard intervals above and below. Lengths of the injection interval for NRG-6 and NRG-7a are 4.3 m (14 ft) and 3.3 m (11 ft) (Rousseau et al., 1996). Portions of the TCw and TSw were tested in all four boreholes. In NRG-7a intervals in the PTn were also tested. There has been no testing of units below the TSw.

LeCains (1996a, 1996b) analysis of the injection test results is based on Hvorslevs (1951) analytical solution for elipsoidal flow during steady state injection testing (constant mass flow rate and constant injection interval pressure). Figures 2.2.1 through 2.2.4 (used with the authors permission, LeCain, 1996b) show permeability values from these analyses range from less than 30 milli-darcies to more than 40 darcies. Statistical analysis of permeability results from the TSw in NRG-6 and NRG-7a give geometric mean permeability of 820 milli-darcies and 290 milli-darcies, respectively (LeCain, 1996a). Standard devi-

ations are reported as 4.4 and 0.59 natural logarithm cycles for NRG-6 and NRG-7a, respectively. Inspection of Figure 2.2.1, which shows all the log permeability values for NRG-6, does not support the large reported standard deviation.

Advanced Resources International, Inc. (1994; 1995) also analyzed results from some of the USGS air injection tests using a combination of methods that analyzed both the transient and steady state portions of the injection test. For borehole SD-12, LeCain (1996b) reports permeability values ranging approximately from 100 milli-darcies to 40 darcies. ARI (1995) reports permeability values ranging from 90 milli-darcies to 67 darcies. The injection testing at SD-12 was performed only in the TCw and TSw. The average values from both analyses of SD-12 fall in the range from 1 to 10 darcies. ARIs (1995) analysis gives credence to the USGS analysis and results for SD-12 and the other boreholes.

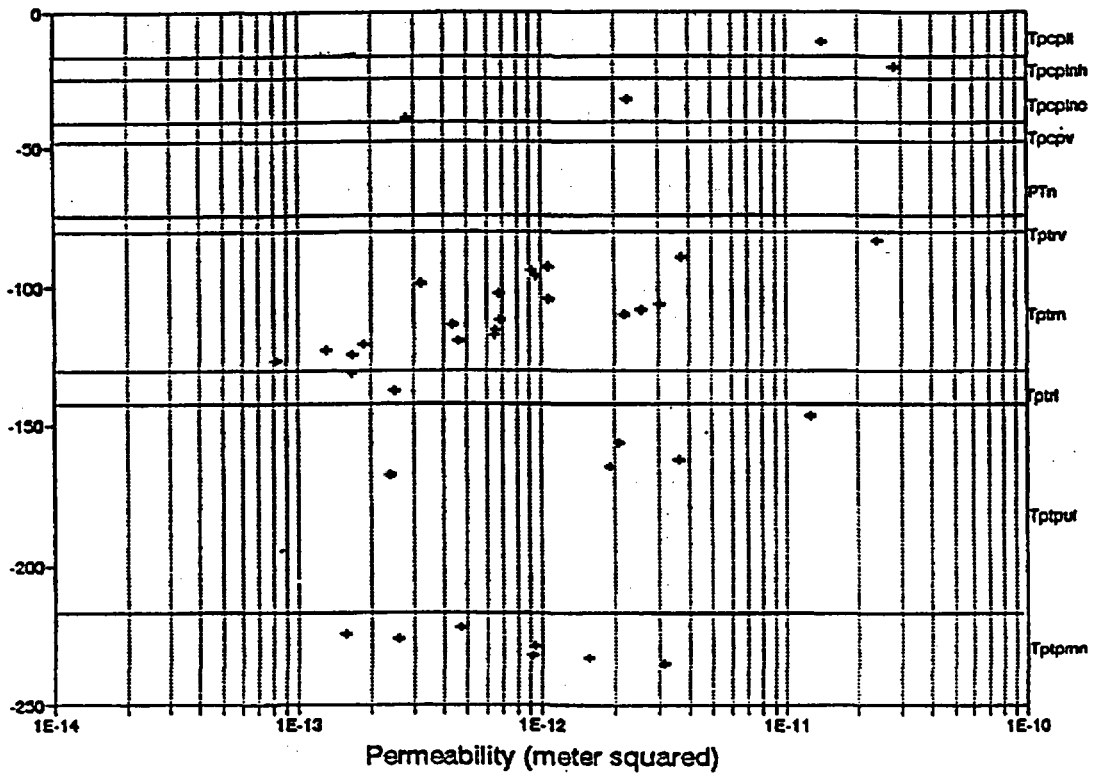

Figure 2.2.1. Results of air injection testing in borehole NRG-6 (LeCain, 1996b)

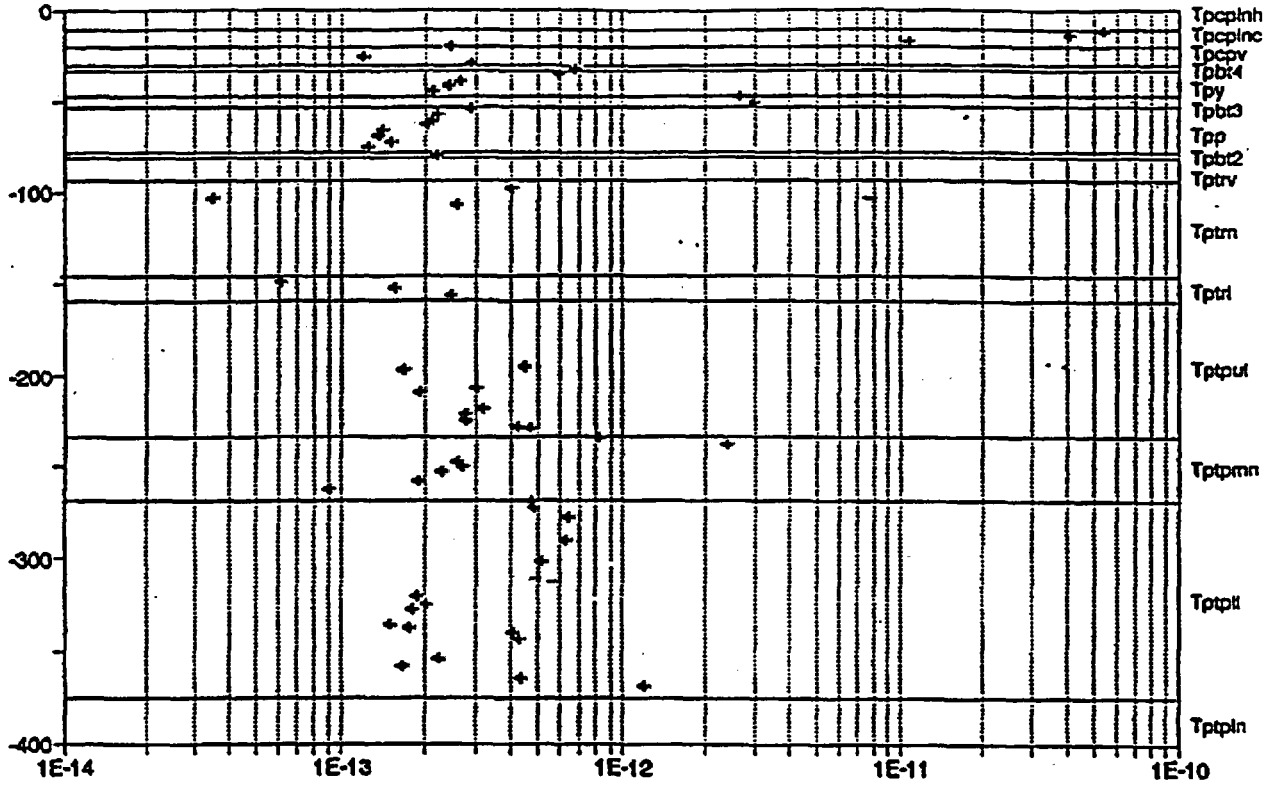

Figure 2.2.2. Results of air injection testing in borehole NRG-7a (LeCain, 1996b)

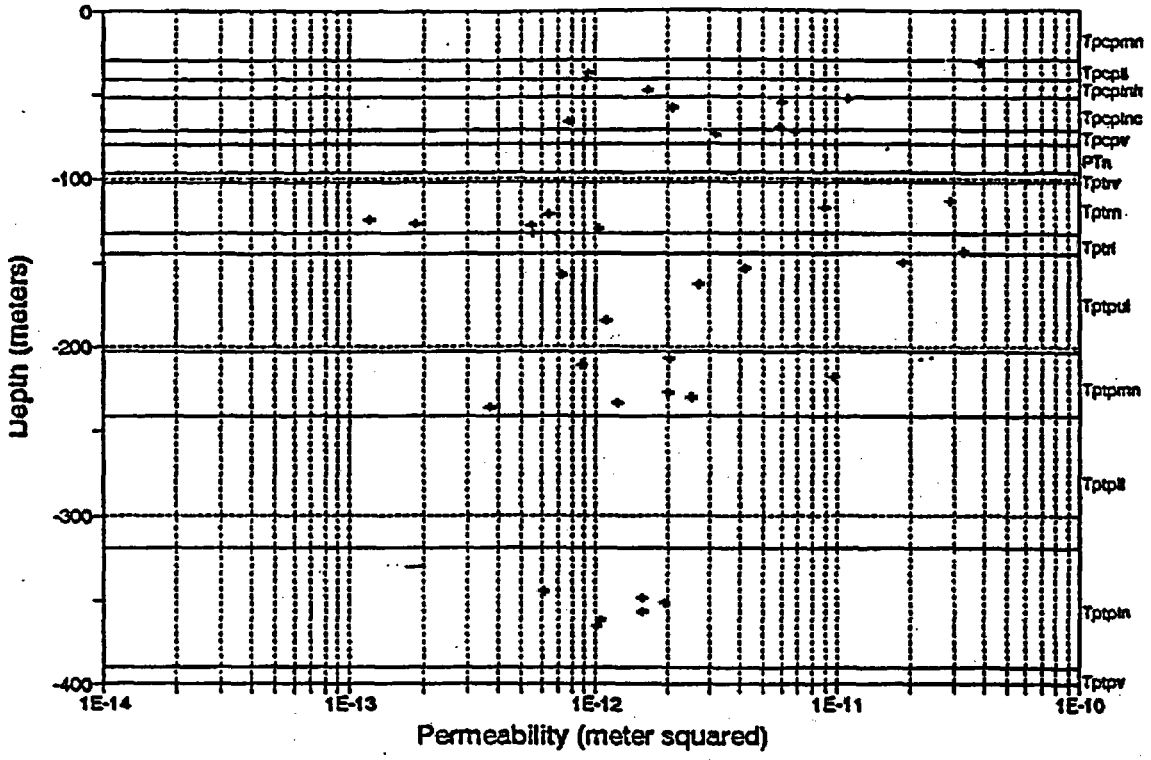

Figure 2.2.3. Results of air injection testing in borehole SD-12 (LeCain, 1996b)

Figure 2.2.4 shows permeability values with depth in UZ#16. No report of the steady-state analysis of UZ#16 air injection testing has been released at the time of writing this report. The figure shows permeability values in the same reange as reported ing the other boreholes.

Inspection of Figures 2.2.1 through 2.2.4 reveals no correlation of air permeability to sub-layer stratigraphy in the welded units (TCw and TSw). Stratigraphy is indicated on the right side of the figures.

At the time of writing this report the USGS air injection testing data are Q, and LeCains (1996a, 1996b) analyses are expected to be Q.

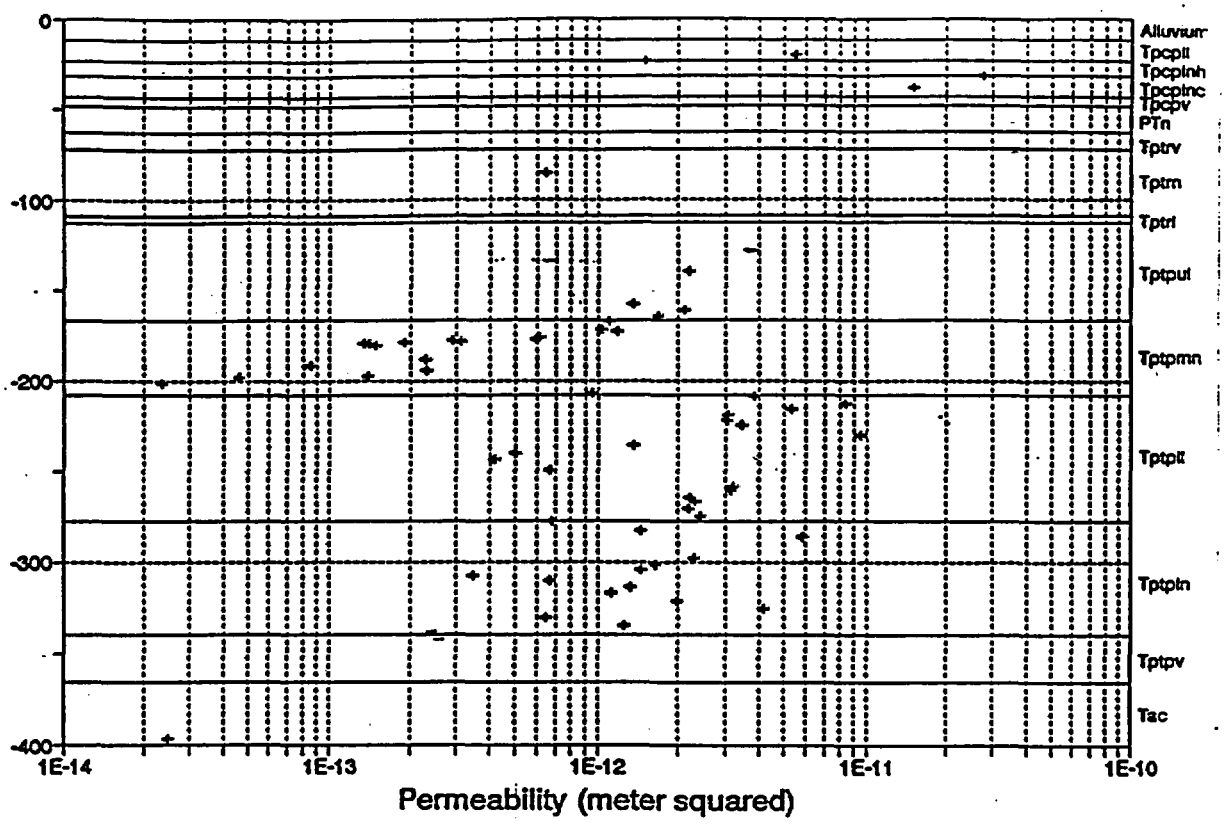

Figure 2.2.4. Results of air injection testing in borehole UZ-16 (LeCain, 1996b)

2.3. Radioactive Isotopes and Travel Time Analysis

Boreholes UZ-1, UZ-6, UZ-6s, UZ#4, and UZ#5 have been analyzed for apparent travel time with depth (Thorstenson et al., 1989; Yang et al., 1985; Yang, 1992; Yang et al., 1993). Water extracted from specific depths in the boreholes has been analyzed for C^{13} and C^{14} fractions of the solubilized CO_2 content. C^{13} fraction is interpreted to indicate the atmospheric or mineral (caliche and calcite) origins of the CO_2. Unfortunately, the C^{13} fraction does not indicate whether the CO_2 was transported in the gaseous or aqueous phase from the atmosphere. If the CO_2 is determined to be of atmospheric origin, the C^{14} fraction can be interpreted to give the travel times from the atmosphere.

Data from three boreholes have been interpreted to indicate that the sampled CO_2 is of atmospheric origin. Travel times in the Tiva Canyon welded unit (TCw) are interpreted to be relatively short, on the order of 100 years from the atmosphere. C^{14} fractions greater than 100% of the pre-1950s atmospheric fraction are found in the TCw, indicating some of the CO_2 can be dated after atmospheric nuclear weapons testing in the late 1950s and early 1960s. Travel times

in the Topopah Spring welded unit (TSw) are interpreted to be 1000 to 10,000 years (Thorstenson, 1989).

Tritium (H^3) is also a radioactive isotope that is used to estimate travel times. It also can be transported in the gaseous and aqueous phases.

Due to multiple transport mechanisms for the radioactive isotope data relevant to gas flow, the data can not be easily interpreted to give clear pneumatic travel times. Radioactive isotope data and interpreted travel times are non-Q.

2.4. Borehole gas flow

Boreholes USW UZ-6 and USW UZ-6s were drilled at Yucca Crest in 1984 and 1985 respectively. Borehole UZ-6 is cased through most of the Tiva Canyon welded unit (TCw) and, at its bottom, penetrates into the Prow Pass member (Whitfield et al., 1993). UZ-6s penetrates to the top of the Topopah Spring welded unit (TSw) and is uncased (Loskot, 1993). Observations were made of gas flowing in and out of both boreholes. At UZ-6, flow is observed both inside and outside of the casing. Gas flow out of the boreholes has been observed to be especially high during lower temperatures in the winter months, during periods of falling surface pressure, and when westerly winds strike the face of the Solitario Canyon escarpment (Weeks, 1987; Thorstenson et al., 1989; Weeks, 1991). Higher winter time gas velocities in both boreholes average 3 m/s (Weeks, 1987). Measurements were made of flow vs. depth in UZ-6s which showed that 80% of the flow originated in the top 30 meters of the borehole (Thorstenson et al., 1989).

Several forces are responsible, in varying amounts, for the observed flows. Variations in the surface pressure can cause the boreholes to inhale or exhale due to differences in head between the surface and formations tapped by the borehole. Wind striking the side of the mountain will force gas into the upwind face of the mountain due to the form drag of the mountain. Wind passing over the top of the mountain will create a zone of lowered pressure just downwind of the crest due to lift. Density variations due to temperature variations can be a cause of gas flow. Density variations due to gas composition (mainly water vapor content) can also cause gas flow, especially at steep exposed faces where a humid air column in the rock is in close proximity to a dry air column in the atmosphere (Weeks, 1991). Data on borehole air flow are non-Q.

2.5 Air permeability measurements on core samples

Air permeability measurments have been conducted on core samples from surface boreholes UZ#4, UZ#5, G-1, a#1, a#4, and a#6 and RBT1, RBT2, and RBT3 in ESF alcove 1. The data show that air permeability appears to be approximately an order of magnitude higher than water permeability measured on the same core samples. Ranges of permeability from 10 microdarcies to 400 millidarcies have been reported (Flint, 1996). Data from ESF core samples is Q. Data from surface borehole core samples is non-Q.

3. Conceptual Model

Gas flow within Yucca Mountain appears to be divided vertically into two cells, one in the TCw and one in the TSw. The TCw and TSw are welded and fractured, and it is assumed that most of the gas flow in these units occurs in the fractures. The intervening nonwelded PTn, composed of the nonwelded base of the TCw, the Yucca Mountain Tuff, the Pah Canyon Tuff, the nonwelded top of the TSw, and interbedded tuffs, acts as a partial barrier to gas flow between the welded units.

Transient gas flow is governed by the diffusivity of the formations through which the gas must pass. Gas diffusivity can be expressed as

$$\alpha_g = \frac{k\bar{P}}{n_a \mu} \tag{3.1}$$

where k is the intrinsic permeability times the relative gas permeability at the prevailing saturation, n_a is the drained porosity (total porosity times gas saturation), μ is the dynamic viscosity of the gas, and $\bar{P}$ is the average gas pressure. For an ideal gas the inverse of the gas pressure is equal to the compressibility of the gas. Equation 3.1 is similar to expressions given by Weeks (1978) and Shan (1995).

In using pneumatic pressure records to characterize the formations present at Yucca Mountain the parameter which is estimated is the pneumatic diffusivity. Pneumatic permeability or drained porosity may be determined from the pneumatic diffusivity if an a priori knowledge of the other exists. This a priori knowledge may come from laboratory tests on core samples to determine total porosity and liquid saturation and field testing such as neutron logging to determine in situ liquid saturation and air injection to determine permeability.

In dual porosity systems, such as the fractured tuffs at Yucca Mountain, the diffusivity of the fracture continuum and the diffusivity of the matrix continuum contribute to the overall diffusivity of the system. Injection and pump testing of double porosity systems show that at early times the response of the system is dominated by the fractures. At later times the contribution of the matrix to the response of the system can be observed.

In unsaturated media the absolute permeability is scaled by the relative permeability. Similar to the injection (pumping) example, the response of the pneumatic system at Yucca Mountain is a combination of the response of the fracture continuum and the response of the matrix continuum. High frequency signals are analogous to early times in the injection test where the response is dominated by the fractures. Low frequency signals are analogous to the late time response in the injection test where the response is a combination of the

fracture and matrix continua. Thus characterization of dual porosity systems is dependent on the frequency of the signal which is used to characterize them.

The pneumatic pressure response of an unsaturated system to a periodic signal, such as a barometric signal, is analogous to forced harmonic motion of an over-damped system. The over-damped system is characterized by having no significant contribution from momentum. Darcian flow can also be characterized as having no momentum component. Study of simple harmonic motion shows that there is a relation between the frequency of the forcing signal and the amount of amplitude attenuation and phase lag in the response. Amplitude attenuation and phase lag act more strongly on higher frequency signals.

To be clear, phase lag should be distinguished from time lag of a signal. Phase lag is measured in radians (or degrees) where 2π radians (360 degrees) are equal to one cycle of the source signal. The source signal for a natural pneumatic system is the barometric signal at the surface may be decomposed into different simple harmonic signals of amplitude and phase in their frequency space The time lag at a specific frequency is the phase lag divided by 2π radians divided by the frequency. This means that although lower frequencies have less phase lag than higher frequencies they will have more time lag.

The pathways for transient pneumatic flow at Yucca Mountain are determined by the characteristics of the different formations. The densely welded, highly fractured units, Topopah Spring and Tiva Canyon, are high pneumatic diffusivity units. Pneumatic flow in the densely welded units occurs entirely in the high permeability fracture continuum. Pneumatic storage in the densely welded units is small. The fractures occupy only a small fraction of the total volume of the rock mass; estimates are generally in the range of 0.1% (Witwer et al., 1995). The drained porosity of the matrix is estimated to be from one to three percent. Some of the drained matrix porosity may be occupied by immobile air bubbles reducing the effective drained porosity of the matrix. Between the high permeability of the fracture continuum and the small drained porosity of the combined fracture and matrix continuum, the densely welded units can be generally characterized as having high pneumatic diffusivity.

In contrast to the densely welded units, the moderately to non-welded units, collectively refereed to as the PTn and bounded by the densely welded units above and below, are characterized by very few through going fractures or fracture networks, more permeable matrix and higher drained matrix porosity. Fractures and fracture networks in the PTn are considered to be strata-bound such that fracture networks which are continuous through the PTn are rare (except in fault zones as discussed below). Within the individual strata of the PTn short fractures may contribute to the pneumatic permeability of the strata. The pneumatic permeability of the matrix in the PTn plays a more significant role in the pneumatic permeability of the strata especially in the non welded strata of the PTn where there are virtually no significant fractures. Drained

porosity of the PTn is estimated from 10% to 20%, and entrapped air reduces that fraction by only a small amount. The PTn can then be characterized as having a low pneumatic diffusivity.

Fault zones at Yucca Mountain provide high diffusivity pneumatic pathways deep into the mountain. Like the densely welded units they have high permeability fracture continua. The volume fraction occupied by the fracture continua in the fault zones is unknown but is assumed to be at least as much as in the densely welded units. Permeability of the fracture continuum probably is higher in the welded units and lower in the moderately to non-welded units. Storage (effective fracture plus drained matrix porosity) in fault zones is lower when the fault zone is in a densely welded unit and higher when it is in a moderately to non-welded unit due to the large drained porosity of the non-welded matrix. Within a fault zone transmission of the surface signal occurs with little attenuation or lagging. However, the influence of the fault zone on pneumatic responses in the rock mass near the fault zone quickly drops off with distance from the fault zone. The effect of volumetric expansion on the signal, as it propagates away from the fault zone, quickly overcomes the strength of the signal propagating downward through the narrow fault zone.

The ESF, as it penetrates the mountain, provides a second source for pneumatic signal. The distance over which there is influence from the ESF is, like the faults, dominated by volumetric expansion. The influence in front of the tunnel drops off as the cube of distance from the tunnel face as pressure fronts expand approximately spherically. At the sides of the tunnel, the influence drops off as the square of distance from the tunnel as the pressure fronts expand cylindrically. In the TSw, faults provide high diffusivity pneumatic pathways away from the ESF. Signals from the ESF can travel long distances with little attenuation through the fault zones.

This conceptual model is supported by several features of the gas flow data. Most of the density driven flow that occurs in the UZ boreholes occurs in the TCw. This is evident from the data regarding flow with depth from UZ-6s which shows that most of the flow occurs in the top 30 meters of the borehole. At the surface of the mountain in the repository area, the TCw is exposed or covered only by alluvium, and therefore is much more affected by atmospheric conditions. Flow conditions in the PTn and the TSw cannot be determined from the UZ-6 and UZ-6s flow data.

Isotopic data suggest that the gas in the TCw is much younger than the gas in the TSw. Isotopic data from boreholes UZ-1, UZ-6, and UZ-6s suggest that the gas in the TCw is on the order of 100 years old while the gas in the TSw is 1000 to 10000 years old. The one to two order of magnitude change in gas age across the PTn cannot be explained by linearly increasing travel time with depth. Rather, increased travel times around (via faults) or through the PTn compared to travel times in the TCw seems a plausible explanation. Travel

times in the TSw also appear to be long, but this may be due to smaller driving forces for the convection of gas. There is only a small area of TSw exposure in Solitario Canyon which would lead to atmospheric driven (density and wind) flow, so that most of the flow in the TSw is likely to be driven by the geothermal gradient with small perturbations from atmospheric pressure variations.

In the boreholes with pneumatic pressure monitoring, the data show a much stronger response to atmospheric pumping in the TCw than in the TSw. Data from the PTn show that most of the attenuation and lagging take place in this unit. The longest data records, at boreholes NRG-6 and NRG-7a, show that the response to atmospheric pumping in the TSw is stronger in borehole NRG-6. The PTn is about half as thick at borehole NRG-6 as it is at borehole NRG-7a.

ESF interference observed at boreholes NRG#4, NRG-7a, SD-9, SD-12, and SD-7 appears to be correlated to the distance between the boreholes and the ESF. ESF interference at boreholes UZ#4, UZ#5, and NRG-6 appears to be transmitted along fault zones.

4. Analytical simulation of time varying pneumatic pressures

Most of the simulation, prediction, and characterization of pneumatic response at Yucca Mountain in this report is performed with TOUGH2 and ITOUGH2 numerical simulation codes. The purpose of this section is to show the results of an analytical technique for calibration to and prediction of pneumatic response. These results provide insight into and help to benchmark the results of the numerical simulations. Parallel analytical and numerical simulations of UZ#5 are presented in this section.

4.1. Geologic Units and Air Pressure Data

Two boreholes, UZ#4 and UZ#5, were drilled about 38 m apart in the bottom of Pagany Wash (Rousseau and Patterson, 1996). In each borehole, eight sensors were installed at different depths (or elevations) and one additional sensor at the land surface. Using an equal scale for the horizontal and vertical directions, the different geologic units and the locations for all the sensors are shown in Figure 4.1.1. Note that the division of these units is usually based on the appearance of the rock samples. Therefore, such a division is probably a right choice for the physical properties of the rock matrix, but not necessarily a right one for the fractures. Since air mainly flows through fractures, the division in Figure 4.1.1 may only be taken as a reference in this study.

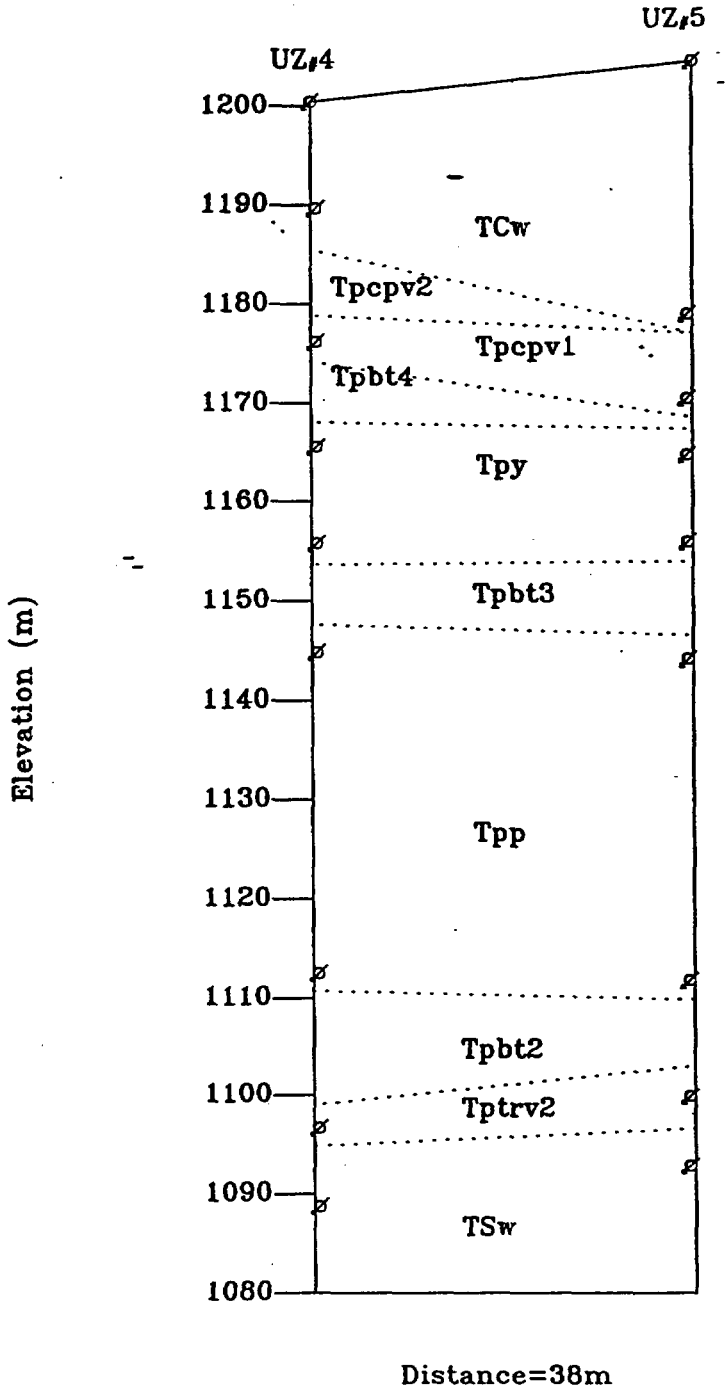

Figure 4.1.1 Geologic units and sensor locations at UZ#4 and UZ#5

To choose an appropriate model for the data analyses, we need to have some idea about how air flows underground. The observed air pressures from the two wells at t=33336 hours were used to create the isopressure map shown in Figure 4.1.2. A similar map was also obtained for the time instants of t=33456 hours (Figure 4.1.3) and t=33576 hours (Figure 4.1.4). t=33336 hours corresponds to 0:00h 7/21/96. From the three figures, we found that air flow in the study area is approximately one-dimensional in the vertical direction below the Paint-Brush non-welded (PTn) unit but aparently two-dimensional at some times in the Tiva Canyon welded (TCw) unit.

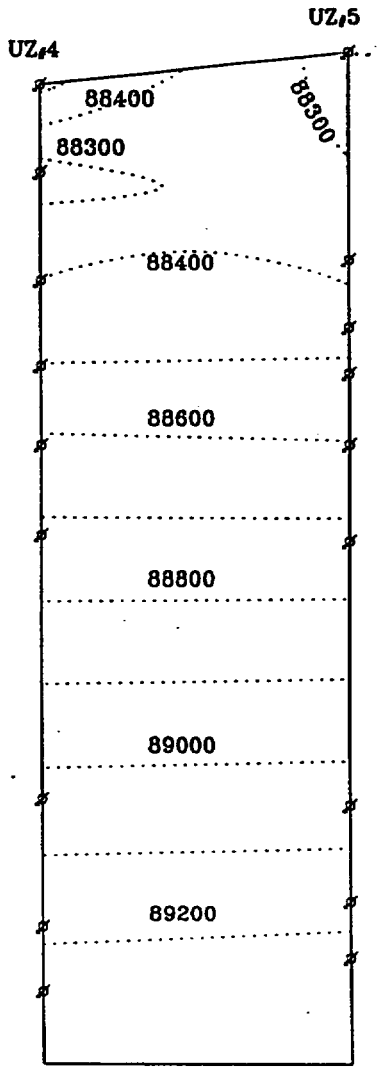

Figure 4.1.2 Air pressure (pascals) distribution at t=33336 hours. Air pressure data obtained from USGS (Rousseau, 1996)

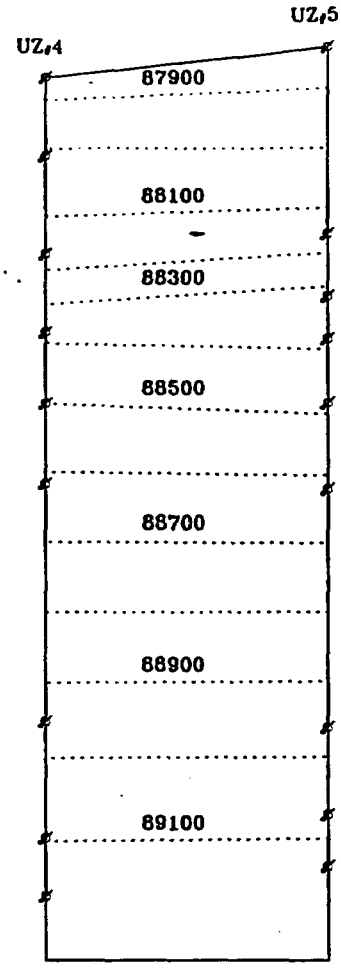

Figure 4.1.3 Air pressure (pascals) distribution at t=33456 hours. Air pressure data obtained from USGS (Rousseau, 1996)

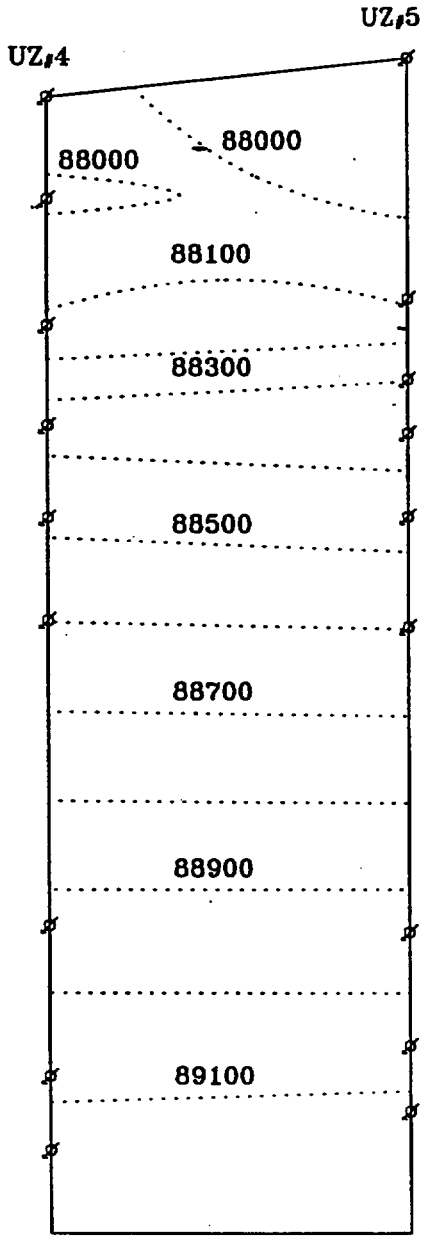

Figure 4.1.4 Air pressure (pascals) distribution at t=33576 hours. Air pressure data obtained from USGS (Rousseau, 1996)

4.2. The Analytical Solution

An analytical solution for air flow crossing a single layer soil was used to estimate the air permeability of the rocks. Such a solution was derived based on the following assumptions: (a) the flow is one-dimensional, (b) the soil (or rock) inside the domain is homogeneous, (c) the air pressure variation in the domain does not exceed 50% of the mean pressure, (d) the gravity, temperature and Klinkenberg effects are negligibly small. By means of these assumptions, the governing equation for such air flow was simplified to, (Shan, 1995),

$$\frac{\partial v}{\partial t} = \alpha \frac{\partial^2 v}{\partial z^2} \tag{4.2.1}$$

where z is the coordinate with the origin at one of the boundaries, t is time, and v is the dependent variable that equals the square of the air pressure P, i.e.,

$$v = P^2 \tag{4.2.2}$$

In (4.2.1), α can be called the diffusivity to air, which is defined by

$$\alpha = (kP_a)/(n_a\mu) \tag{4.2.3}$$

where k is the air permeability, P_a is the mean pressure, n_a is the air-filled porosity, and μ is the viscosity of air. For any specific problem, since the mean pressure can be calculated using the observation data, and the viscosity of air can be obtained from handbooks using the corresponding temperature, the parameters that affect the solution are the air permeability, k and the air-filled porosity, n_a. Furthermore, for any given initial and boundary conditions, it is the ratio of k and n_a that controls the response of air pressure inside the soil. For convenience, we used $n_a = 1.0$ in the following calculations. The actual air permeability, however, should be equal to the product of the measured air-filled porosity and the calculated air permeability in this study.

A merit of the analytical solution is that the initial and boundary conditions can be expressed in very general forms:

$$v(z, 0) = f(z) \tag{4.2.4a}$$

$$v(0, t) = \phi_1(t) \tag{4.2.4b}$$

$$v(L, t) = \phi_2(t) \tag{4.2.4c}$$

where L is the thickness of the soil layer, f, ϕ_1 and ϕ_2 can be any arbitrary functions or even in tabulated forms. The analytical solution of (4.2.1) which satisfies (4.2.4) is (Shan, 1995)

$$v = \frac{2}{L}\sum_{n=1}^{\infty} \exp(-a_n^2 \alpha t)\sin(a_n z)[I_u + a_n \alpha I_w] \tag{4.2.5a}$$

where

$$a_n = n\pi/L \tag{4.2.5b}$$

$$I_u = \sum_{i=1}^{j-1}\left[\frac{c_i}{a_n^2}[\sin(a_n z_{i+1})-\sin(a_n z_i)] + \frac{c_i z_i + d_i}{a_n}\cos(a_n z_i) - \frac{c_i z_{i+1} + d_i}{a_n}\cos(a_n z_{i+1})\right] \tag{4.2.5c}$$

$$I_w = \sum_{i=1}^{m-1}\frac{c_i^{(1)} - (-1)^n c_i^{(2)}}{a_n^4 \alpha^2}[\exp(a_n^2\alpha t_{i+1})(a_n^2\alpha t_{i+1} - 1) - \exp(a_n^2\alpha t_i)(a_n^2\alpha t_i - 1)] + \sum_{i=1}^{m-1}\frac{d_i^{(1)} - (-1)^n d_i^{(2)}}{a_n^2\alpha}[\exp(a_n^2\alpha t_{i+1}) - \exp(a_n^2\alpha t_i)] \tag{4.2.5}$$

where j is the number of data points for the initial condition and m is the number of boundary pressure data at the time of calculation. The coefficients, c_i and d_i are calculated by

$$c_i = (v_{i+1} - v_i)/(y_{i+1} - y_i) \tag{4.2.6a}$$

$$d_i = (y_{i+1} - y_i v_{i+1})/(y_{i+1} - y_i) \tag{4.2.6b}$$

In calculating (4.2.5c), y represents the coordinates of points where the initial pressures were measured; in calculating (4.2.5d), y represents the times where the two boundary pressures were measured. The solution is a simplified form for the special case where the pressures at different points are measured at the same time. Assuming the air pressure variations are measured at three points in the same geologic unit and along the flow direction, one can determine the air permeability of the unit using the analytical solution and the method of curve-fitting (Shan, 1995).

4.3. Calibration and prediction of pneumatic response at UZ#5 with an analytical model

The air pressures were observed at nine different elevations (including the surface) and different times from borehole UZ #5. The elevations of these observation sensors are shown in Table 4.3.1.

Table 4.3.1.
The elevations of the observation sensors

		Elevation	
Record Number	Sensors	(ft)	(m)
1101	A	3,585.42	-1,092.84
1107	B	3,608.42	1,099.85
1113	C	3,647.44	1111.74
1119	D	3,753.52	1,144.07
1125	E	3,792.26	1,155.88
1131	F	3,821.08	1,164.67
1137	G	3,839.92	1,170.41
1143	H	3,867.92	1,178.94
1153	M	3,951.40	1,204.39

In Table 4.3.1, Sensor M is located at the land surface, and Sensor A is the deepest one in this borehole. Three consecutive sensors were then grouped for the air permeability calculations. In each group, we set the origin at the lowest elevation of the three points and have the z axis point upwards. The coordinates for the middle point and the upper boundary are represented by z and L, respectively. Although we know that the air flow in the top unit (TCw) is not one-dimensional in the time period (from 33336 hours to 33576 hours) of calibration, we will keep these data points in the groups of calculations. The set of coordinates for the seven groups are shown in Table 4.3.2

Table 4.3.2.
z and L values for the seven calculation groups.

Group	ABC	BCD	CDE	DEF	EFG	FGH	GHM
z (m)	7.01	11.89	32.33	11.81	8.79	5.74	8.53
L (m)	18.90	44.22	44.14	20.60	14.53	14.27	33.98

These values and the initial and boundary conditions were used as input data to calculate the pressure variation at point for z an assumed air permeability k. A constant temperature of 25°C was used in all the calculations. The root-mean-square (RMS) was then calculated using the calculated and observed pressures at the middle point. By varying the air permeability in a range (e.g., from 10^{-22} to 10^{-2} m^2), we obtained the variation trend of the error, RMS. The air permeability corresponding to the minimum RMS is defined as the best-fitting k that is reported as the air permeability for the soil in the group. However, the existence of a minimum RMS in a reasonable k range is another assumption made during automated estimation of a best-fitting k, i.e., all the major assumptions are valid and the data are of good quality, which is not always true in reality. In the seven groups of calculations, there are two kinds of RMS behavior: an RMS curve with a minimum and an RMS curve with a lower limit at large value of k. In cases where a minimum exists, the minimum RMS and its corresponding air permeability can be determined by the computer program automatically. However, when the program

cannot find a minimum in the specified range, it stops at the upper limit (10^{-2} m^2) and gives this limit as the output for air permeability. In this case, inspection of the RMS curve is performed to estimate a minimum best-fit k. In fact, the air-permeability-dependent variation of RMS should be checked for both the automated and manual estimation cases. Figure 4.3.1 gives the RMS-k curves for all seven groups. Based on this figure, the best-fit air permeability for the six groups are given in Table 4.3.3. Groups GHM and ACD are estimated similarly.

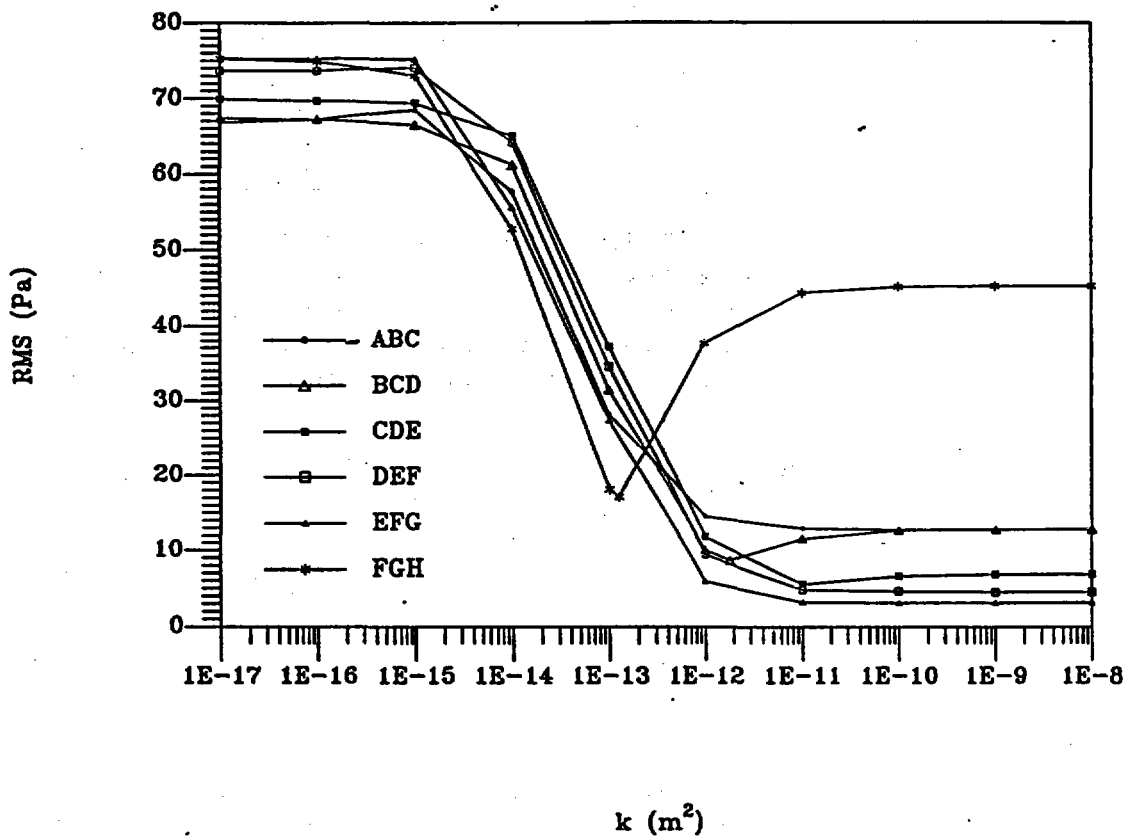

Figure 4.3.1. Fitting error (RMS) as a function of air permeability (k) for six sets of calculations.

Table 4.3.3.
The calculated air permeabilities

Group	ABC	BCD	CDE	DEF	EFG	FGH	GHM	ACD
k (m^2)	10^{-10}	1.832×10^{-12}	1.004×10^{-11}	10^{-9}	10^{-10}	1.253×10^{-13}	10^{-9}	3.750×10^{-12}

A comparison of the calculated and observed air pressures at the middle point of each group is shown in Figures 4.3.2 through 4.3.8. In each figure, the data of the first 10 days (33336 to 33576 hours) was used to calculate the air permeability that is reported in the figure. Such calculated air permeability and the observation data at the upper and lower boundaries for the next 18 days (33648 to 34080 hours) were then used to predict the pressure variation at the middle point. The two errors, E_{cal} and E_{pre} represent the RMS values for the calibration and prediction, respectively. The errors appear to be at the same level of measurement accuracy except that for Figure 4.3.8 corresponding to the group GHM, where the air flow is not one-dimensional.

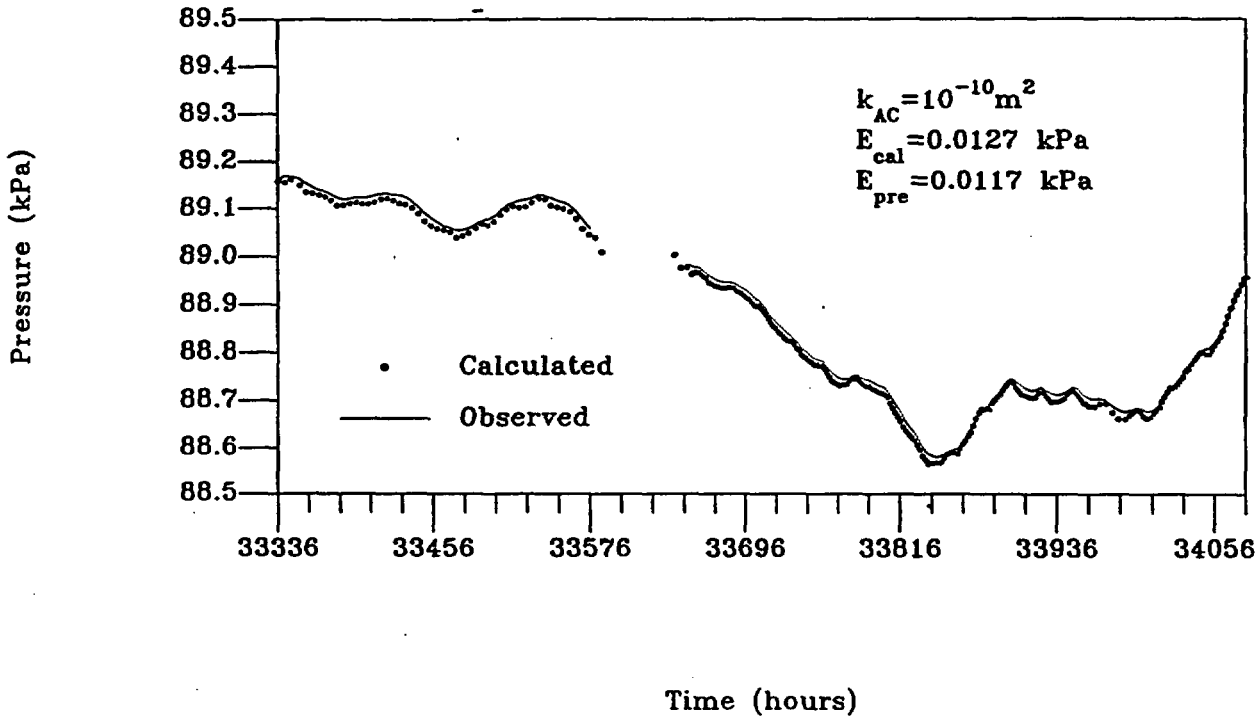

Figure 4.3.2. Comparison of the calculated and observed air pressures at sensor B in UZ#5. Observed data obtained from USGS (Rousseau, 1996).

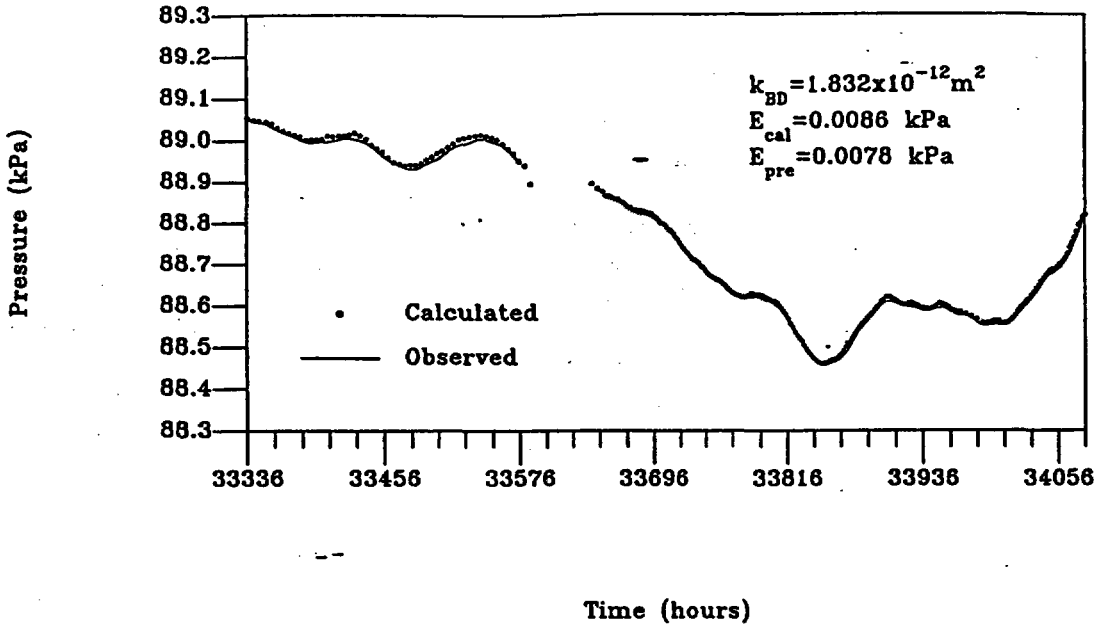

Figure 4.3.3. Comparison of the calculated and observed air pressures at sensor C in UZ#5. Observed data obtained from USGS (Rousseau, 1996).

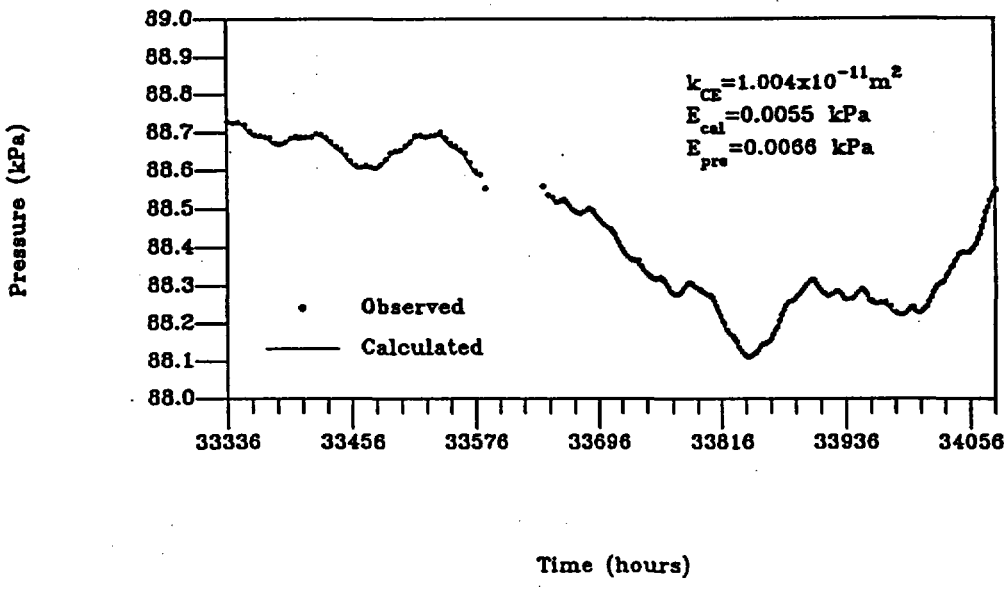

Figure 4.3.4. Comparison of the calculated and observed air pressures at sensor D in UZ#5. Observed data obtained from USGS (Rousseau, 1996).

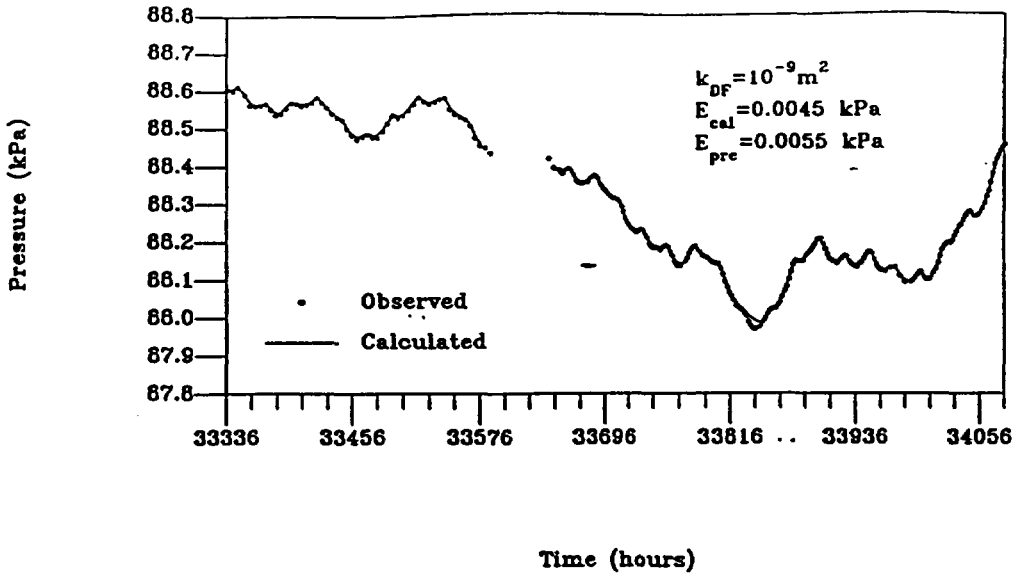

Figure 4.3.5. Comparison of the calculated and observed air pressures at sensor E in UZ#5. Observed data obtained from USGS (Rousseau, 1996).

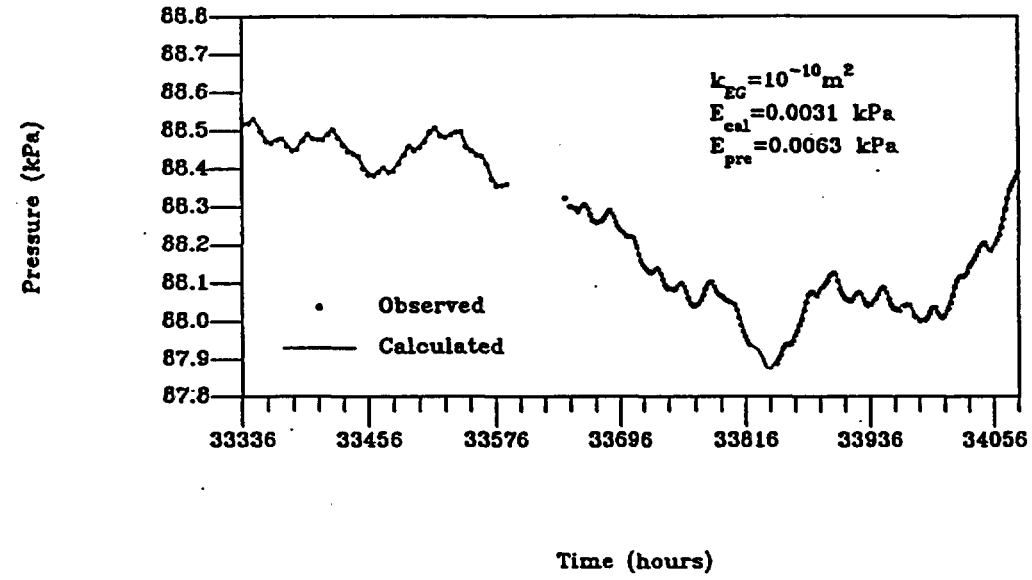

Figure 4.3.6. Comparison of the calculated and observed air pressures at sensor F in UZ#5. Observed data obtained from USGS (Rousseau, 1996).

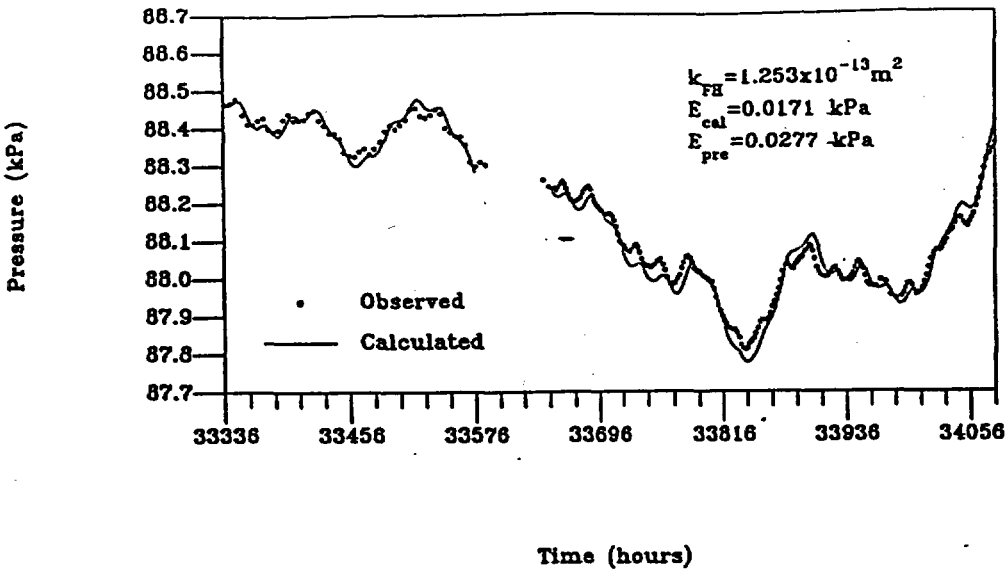

Figure 4.3.7. Comparison of the calculated and observed air pressures at sensor G in UZ#5. Observed data obtained from USGS (Rousseau, 1996).

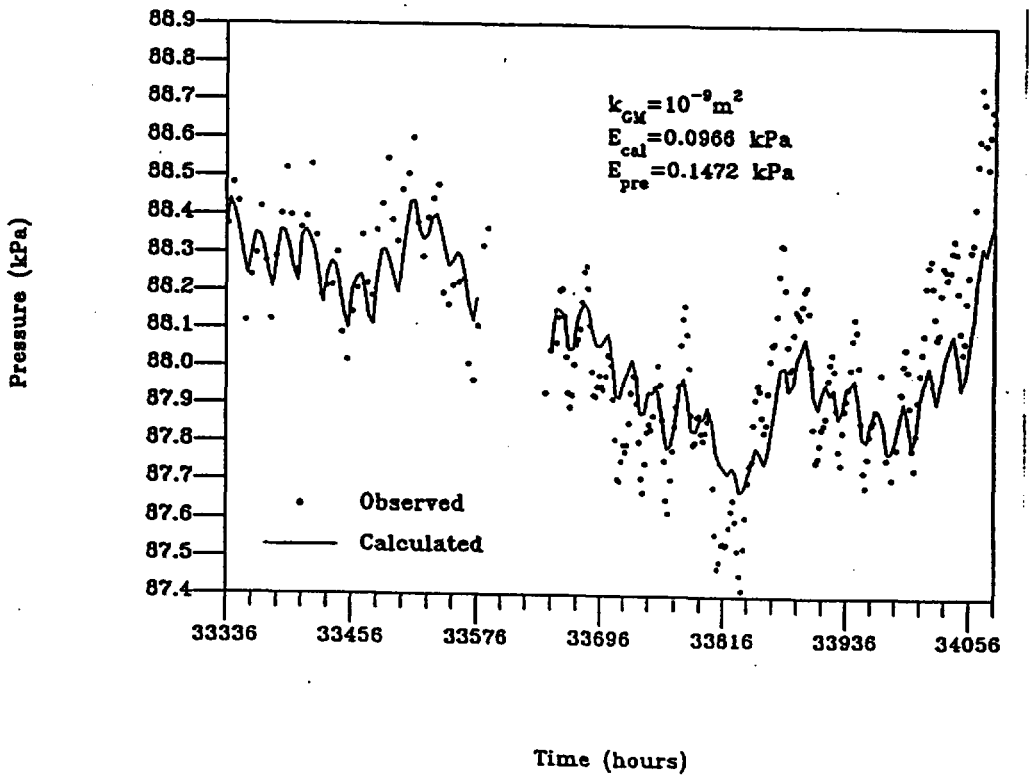

Figure 4.3.8. Comparison of the calculated and observed air pressures at sensor H in UZ#5. Observed data obtained from USGS (Rousseau, 1996).

The observation data from this site were obtained at different times for different observation points. To simplify the application, the data was first processed to obtain the pressure data at the same time for three different points using the method of linear interpolation. The processed data were then used for the calculation. But the raw data were used for comparison in the figures. Although there may be some additional error caused by the simplified calculations, the calculated pressure curves in Figures 4.3.2 through 4.3.7 seem to match the raw data very well. For one group, we conducted an additional calculation using raw data. The results are almost the same as those obtained using the processed data.

It is worthwhile to point out that the calculated air permeability for each group is actually an "equivalent air permeability" because each group may be composed of more than one geological unit. Such an equivalent air permeability is dependent on the location of the middle sensor. To determine the air permeability for these individual units, one may think of the application of the formula for calculating the equivalent hydraulic conductivity across a system with n layers (e.g., Freeze and Cherry, 1979):

$$k_E = \sum_{i=1}^{n} d_i \Big/ \sum_{i=1}^{n} \left(\frac{d_i}{k_i}\right) \qquad (4.3.1)$$

and the solution of the simultaneous equations. This is, however, only theoretically achievable. Practically, one may face problems. For example, using the results in Table 4.3.3, we obtained some negative air permeabilities for some units. This was caused by the uncertainty of most of the results. If we look back at Figure 4.3.1, we shall find that there is actually only one best-fit, which is from the group, FGH. For the other five groups, any value of k large than 10^{-12} m^2 yields an equally good match to the data. To show this, we used k =10^{-11} m^2 as the air permeability for rocks between points A and G, and the observed air pressures at A and G as the boundary conditions to calculate the air pressures at points B, C, D, E, and F. The calculations were conducted for both the 10-day calibration period and the 18-day prediction period. The calculated air pressures are compared with the corresponding observed ones in Figure 4.3.9. The RMS was calculated for the analytical solution at each station and gave a maximum of 11.7 Pa and a minimum of 3 Pa.

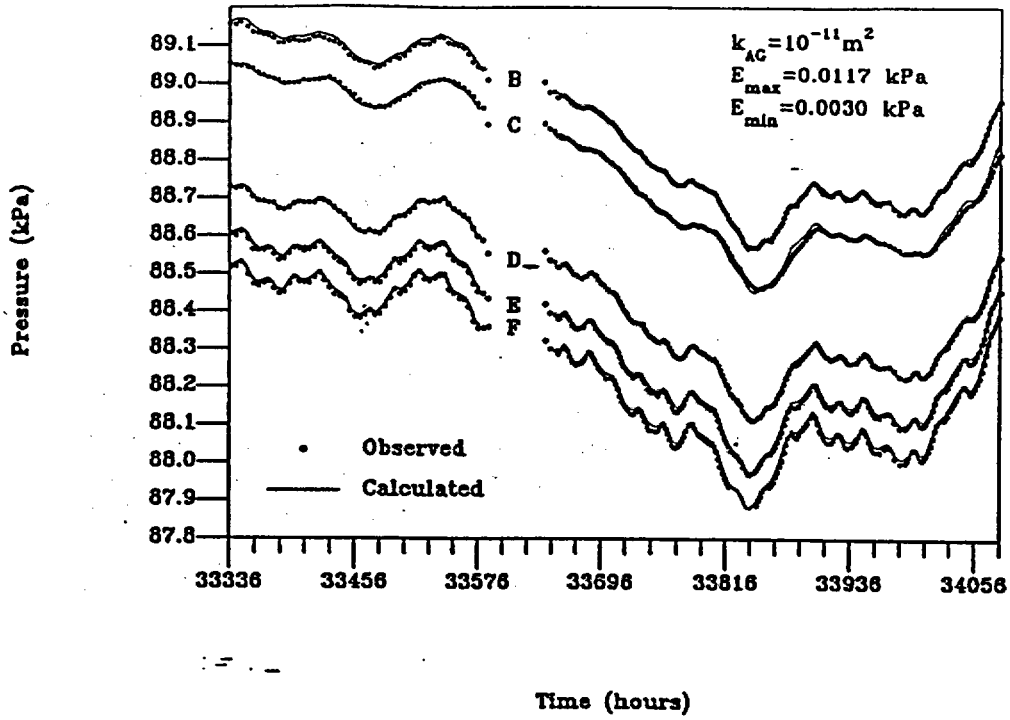

Figure 4.3.9. Comparison of calculated and observed air pressures at sensors B through F. A single value of air permeability, $k_{AG}=10^{-11}$ m^2, is used. Observed data obtained from USGS (Rousseau, 1996).

4.4. Parallel numerical simulations of UZ#5

The 10-days of data from UZ#5 were also used for a TOUGH2 (Pruess, 1991) simulation. A uniform grid size of 0.1 m was used to discretize the one-dimensional rock column between stations A and G. A maximum time step of 0.5 hours was used to control the time discretization. Module EOS3 was chosen to simulate the air flow using two-phase conditions and specifying single phase gas conditions (i.e. zero water content). The input data used a rock permeability of 10^{-12} m^2 and a rock porosity of 0.1 (the ratio of the two parameters is 10^{-11} m^2). To compare with the analytical solution, the gravity effect was neglected. The time-dependent pressure boundary conditions at A and G were generated by alternating injection and production of appropriate amounts of air as recommended by Moridis and Pruess (1992). A check on the output confirms that the air pressures at the two boundaries are exactly the same as the corresponding observed ones. The calculated air pressures at points B, C, D, E, and F are compared with the ones from the analytical solution for which a single permeability value was used. Figure 4.4.1 shows that the numerical and analytical solutions using a single permeability (the same in both cases) agree very well.

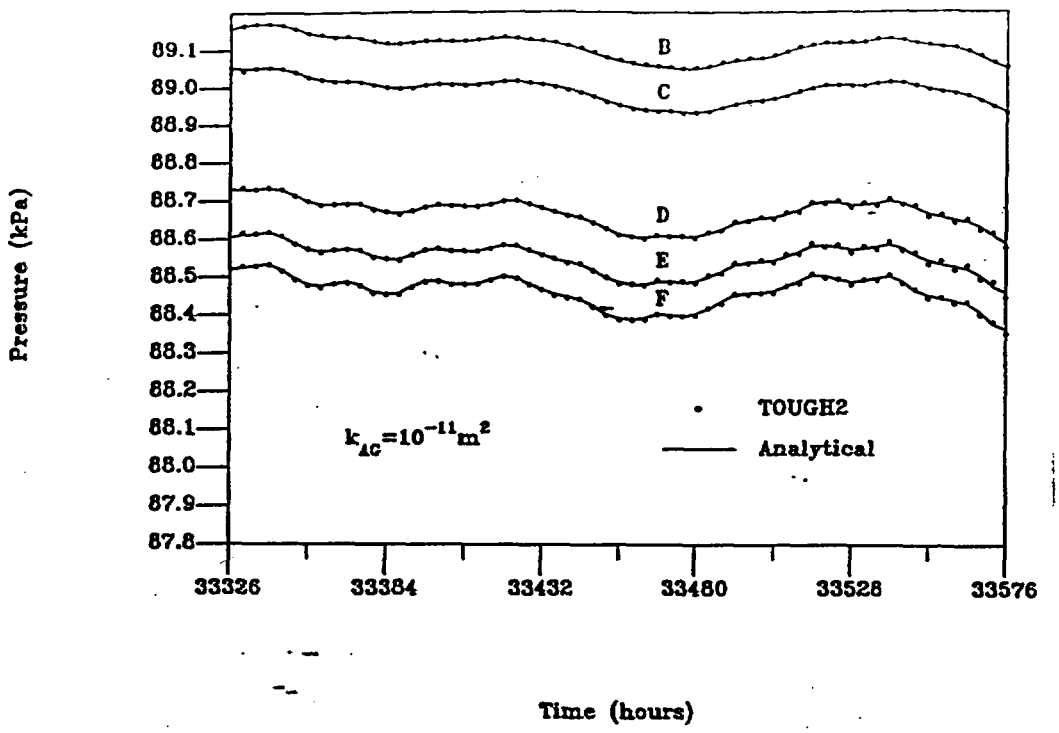

Figure 4.4.1. Comparison of calculated air pressures at five sensors using TOUGH2 and the analytical solution.

Two models of UZ#5 that represent the type of numerical grid used for simulations reported in section 5 were used to estimate pneumatic diffusivity for the intervals used with the analytical solution. The models are one-dimensional vertical grids that have no-flow boundaries at the lateral and lower boundaries. The lower boundary is situated at the regional water table. A time varying pneumatic pressure is applied at the upper boundary in order to simulate the pressure record at station H. Station H is used in these models because the non-one-dimensional flow above the top of the PTn appeared to interfere with reasonable comparisons between the numerical and analytical solutions.

Layering in the model is defined by instrument station position. In the first model the layers are positioned between stations B, D, F, and H. In the second model the layers are positioned between stations A, C, E, G and H. Pneumatic diffusivity for each interval is estimated by matching the simulated pneumatic pressures at all stations to the observed pressures over the same 10 day calibration period used with the analytical solution.

Table 4.4.1 shows the effective air permeability estimated with the numerical simulations compared to the effective air permeability estimated with the analytical solution. The match is worst at those groups for which the estimated effective air permeability is highest. This may be due, as pointed out above, to

the ability of the simulations to produce equally good matches at any value of effective air permeability above 10^{-12} m^2. The best matches are in those groups for which both estimates are below 10^{-10} m^2. Group GHM is not a good comparison because the column above station H is not present in the numerical simulation.

The comparisons in this section may be biased because no three stations are in the same stratigraphic layer. Unfortunately in other boreholes where stations are in the same stratigraphic layer, these stations are positioned in highly permeable layers which would also make estimation troublesome. One conclusion that can be made from this section is that the uncertainty associated with estimating pneumatic diffusivity numerically is no greater than doing so analytically.

Conclusions in this section are Q. The purpose of this section is not to characterize the tuffs at Yucca Mountain but to benchmark the performance TOUGH2 and ITOUGH2 with an independent means of similarly simulating and estimating pneumatic diffusivity. This benchmarking also allows a qualitative analysis of the uncertainties involved in simulating and estimating pneumatic diffusivity for the tuffs at Yucca Mountain. As such the data used in this section is important only in that it is generally characteristic of data collected at Yucca Mountain.

Table 4.4.1.
Effective air permeability estimated with analytical and numerical techniques.

	Estimated effective air permeability (m^2)		
Group	Analytical (Shan)	Numerical (TOUGH2)	Ratio of esimates
ABC	10^{-10}	4.1×10^{-8}	410
BCD	1.8×10^{-12}	1.3×10^{-11}	7.2
CDE	1.0×10^{-11}	1.1×10^{-11}	1.0
DEF	10^{-9}	5.6×10^{-8}	56
EFG	10^{-10}	4.1×10^{-11}	.41
FGH	1.2×10^{-13}	1.2×10^{-12}	9.3
GHM (GH)	10^{-9}	3.0×10^{-12}	0.0030

5. One-dimensional Numerical Simulation and Data Inversion

Calibration and prediction for most of this report are performed with the numerical simulation codes TOUGH2 (Pruess, 1991) and ITOUGH2 (Finsterle, 1993). Calibration and prediction are performed with one-dimensional (this section), two-dimensional and three-dimensional (following sections) models of Yucca Mountain. Stratigraphy taken from logs of the instrumented boreholes is used explicitly in the one and two-dimensional models. Where boreholes do not penetrate to the water table (the lower boundary of all models), the elevation of stratigraphic contacts is taken from the three-dimensional stratigraphic model (Bandurraga et al., 1996a)

One-dimensional numerical simulations were used to analyze the pneumatic pressure records from boreholes. Vertical pneumatic diffusivity of PTn sub-layers is estimated for boreholes NRG-6, NRG-7a, and UZ#5. The correlation between PTn vertical thickness and pneumatic response below the PTn is estimated using pneumatic records from boreholes NRG#4, UZ#4, UZ#5, NRG-6, NRG-7a, SD-9, SD-12, UZ-7a, and ONC#1. One-dimensional numerical analyses to determine pneumatic diffusivity at Yucca Mountain have also been reported by Kwicklis (1996) for boreholes NRG-6, NRG-7a, UZ#4, and UZ#5, in Multimedia Environmental Technology, Inc. (1995) for boreholes NRG#4 and ONC#1, and in Ahlers et al. (1995) for boreholes NRG-6 and NRG-7a.

One-dimensional simulation assumes that the direction of pressure diffusion is entirely vertical. As shown in the previous section, this assumption is only valid below the top of the PTn. However, it will be made for all layers. For all one-dimensional simulations reported in section 5, no-flow boundary conditions are applied to the lower and lateral boundaries. A time varying pressure boundary condition is applied to the upper boundary.

5.1. NRG-6 and NRG-7a joint inversion

As the first available data from the USGS was for boreholes NRG-6 and NRG-7a, these were the first boreholes to be simulated and analyzed. A common barometric signal is applied as the upper boundary condition for the two columns. Lateral and lower boundaries are no flow. The same diffusivity is used for each layer common to both boreholes. A joint inversion of the two boreholes is run in order to estimate a global diffusivity for each of the five layers modeled in the PTn. Permeability an porosity are actually the parameters modeled, and thus estimated. However, the single parameter, diffusivity, describes the transient behavior of the system. The PTn was previously identified, by sensitivity analysis, as the layer which controls the flow of gas deeper into the mountain (Ahlers et al., 1995). The estimated diffusivity for each PTn sub-layer is shown in Table 5.1.1 along with the estimated simulation parameters, permeability and porosity, used to calculate diffusivity. Also shown in Table 5.1.1 is the relative sensitivity of each of the sub-layers. It is the least permeable layers that are the

most sensitive and the layers that control the pneumatic response deeper in the mountain. Estimates of diffusivity and sensitivity presented in Table 5.1.1 are Q.

The best fit to the observed pressure data in the joint inversion is identified by ITOUGH2 (Finsterle, 1993) which minimizes the squared difference between the data and the simulated pressures at predetermined points in time. The robustness of this technique relies on the assumptions that the mean pressure of the simulation and data are exactly the same and, more importantly, that the time varying upper boundary condition is correct. The first assumption is difficult to implement exactly, but the error introduced by slight differences in the mean pressure is small. It is the second assumption that proves to be more troublesome. The only record of the time varying pressure boundary condition is taken from a point on the surface at the top of each pneumatic monitoring borehole. The pneumatic pressure variation at depth is a response to the barometric signal over some finite area at the surface. The effective upper boundary condition and the measured signal at the surface may not be the same due to actual variations in the surface signal and heterogeneity in the rock column (leading to preferential flow paths and non-one-dimensional, vertical flow). In practice construction of a time varying pressure record for the upper boundary condition is even more difficult. Due to gaps in the data, it is necessary to mix surface pressure records from different boreholes in order to get a continuous record. For this and all following simulations a single continuous record was produced from records from multiple boreholes and applied as the upper boundary condition.

Figures 5.1.1 and 5.1.2 show the match between the simulation and the data for selected sensors in NRG-6 and NRG-7a using the estimates from the joint inversion of the two boreholes. The overall match using the estimated parameters is good. However the match at each sensor appears to need some improvement.

Table 5.1.1.
Estimated pneumatic diffusivity and sensitivity for PTn sub-layers from a joint inversion of NRG-6 and NRG-7a. TOUGH2 parameters permeability and porosity are also shown.

PTn sub-layer	Estimated pneumatic permeability (darcy)	Estimated drained porosity	Derived pneumatic diffusivity (m^2/s)	Sensitivity of estimated diffusivity
Tpcpv1/Tpbt4	1.59E-01	0.168	4.71E-03	1044
Tpy	7.29E-01	0.179	2.02E-02	223
Tpbt3	5.01E-02	0.171	1.46E-03	1920
Tpp	4.54E+00	0.192	1.18E-01	161
Tpbt2/Tptrv3	2.80E-01	0.165	8.41E-03	599

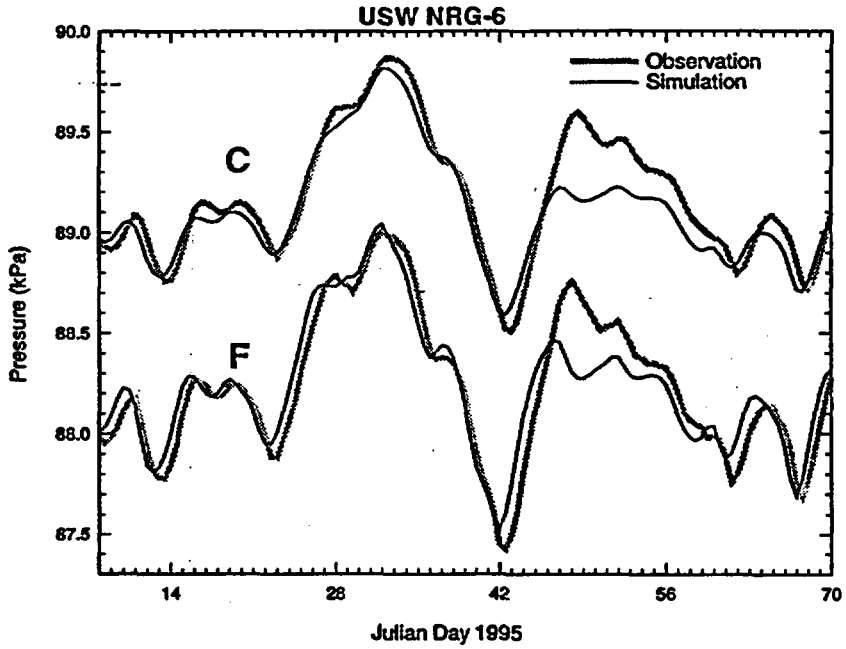

Figure 5.1.1. Simulated pneumatic pressure response at stations C and F in borehole NRG-6 using parameters estimated with a joint inversion of NRG-6 and NRG-7a. Observed data obtained from USGS (Rousseau, 1996).

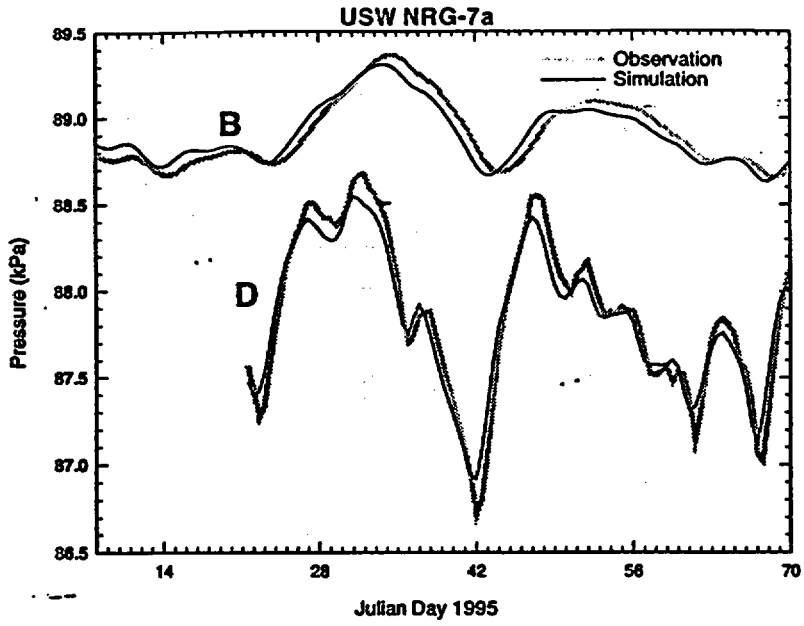

Figure 5.1.2. Simulated pneumatic pressure response at stations B and D in borehole NRG-7a using parameters estimated with a joint inversion of NRG-6 and NRG-7a. Observed data obtained from USGS (Rousseau, 1996).

5.2 Inversion of NRG-6, NRG-7a, and UZ#5 (individually)

In order to improve the match, the boreholes are simulated individually. UZ#5 is also added to the boreholes being simulated. Using the pneumatic diffusivity estimated by the joint inversion as the starting point, PTn diffusivity sets are estimated for each of the three boreholes individually. For these and all future simulations the simulation parameter, drained porosity, estimated by the joint inversion (see Table 5.1.1) is held constant and only the simulation parameter, permeability, is varied in order to vary the pneumatic diffusivity. From the equation for pneumatic diffusivity (3.1), we know that permeability and diffusivity are proportional if all other variables are held constant. Table 5.2.1 shows the diffusivity of the PTn sub-layers estimated for each of the boreholes. Permeability and porosity values that correspond to these values of diffusivity are shown in the section 6 in Tables 6.1.1, 6.2.1, and 6.3.1. The permeability values may be assumed to be correct as long as the drained porosity values are also assumed correct. These estimates are Q when data from these boreholes are submitted

Table 5.2.1.
Estimated pneumatic diffusivity from inversions of individual one-dimensional borehole simulations. NP means layer is not present at this borehole.

PTn sub-layer	Estimated pneumatic diffusivity (m^2/s)		
	NRG-6	NRG-7a	UZ#5
Tpcpv1/Tpbt4	4.7 e-3	3.9 e-3	7.4 e-3
Tpy	NP	1.7 e-2	1.1 e-1
Tpbt3	9.8 e-4	8.1 e-4	4.6 e-2
Tpp	7.9 e-2	6.6 e-2	6.5 e-2
Tpbt2/Tptrv3	5.7 e-3	4.8 e-3	1.5 e-2

Where possible the ratio between PTn sub-layer diffusivity values was held constant (e.g. the diffusivity of PTn sub-layers above instrument station F in NRG-6 were varied by the same factor during the inversion). In the case of UZ#5 each PTn sub-layer either has an instrument station in it or is bounded above and below by sub-layers that have instrument stations in them, so for this borehole each sub-layer is varied independently. Figures 5.2.1though 5.2.3 show the match for selected instrument stations in NRG-6, NRG-7a, and UZ#5.

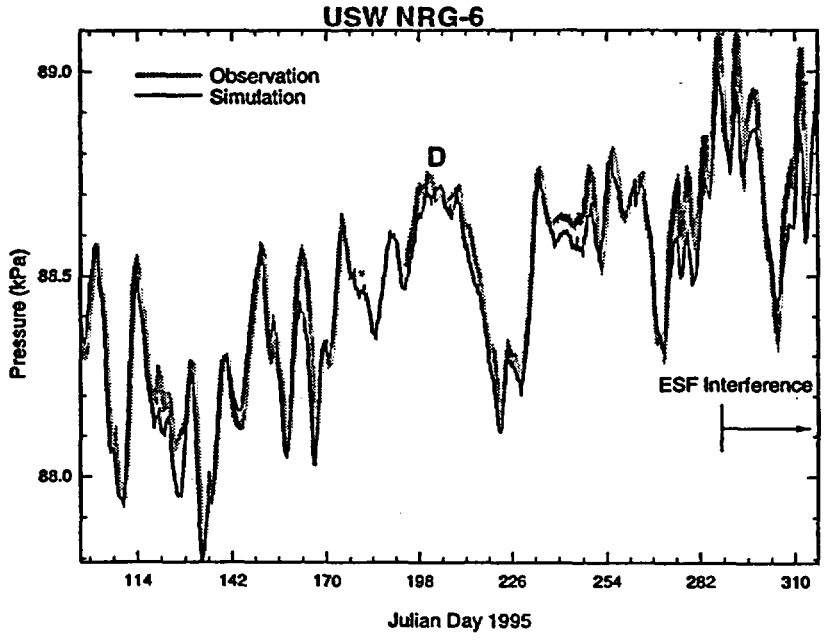

Figure 5.2.1. One-dimensional simulation match to observed data at station D in NRG-6. Observed data obtained from USGS (Rousseau, 1996). Note discrepancy between data and one-dimensional simulation after day 289 (October 16, 1995) indicating possi-

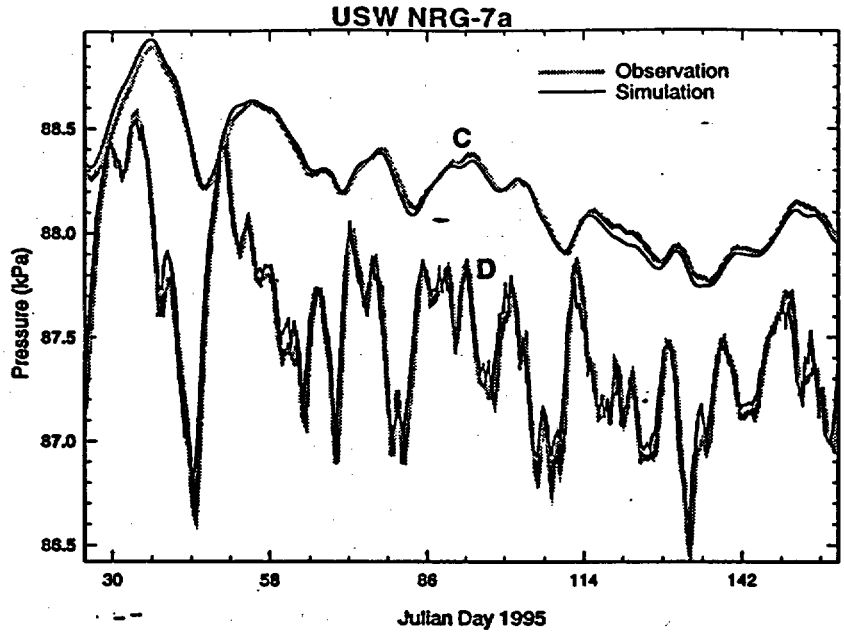

Figure 5.2.2. One-dimensional simulation match to observed data at stations C and D in NRG-7a. Observed data obtained from USGS (Rousseau, 1996).

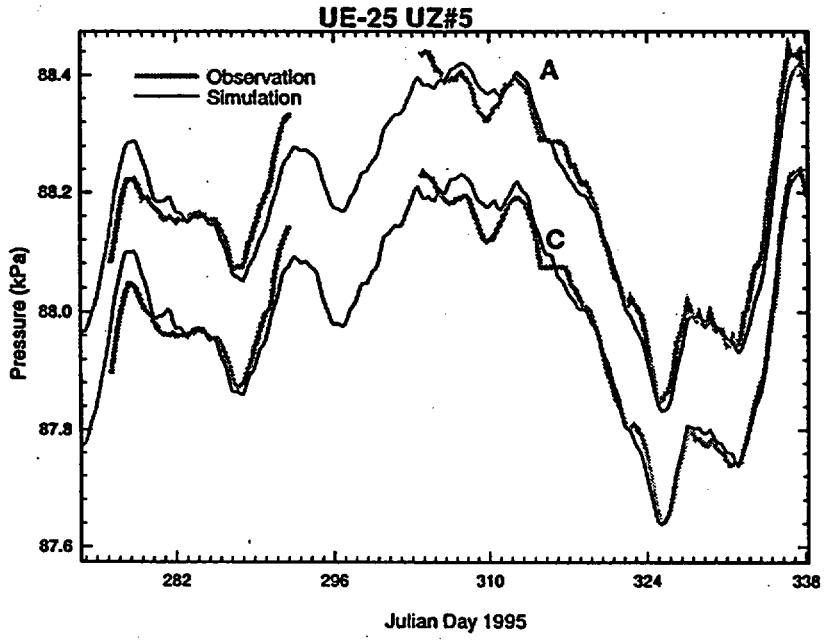

Figure 5.2.3. One-dimensional simulation match to observed data at stations A and C in UZ#5 Observed data obtained from USGS (Rousseau, 1996).

From the joint estimation of PTn diffusivity for NRG-6 and NRG-7a and the estimation for NRG-6, NRG-7a and UZ#5 individually, a common pattern is observed. Of the five layers into which the PTn is subdivided, the second and fourth, Tpy and Tpp, have consistently the highest diffusivity. These two layers have been identified as being moderately welded to non-welded and fractured in the vicinity of the three boreholes simulated (Moyer et al., 1995). The other three layers, Tpcpv1/Tpbt4, Tpbt3, and Tpbt2/Tptrv3 are non-welded with little or no fracturing. The higher pneumatic diffusivity of the Tpy and Tpp can be conclude to be due to the presence of fracturing in these layers, because the pneumatic permeability of the layer is a combination of fracture and matrix permeability. In the unfractured layers only matrix permeability is available for pneumatic diffusivity. Note that in the lower two non-welded layers (Tpbt3 and Tpbt4/Tptrv3) in UZ#5, the diffusivity contrast with layer Tpp is not as strong as in NRG-6 and NRG-7a. Even layer Tpcpv1/Tpbt4 shows a stronger diffusivity in UZ#5 than in NRG-6 or NRG-7a. The stronger diffusivity of the non-welded layers in UZ#5 is indicative of the imbricate fault that is very near this borehole. The fault provides fracturing even through the non-welded layers, locally increasing their pneumatic diffusivity.

5.3. Correlation of PTn thickness to pneumatic response below the PTn

The purpose of this investigation is to verify that there is a correlation between pneumatic response in the TSw and the thickness of the overlying PTn. Nine boreholes were simulated simultaneously for this investigation. The boreholes are (in the order that they occur along the ESF) NRG#4, UZ#5, UZ#4, NRG-6, NRG-7a, SD-9, SD-12, UZ-7a, and ONC#1. Boreholes NRG#4, NRG-6, NRG-7, and SD-9 do not appear to have any pneumatic fast pathways through the PTn or additional attenuating effects other than the PTn. UZ#5, UZ#4, SD-12, and UZ-7a are all associated with faults, by design in the case of UZ-7a. The faults act as fast pneumatic pathways through the PTn. ONC#1 has Rainier Mesa Tuff at the top of the borehole. This tuff is characterized much like the PTn tuffs in the borehole logs and is expected to act as a low diffusivity zone much like the PTn.

The first step in the estimation of an effective thickness of the PTn for all the boreholes is to establish a global value of effective diffusivity for the PTn at all the wells. This is done using an initial thickness of the PTn and pneumatic observations immediately below the PTn. The thickness of the PTn is initially set as the thickness from the top of Tpcpv2 to the bottom of Tptrv2. This interval includes the Yucca and Pah tuffs where they are present, the interbedded tuffs above, between, and below the Yucca and Pah tuffs, and the non to moderately welded base of the Tiva and top of the Topopah. These thicknesses are shown in Table 5.3.1. Table 5.3.1 also shows thicknesses that do not include the moderately welded base of the Tiva and top of the Topopah and the PTn thicknesses used for development of the new three-dimensional grid (Bandurraga et al., 1996a). Pneumatic observations from the first instrument station below the

PTn are used for all but borehole UZ-7a. In UZ-7a the first instrument station in the TSw that is not in the fault (instrument station C) is used. The estimated effective gas diffusivity for the PTn, determined by ITOUGH2, is 0.0066 m^2/s (200 milli-darcy gas permeability and 0.15 drained porosity).

The thickness of the PTn is then varied in each of the boreholes so that the pneumatic signal at each borehole matches as well as possible. The last column in Table 1 shows the estimated thickness of the PTn. Figures 5.3.1 through 5.3.3 show a comparison between the estimated PTn thickness and the thickness based on the logs and different definitions of the PTn.

Table 5.3.1.
Thickness in meters of the PTn at pneumatically monitored boreholes based on several definitions of the PTn. Estimated thickness of PTn from simultaneous inversion of pneumatic data from nine boreholes is in last column.

	Tpcpv2-Tptrv2	Tpcpv1-Tptrv3	New 3-D Grid	Estimated Thickness
NRG#4	53.03	44.22	44.22	53
UZ#5	80.46	74.06	80.47	40
UZ#4	90.77	79.85	84.06	41
NRG-6	37.95	31.79	31.79	38
NRG-7a	69.03	65.04	65.04	79
SD-9	64.4	62.70	62.70	74
SD-12	26.06	19.76	19.88	18
UZ-7a	23.68	18.99	25***	15
ONC#1	10.33*	5.76**	N/A	25
* Tpbt4-Tptrv2, **Tpbt4-Tpbt2, ***from UZ-7				

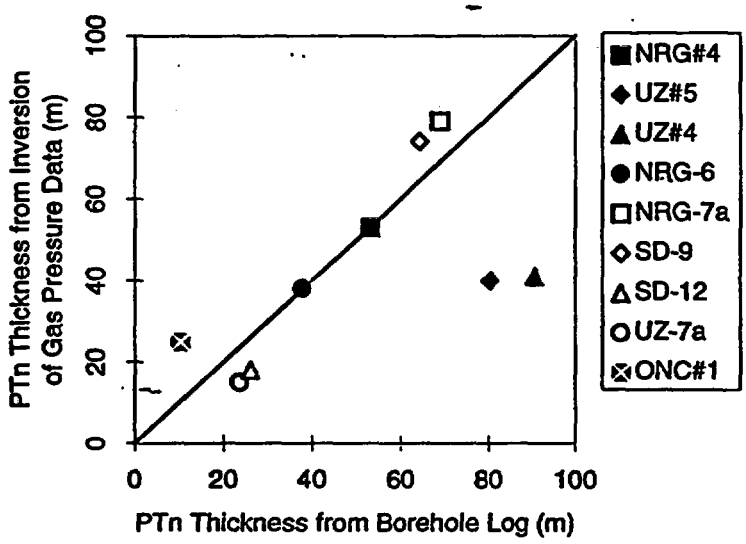

Figure 5.3.1. Tpcpv2-Tptrv2 PTn thickness vs. estimated PTn thickness.

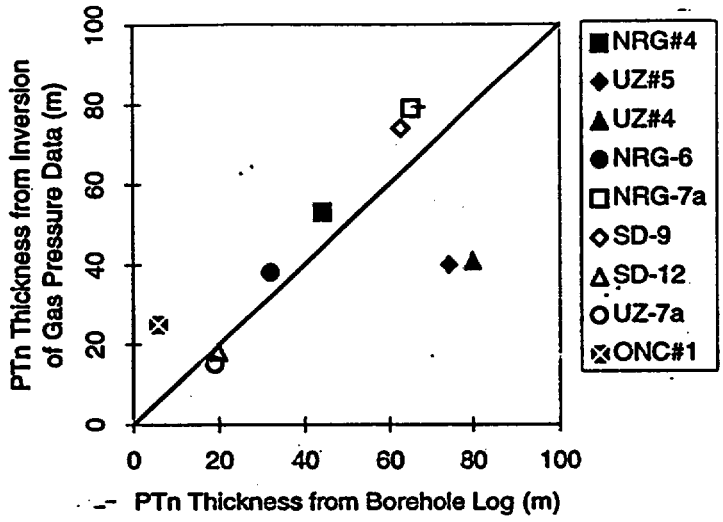

Figure 5.3.2. Tpcpv1-Tptrv3 PTn thickness vs. estimated PTn thickness.

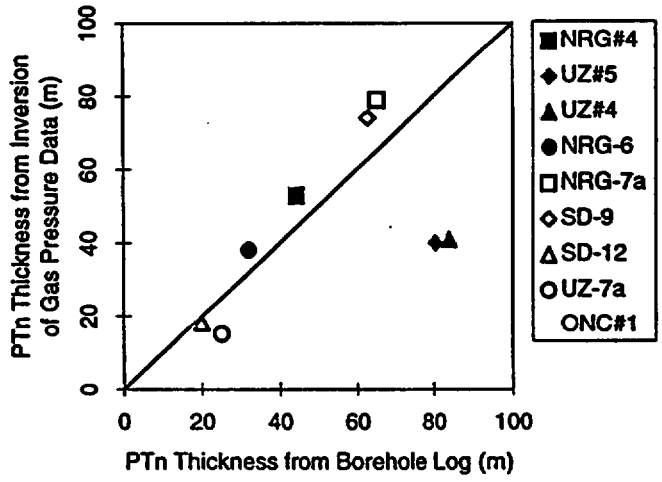

Figure 5.3.3. PTn thickness used for new 3-D grid vs. estimated PTn thickness. ONC#1 is not used for PTn thickness in the new 3-D grid.

In Figures 5.3.1 through 5.3.3, boreholes NRG#4, NRG-6, NRG-7a, SD-9, SD-12, and UZ-7a appear to fall consistently close to the 1:1 line that would indicate a perfect correlation between the PTn thickness and pneumatic response in the TSw. The data from these boreholes appear to define a line that is slightly skewed with respect to the 1:1 line. This may indicate that the Yucca and Pah tuffs are more important as pneumatic barriers than the interbedded

tuffs because they account for a larger portion of the PTn in the thicker areas than in the thinner areas. Where they are thin or not present the PTn is a less effective pneumatic barrier, and where they are very thick it is a much more effective barrier. It is also possible that the thicknesses at SD-12 and UZ-7a are underestimated because of the proximity of the Ghost Dance Fault which acts as a fast pneumatic pathway through the PTn. The estimated thicknesses from UZ#5, UZ#4, and ONC#1 do not correlate well with the actual thicknesses because there are other significant pneumatic pathways or barriers present, ie. the imbricate fault at UZ#4 and UZ#5, and the Rainier Mesa Tuff at ONC#1. Conclusions presented in this section are Q as they are based on data which will be Q when submitted. Non-Q data from NRG#4 and ONC#1 confirm conclusions based on Q data.

6. Two-dimensional numerical simulations

With the penetration of the ESF into the Topopah Spring unit, data are available to more completely characterize the pneumatic system in the Topopah Spring unit. By observing the response of gas pressures in boreholes close to, and far from, the ESF alignment, much can be learned about the pneumatic system. Boreholes close to the ESF give indications of the bulk pneumatic diffusivity and any anisotropy that may exist. While boreholes far from the ESF may give an indication of larger scale structures in the Topopah Spring unit, such as faults, that may affect the pneumatic system.

6.1. R-Z sensitivity analysis with ESF Signal

In order to study the effect of distance on the ESF signal and use this to characterize the diffusivity of the Topopah Spring unit, a basic grid is used. Figure 6.1.1 shows an approximation of the numerical grid used to investigate the distance effects of the ESF barometric signal. Nineteen layers are used in the r-z grid. Layers in the middle of the grid are 10 m thick with layers at the top and bottom increasing by 10 m increments to 50 m thick. In the radial direction, there are nineteen concentric rings from radius 10 m to 10,000 m. The (r between concentric rings increases logarithmically, giving six concentric rings per log cycle of radius, e.g., 10 m to 100 m, and a central cylinder of 10 m radius. All boundaries are no flow. A disc one third of the way from the top of the grid simulates the ESF source of the barometric signal. The disc is 10 m thick and has a radius of 68 m which gives it a surface area equivalent to approximately 1300 m of ESF tunnel.

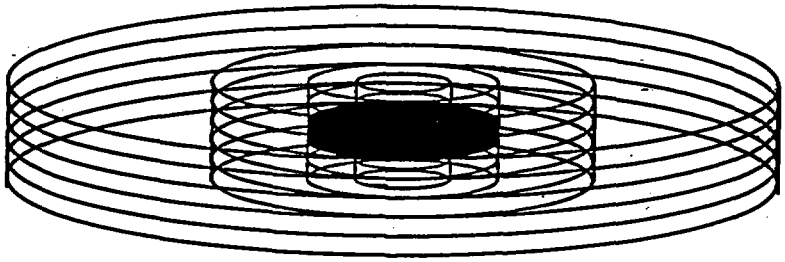

Figure 6.1.1. Schematic of r-z grid with logarithmically increasing (r. Shaded disc represents source for ESF barometric signal.

The simulation is run with only the air phase present. The effective air permeability and effective air porosity are the two input parameters of interest. Initial pressure conditions are static. There is a time varying pressure boundary condition at the source that is taken from records of the barometric signal at the surface of the mountain. Time stepping for the simulation is constant at one half day (43200 seconds) so that the daily component of the signal can be resolved in the simulation results.

Porosity and permeability are initially set to the default values from Wittwer et al. (1995), i.e. 0.001 and 10 darcy, respectively, for the Topopah Spring fracture system. This is equivalent to a gas diffusivity of 48 m^2/s. To study the sensitivity of the system to variations in diffusivity, the diffusivity is decreased over three orders of magnitude, and the response of the system is observed at various distances from the lateral boundary of the source. Figures 6.1.2 through 6.1.5 show the response of the system at the elevation of the source and at various distances from the lateral boundary of the source for four different values of diffusivity. In Figure 6.1.2, the pressure signal 16 meters from the lateral boundary of the source, is very strong. Also, note the strong daily component of the signal. Even 8338 meters from the lateral boundary of the source, the signal still responds to the larger peaks and toughs of the source signal. As the diffusivity is reduced the response at large distances from the source is also reduced. In Figure 6.1.5 there is no response at the most distant points and only a response to the overall trend of the source signal 505 meters from the source. At the innermost point, the response is approximately half of the response seen in Figure 6.1.2. There is a 3.3 order of magnitude difference in the diffusivity between Figures 6.1.2 and 6.1.5.

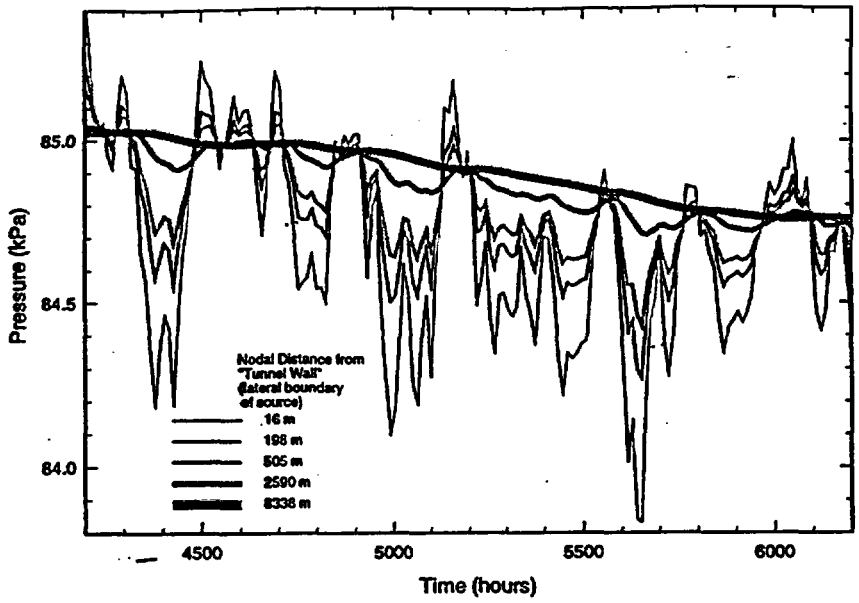

Figure 6.1.2. Response to ESF barometric signal at 16m, 198m, 505m, 2590m, 8338m from tunnel wall for 0.001 porosity and 10 darcy permeability (48 m^2/s gas diffusivity). Data used to simulate source signal obtained from USGS (Rousseau, 1996)

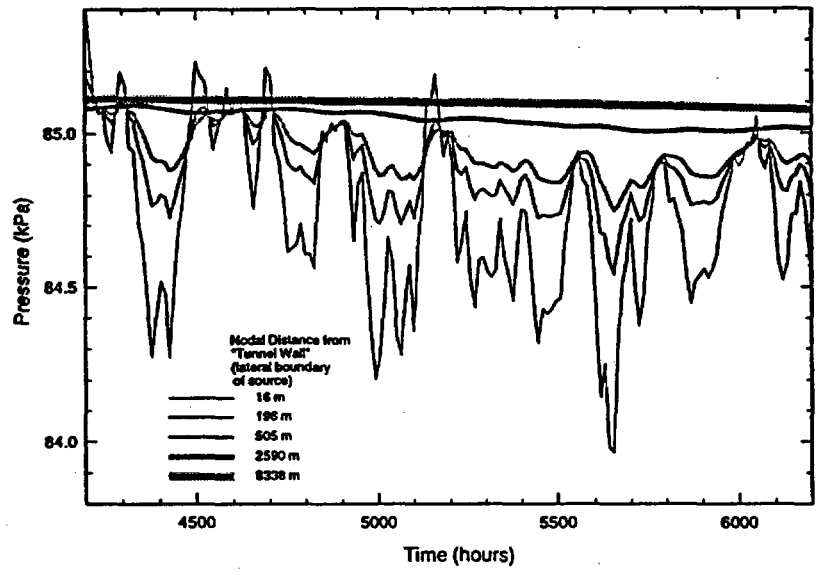

Figure 6.1.3. Response to ESF barometric signal at 16m, 198m, 505m, 2590m, 8338m from tunnel wall for 0.01 porosity and 10 darcy permeability(4.8 m^2/s gas diffusivity). Data used to simulate source signal obtained from USGS (Rousseau, 1996)

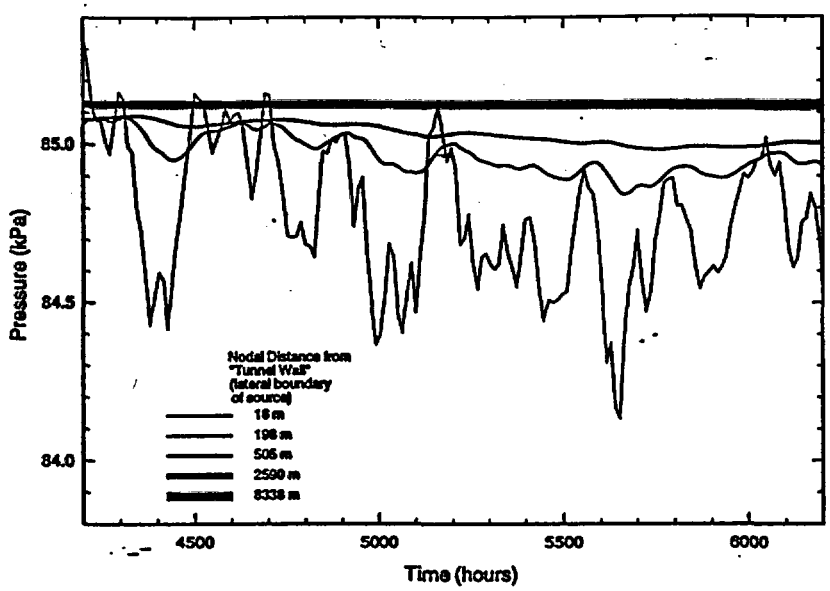

Figure 6.1.4. Response to ESF barometric signal at 16m, 198m, 505m, 2590m, 8338m from tunnel wall for 0.02 porosity and 1.0 darcy permeability (0.24 m^2/s gas diffusivity). Data used to simulate source signal obtained from USGS (Rousseau, 1996)

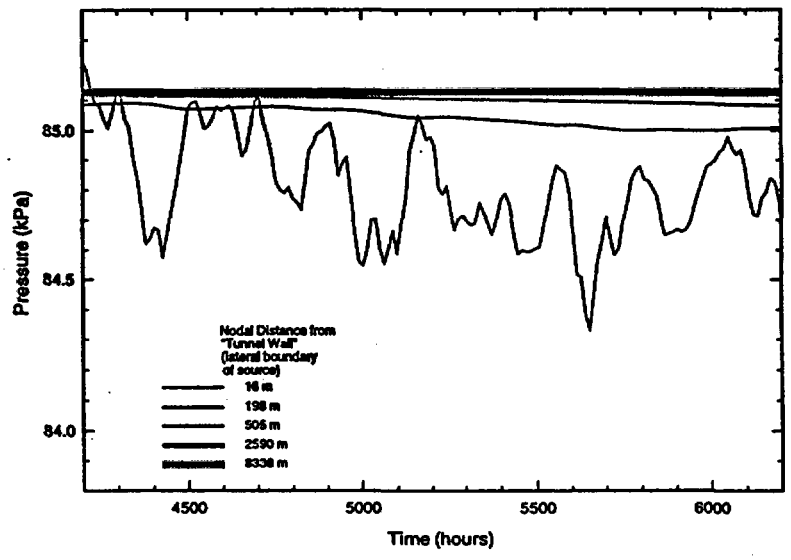

Figure 6.1.5. Response to ESF barometric signal at 16m, 198m, 505m, 2590m, 8338m from tunnel wall for 0.02 porosity and 0.1 darcy permeability (0.024 m^2/s gas diffusivity). Data used to simulate source signal obtained from USGS (Rousseau, 1996)

Figures 6.1.2 through 6.1.5 show that, though there is significant amplitude attenuation of the signal, the phase lag of the signal is only significant at low diffusivity and/or large distances from the source. At high diffusivity, this indicates that in the near field around the ESF, volumetric expansion is responsible for the attenuation of the signal. As the diffusivity is lowered, frictional forces become more significant. Phase lag in the signal 198 m from the source is observed for the case of 0.24 m^2/s gas diffusivity shown in Figure 6.1.4.

The response observed at Yucca Mountain is a combination of surface signal and ESF signal. Except where the ESF response is strong (i.e. near the ESF), it will be lost in the response to the surface. These simulations show that, even at high diffusivity, the response to only the ESF is strong within a few hundred meters of the ESF. Beyond this range, ESF interference is likely to be masked by the response to the surface signal. Conclusions are Q in that the simulated source signal is representative of actual ESF conditions.

6.2 X-Z simulations of ESF interference and fault effects

Atmospheric records were received from the USGS (J. Rousseau) for the period from mid November 1995 through mid March 1996. During this period the TBM did not pass any pneumatic monitoring boreholes. The atmospheric records are used to predict the pneumatic response in boreholes UZ#5, NRG-6, NRG-7a, SD-12 and UZ-7a using models calibrated to pneumatic data prior to mid November 1995. UZ#4 is not explicitly included as the pneumatic response is nearly identical to UZ#5.

All models used for this set of calibrations and predictions are two-dimensional in the X and Z directions (a change from the previous R-Z simulation). The stratigraphy is based on logs of each borehole and does not vary horizontally in the models. Two-dimensional X-Z models are used to simulate the effect of ESF and Fault interference with the surface barometric signal. The interference is observed primarily in the Topopah Spring unit.

The lateral and lower boundaries of these models are no-flow. The lateral boundaries are set more than 1000 m from the boreholes and ESF so that they have little effect on lateral propagation of ESF signals or signals that bypass the PTn via faults. A time varying pressure is applied at the upper boundary. Where appropriate, Time varying pressure is applied at a grid position corresponding to the location of the ESF.

The models are first calibrated to the vertical propagation of the surface barometric signal without consideration of any ESF interference. This calibration is presented in section 5.2. Where a fault provides a fast pneumatic pathway from the surface, such as the Ghost Dance Fault at UZ-7a and SD-12, a one-dimensional calibration is not possible and calibration is performed with a two-dimensional model. At those boreholes which had been passed by the TBM as of mid March 1996, a calibration is performed which includes the effect of ESF interference. Predictions are produced for the period from mid November to

mid March for all boreholes except SD-12 which did not come on line until the end of November. For SD-12 the calibration period is from the end of November to mid January, and predictions are from mid January to mid March. All conclusions in section 6.2 are Q when data from boreholes simulated are submitted.

6.2.1. UZ#5 Calibration and Prediction

UZ#4 and UZ#5 are the first USGS boreholes to record ESF interference. They are approximately 450m from the ESF and are located on an imbricate fault that crosses from Pagany Wash to Drill Hole Wash. This fault appears to communicate the ESF pneumatic signal to these boreholes. Except for one instrument station at the base of the Tiva Canyon unit the pneumatic records from both boreholes are nearly identical. Only UZ#5 is simulated.

The two-dimensional model used for this simulation is in a vertical plane that extends from the ESF past UZ#5 along the fault connecting them. The ESF is modeled as a line source perpendicular to the plane of the model (thus occupying a single element in the model grid). Properties corresponding to a fault are modeled in the TSw between the ESF and UZ#5. Beyond UZ#5, the properties are those of the bulk TSw estimated from inversion of NRG-7a data (see section 6.2.3).

Table 6.2.1.1 shows the permeability estimated for this simulation and the derived gas diffusivity of the formations. Figure 6.2.1.1 and 6.2.1.2 show the calibrated and predicted pneumatic response at stations A through H after ESF interference has begun. Stations A and B, in the TSw, are the lowest stations in the borehole and show the strongest response to ESF interference. Compared to the estimated bulk horizontal gas diffusivity of the TSw, the estimated gas diffusivity in the fault is 400 times larger. The gas diffusivity calculated for the fault may be low, as losses from the pressure signal to the fractured rock mass on either side of the fault are not included in the model.

Table 6.2.1.1.
Estimated gas permeability (k_g), prescribed drained porosity (n_g) and derived gas diffusivity (D_g) values used to simulate and predict pneumatic pressure response at UZ#5

Unit	Formation	k_g (darcy)	n_g	D_g (m^2/s)
Tiva	-Tpcpv2	6.3 e-1	1.00 e-2	3.1 e-1
Paintbrush	Tpcpv1/Tpbt4	2.5 e-1	1.68 e-1	7.4 e-3
	Tpy	4.0 e+0	1.79 e-1	1.1 e-1
	Tpbt3	1.6 e+0	1.71 e-1	4.6 e-2
	Tpp	2.5 e+0	1.92 e-1	6.5 e-2
	Tpbt2/Tptrv3	5.0 e-1	1.65 e-1	1.5 e-2
Topopah	Tptrv2-Tptpv2 (vertical)	4.0 e+0	1.00 e-2	2.0 e+0
--	Tptrv2-Tptpv2 (horizontal)	8.0 e-1	1.00 e-2	4.0 e-1
Calico Hills	CHnv	3.0 e-2	1.00 e-1	1.5 e-3
	CHnz	1.0 e-5	2.00 e-2	2.5 e-6
	PPv	3.0 e-2	1.00 e-1	1.5 e-3
	PPz	1.0 e-5	2.00 e-2	2.5 e-6
Fault		3.2 e+1	1.00 e-3	1.6 e+2

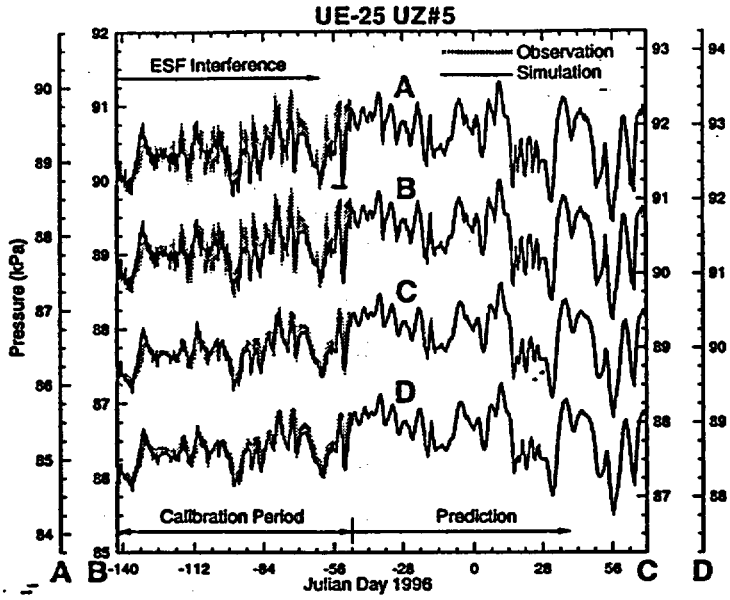

Figure 6.2.1.1. Comparison of simulation and observation in instrument stations A through D in borehole USW UZ#5. Note that the strongest response to ESF interference is at stations A and B. Station locations are A-Tptrn(top), B-Tptrv, C-Tpp(base), D-Tpp(top). Observed data obtained from USGS (Rousseau, 1996).

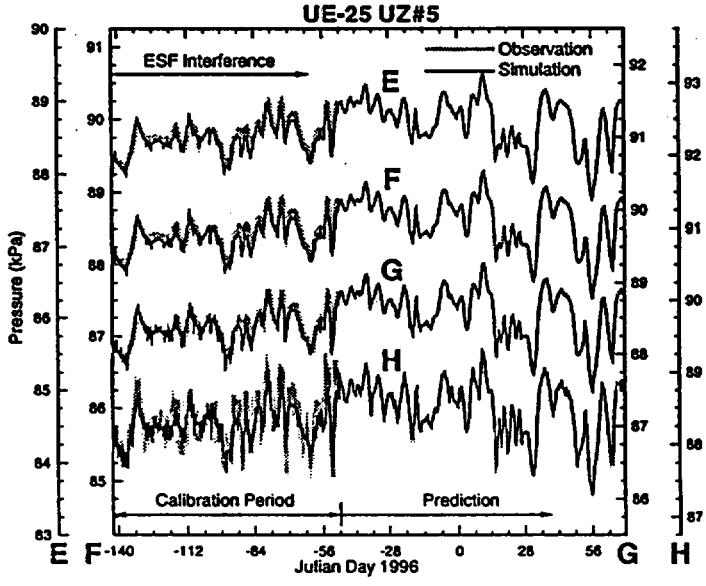

Figure 6.2.1.2. Comparison of simulation and observation at instrument stations E through H in borehole USW UZ#5. Station locations are E-Tpy(base), F-Tpy(top), G-Tpcpv, H-Tpc-plnc(base). Observed data obtained from USGS (Rousseau, 1996).

6.2.2 NRG-6 Calibration and Prediction

The pneumatic response at NRG-6 was first thought to have no ESF interference. A one-dimensional simulation was performed, and the calibrated response matched well with the observed response until the beginning of October 1995. After this point the observed response became slightly stronger than the simulated response. At the same time that the pneumatic response in NRG-6 became stronger, the TBM penetrated the Drill Hole Wash Fault.

The two-dimensional model for NRG-6 is oriented in a vertical plane running from the intersection of the ESF and Drill Hole Wash fault to NRG-6. The ESF is modeled as a line source perpendicular to the plane of the model.

The first hypothesis that was tested with this model was that the fault acted as a pneumatic insulator, so that the ESF signal was not recorded at NRG-6 until the fault was penetrated, and the signal allowed to propagate through 720 m of TSw. However, for the ESF signal to produce the observed response, a horizontal gas diffusivity of approximately 10 m^2/s (k = 20 d, with f = 0.01) is necessary in the TSw. This is 25 times larger than the horizontal gas diffusivity estimated for the TSw from analysis of NRG-7a pneumatic response (see section 6.2.3). With such high estimates of diffusivity, it seems more likely that the ESF signal is communicated along the Drill Hole Wash Fault to within 100 m of NRG-6.

Without changing the two-dimensional model grid, the first 610 m from the ESF to the borehole are modeled as a fault, and the remaining 110 m are modeled with bulk TSw parameters. This setup approximates an L shaped pathway along the fault from the ESF and then through intact TSw to the borehole.

Table 6.2.2.1.
Estimated gas permeability (k_g), prescribed drained porosity (n_g) and derived gas diffusivity (D_g) values used to simulate and predict pneumatic pressure response at NRG-6.

Unit	Formation	k_g (darcy)	n_g	D_g (m^2/s)
Tiva	-Tpcpv2	1.0 e+1	1.00 e-2	5.0 e+0
Paintbrush	Tpcpv1/Tpbt4	1.6 e-1	1.68 e-1	4.7 e-3
	Tpy	NP	NP	NP
	Tpbt3	3.4 e-2	1.71 e-1	9.8 e-4
	Tpp	3.0 e+0	1.92 e-1	7.9 e-2
	Tpbt2/Tptrv3	1.9 e-1	1.65 e-1	5.7 e-3
Topopah	Tptrv2-Tptpv2 (vertical)	4.0 e+0	1.00 e-2	2.0 e+0
	Tptrv2-Tptpv2 (horizontal)	7.9 e-1	1.00 e-2	3.9 e-1
Calico Hills	CHnz	1.0 e-5	5.00 e-2	9.9 e-7
Fault		2.0 e+1	1.00 e-2	9.9 e+0
NP=formation Not Present				

Table 6.2.2.1 shows the gas diffusivity estimated for the L shaped system. The fault is considered to be a significant pneumatic pathway only within the welded Topopah Spring unit. It does not create a significant pneumatic pathway through the PTn. Figures 6.2.2.1 and 6.2.2.2 show the match between the calibrated simulation and observation.

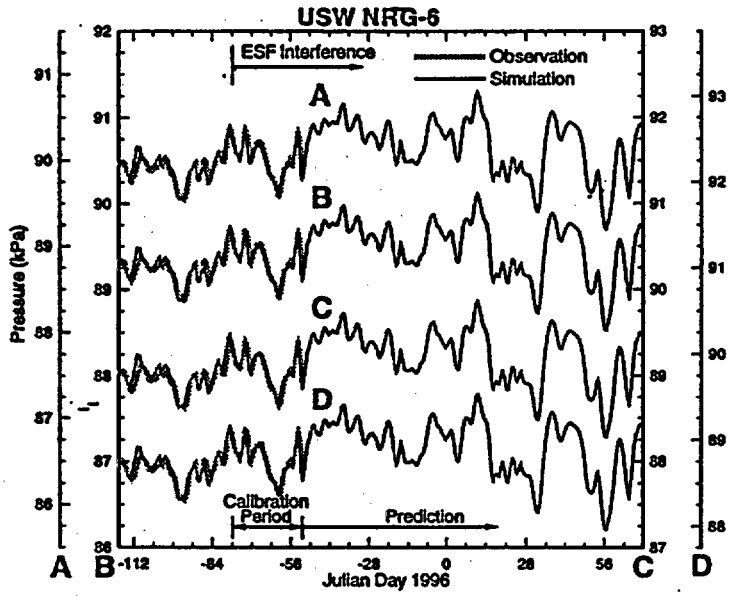

Figure 6.2.2.1. Comparison of simulation and observation in instrument stations A through D in borehole USW NRG-6. Station locations are A-Tptpmn, B-Tptpul, C-Tptpul, D-Tptrn. Observed data obtained from USGS (Rousseau, 1996).

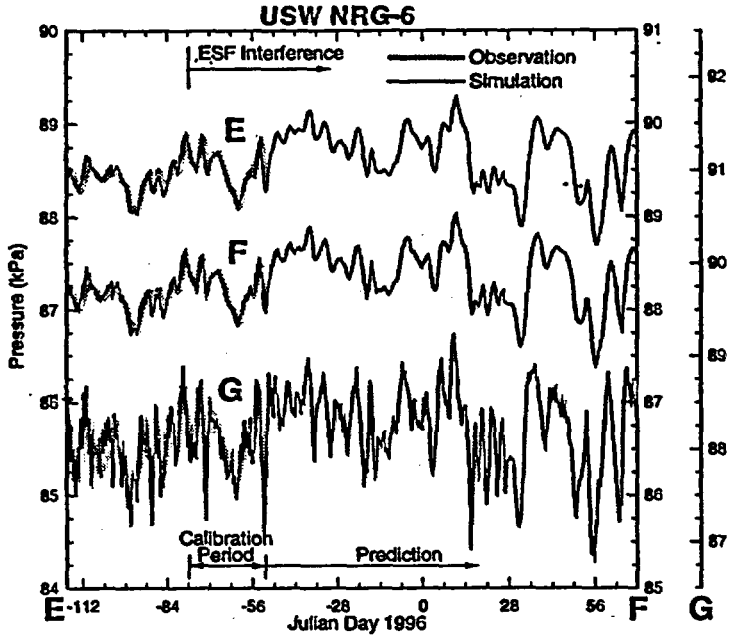

Figure 6.2.2.2. Comparison of simulation and observation in instrument stations E through G in borehole USW NRG-6. Station locations are E-Tptrv, F-Tpp, G-Tpcplnc. Observed data obtained from USGS (Rousseau, 1996).

As with the simulation of UZ#5, the pneumatic diffusivity of the fault may be underestimated because losses from the fault are not considered. This may be even more important to this simulation, as it is the losses from the fault that are recorded at NRG-6. Remember that NRG-6 is not in the Drill Hole Wash fault but is approximately 100 m outside the fault.

6.2.3. NRG-7a Calibration and Prediction

The grid used to simulate NRG-7a is oriented in a vertical plane passing through NRG-7a and perpendicular to the alignment of the ESF nearest NRG-7a. The ESF is modeled as a line source perpendicular to the plane of the model.

Figures 6.2.3.1 and 6.2.3.2 show the pneumatic response predicted for instrument stations A through E in NRG-7a. Prior to the calibration period the simulation and observations do not match because the simulation includes the effect of ESF interference while the observations do not yet show the full effect of ESF interference. The TBM passed closest to NRG-7a on October 25, 1995 (67 days before 1/1/96). The increasing effect of the ESF on instrument stations A-C

can be seen in Figure 6.2.3.1. The phase-difference between the simulation and observations decreases from day -99 to day -70 as the TBM approached the closest point to the borehole. After the TBM has passed the borehole the signal does not appear to get any stronger. The magnitude of the pneumatic response observed in the Topopah Spring instrument stations, A-C, can be correlated to the vertical distance from the ESF to the instrument station. Station A is at approximately the same level as the ESF and shows the largest response to the ESF signal. Station C is 85 meters above station A, and the response at C is approximately 65% of the response at station A. In order to simulate the response at the Topopah Spring stations it is necessary to introduce anisotropy into the permeability field. Using a drained porosity of 1% the observations were best fit with a vertical permeability of 4.0 d and a horizontal permeability of 0.8 d. Table 6.2.3.1 shows the calibrated parameters used for prediction of the pneumatic response.

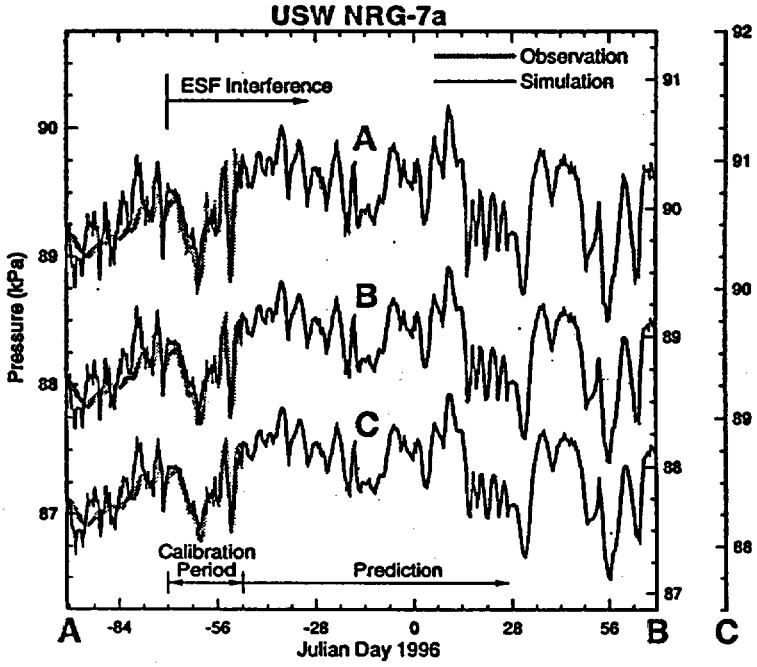

Figure 6.2.3.1. Comparison of simulation and observation in instrument stations A through C in borehole USW NRG-7a. Note that ESF interference is strongest at instrument station A and gets weaker at stations B and C, which are further from ESF. Station locations are A-Tptrl, B-Tptrl/Tptrn, C-Tptrn. Observed data obtained from USGS (Rousseau, 1996).

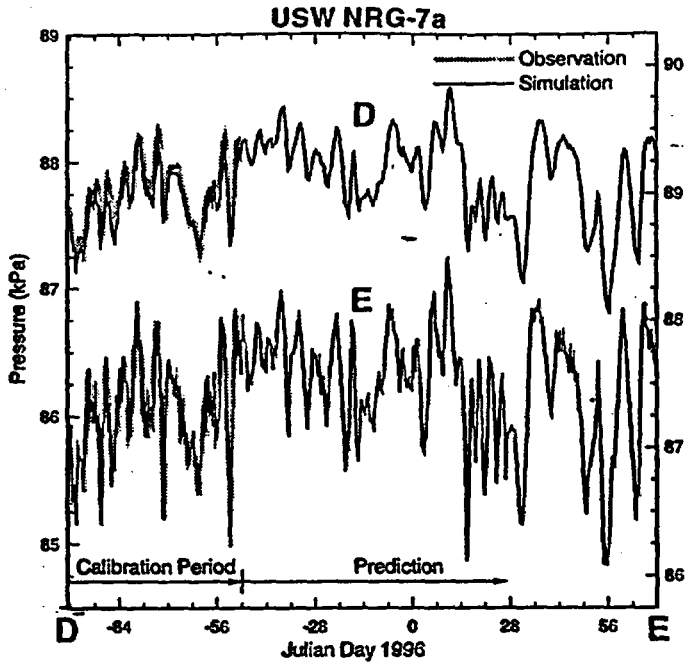

Figure 6.2.3.2. Comparison of simulation and observation in instrument stations D and E in borehole USW NRG-7a. Station locations are D-Tpy, E-Tpcplnh. Observed data obtained from USGS (Rousseau, 1996).

Table 6.2.3.1.
Estimated gas permeability (k_g), prescribed drained porosity (n_g) and derived gas diffusivity (D_g) values used to simulate and predict pneumatic pressure response at NRG-7a.

Unit	Formation	k_g (darcy)	n_g	D_g (m^2/s)
Tiva	-Tpcpv2	1.0 e+1	1.00 e-2	5.0 e+0
Paintbrush	Tpcpv1/Tpbt4	1.3 e-1	1.68 e-1	3.9 e-3
	Tpy	6.0 e-1	1.79 e-1	1.7 e-2
	Tpbt3	2.8 e-2	1.71 e-1	8.1 e-4
	Tpp	2.5 e+0	1.92 e-1	6.6 e-2
	Tpbt2/Tptrv3	1.6 e-1	1.65 e-1	4.8 e-3
Topopah	Tptrv2-Tptpv2 (vertical)	4.0 e+0	1.00 e-2	2.0 e+0
	Tptrv2-Tptpv2 (horizontal)	7.9 e-1	1.00 e-2	3.9 e-1
Calico Hills	CHnz	1.0 e-5	5.00 e-2	9.9 e-7

The anisotropy estimated for the TSw is consistent with a conceptual model of fracturing in the TSw. Vertical cooling fractures provide most of the pneumatic permeability in the TSw. Less pneumatic permeability is associated with horizontal fracturing which occurs mainly in conjunction with sub layer contacts (Simmons et al., 1996). This fracture system means that pneumatic permeability is stronger in the vertical direction because connectivity in the fracture networks is larger in the vertical direction.

6.2.4. SD-12 Calibration and Prediction

The grid used to simulate SD-12 is oriented in a vertical plane passing through SD-12 and perpendicular to both the alignment of the main drift of the ESF and the surface trace of the Ghost Dance fault. An ESF boundary condition is not included in this section.

Qualitative analysis of the observations from SD-12 shows two areas of interest. The bottom two stations, A and B, show little response to the barometric signal. These stations are located in the Calico Hills Vitric unit and the moderately welded portion of the base of theTopopah Spring unit, respectively. Station C, located in the Topopah Spring Lower Non-Lithophysal zone, has much more pneumatic response than the stations below it. The pneumatic response is similar in degree of amplitude attenuation to the stations above it in the Topopah Spring, however the phase lag is less than other stations in the Topopah Spring. Other stations in SD-12 show typical pneumatic response with increased amplitude attenuation and phase lag downward through the Paintbrush non welded unit.

A conceptual model that explains the non-typical pneumatic response at the base of the Topopah Spring relies on the proximity of SD-12 to the Ghost Dance Fault. Fractures from the fault zone create a fast pneumatic pathway from the surface that intersects the borehole at approximately the depth of instrument station C. It is also possible that there is increased horizontal fracturing at the base of the Topopah Spring, in and/or just above the vitrophyre, which intersects the fault zone and creates a pneumatic pathway from the fault zone to instrument station C. The intersection of the fault zone and the non-welded layer from the base of the Topopah Spring downward creates a zone of very high saturation (possibly perched water) above and/or around stations A and B. The high saturation makes the gas diffusivity effectively zero, blocking the majority of the barometric signal.

In order to simulate this system the model includes a fault as a fast pneumatic pathway from the surface to the base of the Topopah Spring and a highly fractured layer at and just above the Topopah Spring Basal Vitrophyre to conduct the signal to station C. Table 6.2.4.1 shows the estimated gas diffusivity of the fault zone and the highly fractured layer as well as other portions of the model. At the boundary between the vitrophyre (Tptpv3) and the moderately to non-welded vitric base of the Topopah Spring (Tptpv2-1), connections between grid elements are removed to simulate the extremely low gas diffusivity in a

high saturation or perched water zone. The extent of the simulated high saturation zone and the gas diffusivity below it are varied to match observations at stations A and B. The best match in the calibration period was achieved with a lateral extent of 90 m (45 m on either side of the borehole) and gas diffusivity of the underlying layer as shown in Table 6.2.4.1. Figures 6.2.4.1-through 6.2.4.4 show comparisons of the simulation and observations for both the calibration period and the prediction period. There is no ESF interference during the calibration or prediction period.

Table 6.2.4.1.
Estimated gas permeability (k_g), prescribed drained porosity (n_g) and derived gas diffusivity (D_g) values used to simulate and predict pneumatic pressure response at SD-12.

Unit	Formation	k_g (darcy)	n_g	D_g (m^2/s)
Tiva	-Tpcpv2	1.0 e+1	1.00 e-2	5.0 e+0
Paintbrush	Tpcpv1/Tpbt4	1.0 e+0	1.68 e-1	3.1 e-2
	Tpy	NP	NP	NP
	Tpbt3	2.2 e-1	1.71 e-1	6.5 e-3
	Tpp	2.0 e+1	1.92 e-1	5.3 e-1
	Tpbt2/Tptrv3	7.1 e-2	1.65 e-1	2.1 e-3
Topopah	Tptrv2-Tptpln (vertical)	4.0 e+0	1.00 e-2	2.0 e+0
	Tptrv2-Tptpln (horizontal)	8.0 e-1	1.00 e-2	4.0 e-1
	Tptpv3 (vertical)	1.0 e-4	1.00 e-2	5.0 e-5
	Tptpv3 (horizontal)	1.0 e+1	1.00 e-2	5.0 e+0
Calico Hills	Tptpv2-CHnv	3.0 e-2	1.00 e-1	1.5 e-3
	CHnz	1.0 e-5	2.00 e-2	2.5 e-6
	PPv	3.0 e-2	1.00 e-1	1.5 e-3
	PPz	1.0 e-5	2.00 e-2	2.5 e-6
Fault	TCw (∥ fault)	1.0 e+1	1.00 e-2	5.0 e+0
	TCw (⊥ fault)	1.0 e+1	1.00 e-2	5.0 e+0
	Tpcpv1/Tpbt4 (∥ fault)	5.0 e+0	1.68 e-1	1.5 e-1
	Tpcpv1/Tpbt4 (⊥ fault)	1.0 e-4	1.68 e-1	3.0 e-6
	Tpbt3 (∥ fault)	5.0 e+0	1.71 e-1	1.5 e-1
	Tpbt3 ⊥ fault)	1.0 e-4	1.71 e-1	2.9 e-6
	Tpp (∥ fault)	5.0 e+0	1.92 e-1	1.3 e-1
	Tpp (⊥ fault)	1.0 e-4	1.92 e-1	2.6 e-6
	Tpbt2/Tptrv3 (∥ fault)	5.0 e+0	1.65 e-1	1.5 e-1
	Tpbt2/Tptrv3 (⊥ fault)	1.0 e-4	1.65 e-1	3.0 e-6
	TSw (∥ fault)	1.0 e+1	1.00 e-2	5.0 e+0
	TSw (⊥ fault)	1.0 e-4	1.00 e-2	5.0 e-5
	Tptpv3 (∥ fault)	1.0 e+1	1.00 e-2	5.0 e+0
	Tptpv3 ⊥ fault)	1.0 e+1	1.00 e-2	5.0 e+0
	CHnv/PPv (∥ fault)	3.2 e-2	1.00 e-1	1.6 e-3
	CHnv/PPv ⊥ fault)	3.2 e-2	1.00 e-1	1.6 e-3
	CHnz/PPz (∥ fault)	1.0 e-5	2.00 e-2	2.5 e-6
	CHnz/PPz ⊥ fault)	1.0 e-5	2.00 e-2	2.5 e-6
NP=formation Not Present				

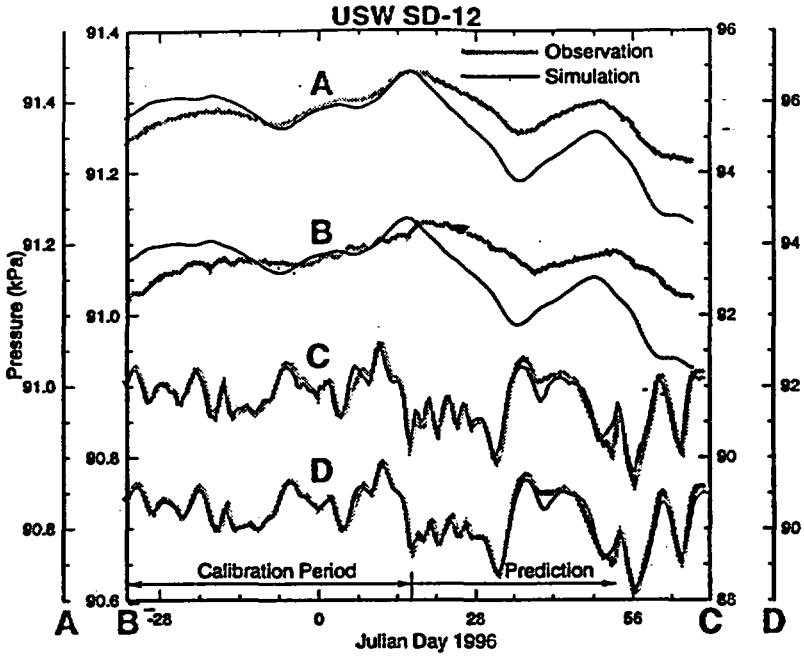

Figure 6.2.4.1. Comparison of simulation and observation in instrument stations A through D in borehole USW SD-12. Station locations are A-CHnv(Ta unit 4), B-Tptpv2, C-Tptpln(base), D-Tptpln(top). Note that pressure scale for stations A and B is not the same as for C and D. Observed data obtained from USGS (Rousseau, 1996).

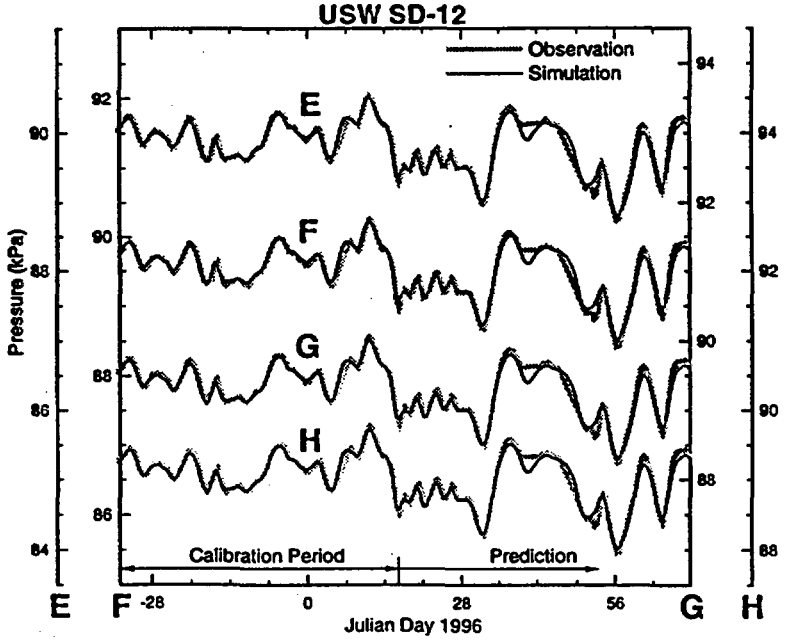

Figure 6.2.4.2. Comparison of simulation and observation in instrument stations E through H in borehole USW SD-12. Station locations are E-Tptpll, F-Tptpll, G-Tptpmn, H-Tptpmn. Observed data obtained from USGS (Rousseau, 1996).

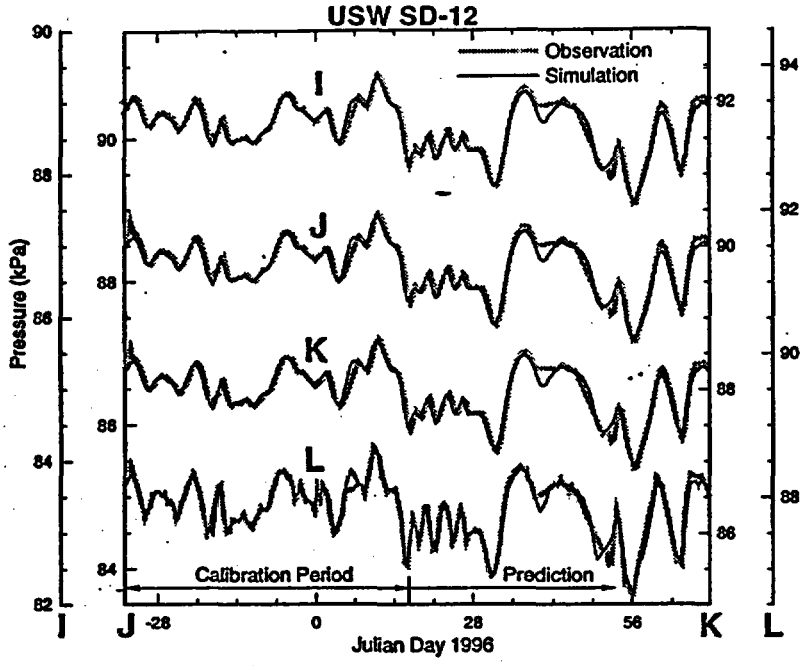

Figure 6.2.4.3. Comparison of simulation and observation in instrument stations I through L in borehole USW SD-12. Station locations are I-Tptpul, J-Tptrl, K-Tptrl, L-Tptrv1. Observed data obtained from USGS (Rousseau, 1996).

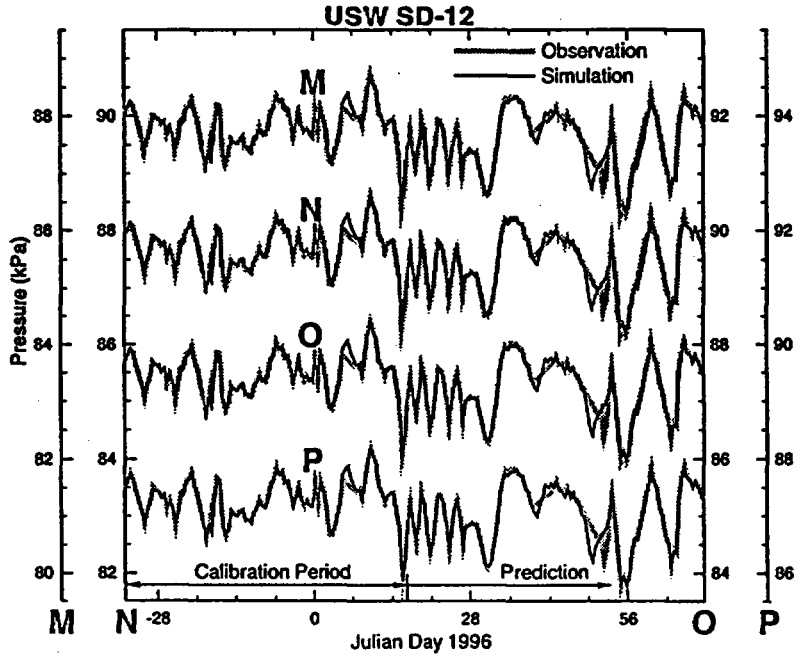

Figure 6.2.4.4. Comparison of simulation and observation in instrument stations M through P in borehole USW SD-12. Station locations are M-Tpcpv, N-Tpcplnc, O-Tpcplnh, P-Tpcpmn (base). Observed data obtained from USGS (Rousseau, 1996).

6.2.5. UZ-7a Calibration and Prediction

Borehole UZ-7a is located within the surface expression of the Ghost Dance Fault zone. Qualitative analysis of the pneumatic response observed in UZ-7a suggests that the seven upper instrument stations are all in the fault zone. There is increasing amplitude attenuation with depth observed in the signals, but there is no apparent phase lag between the signals observed at any of the upper seven stations. There is a phase lag observable between signals from the upper seven stations and signals from the lower three stations. The lower three stations would then appear to be outside the fault zone, so that they are not in direct communication with the surface barometric signal via the fault zone.

The grid used to simulate UZ-7a is oriented in a vertical plane passing through UZ-7a and perpendicular to the alignment of the main drift of the ESF and the surface trace of the Ghost Dance fault. The Ghost Dance Fault zone is represented by a 30 m wide fault zone which is inclined at 80 to horizontal. The vertical string of instrument stations in UZ-7a is modeled so that the top seven stations are in the fault zone and the bottom three are outside the fault zone. An ESF boundary condition is not included in this simulation.

Table 6.2.5.1.
Estimated gas permeability (k_g), prescribed drained porosity (n_g) and derived gas diffusivity (D_g) values used to simulate and predict pneumatic pressure response at UZ-7a

Unit	Formation	k_g (darcy)	n_g	D_g (m^2/s)
Tiva	-Tpcpv2	1.0 e+1	1.00 e-2	5.0 e+0
Paintbrush	Tpcpv1/Tpbt4	2.6 e-1	1.68 e-1	7.8 e-3
	Tpy	NP	NP	NP
	Tpbt3	5.6 e-2	1.71 e-1	1.6 e-3
	Tpp	2.0 e+1	1.92 e-1	5.3 e-1
	Tpbt2/Tptrv3	3.2 e-1	1.65 e-1	9.5 e-3
Topopah	Tptrv2-Tptpv2 (vertical)	4.0 e+0	1.00 e-2	2.0 e+0
	Tptrv2-Tptpv2 (horizontal)	8.0 e-1	1.00 e-2	4.0 e-1
Calico Hills	CHnv	3.0 e-2	1.00 e-1	1.5 e-3
	CHnz	1.0 e-5	2.00 e-2	2.5 e-6
	PPv	3.0 e-2	1.00 e-1	1.5 e-3
	PPz	1.0 e-5	2.00 e-2	2.5 e-6
Fault	TCw (∥ fault)	2.0 e+1	1.00 e-2	9.9 e+0
	TCw (⊥ fault)	2.0 e-1	1.00 e-2	9.9 e-2
	Tpcpv1/Tpbt4 (∥ fault)	2.0 e-1	1.68 e-1	5.9 e-3
	Tpcpv1/Tpbt4 ⊥ fault)	2.0 e+0	1.68 e-1	5.9 e-2
	Tpbt3 (∥ fault)	2.0 e-1	1.71 e-1	5.8 e-3
	Tpbt3 (⊥ fault)	2.0 e+0	1.71 e-1	5.8 e-2
	Tpp (∥ fault)	2.0 e-1	1.92 e-1	5.2 e-3
	Tpp ⊥ fault)	2.0 e+0	1.92 e-1	5.2 e-2
	Tpbt2/Tptrv3 (∥ fault)	2.0 e-1	1.65 e-1	6.0 e-3
	Tpbt2/Tptrv3 (⊥ fault)	2.0 e+0	1.65 e-1	6.0 e-2
	TSw (∥ fault)	2.0 e+1	1.00 e-2	9.9 e+0
	TSw (⊥ fault)	2.0 e-1	1.00 e-2	9.9 e-2
	CHnv/PPv (∥ fault)	1.0 e-2	1.00 e-1	5.0 e-4
	CHnv/PPv ⊥ fault)	1.0 e-2	1.00 e-1	5.0 e-4
	CHnz/PPz (∥ fault)	1.0 e-2	2.00 e-2	2.5 e-3
	CHnz/PPz (⊥ fault)	1.0 e-2	2.00 e-2	2.5 e-3
NP=formation Not Present				

Table 6.2.5.1 shows the estimated gas diffusivity for all portions of the model. Note that the fault zone is layered similarly to the intact tuff. Like observations from other boreholes in intact tuff, most of the amplitude attenuation occurs in the Paintbrush non-welded unit portion of the fault. Figures 6.2.5.1 through 6.2.5.3 show the comparison of observation and calibrated simulation for the calibration period and the prediction period. Note in Figure 6.2.5.2 the relative amplitude attenuation at stations G, F and E, above, below and within the Paintbrush non-welded portion of the fault. There is no ESF interference during the calibration or prediction periods for this borehole.

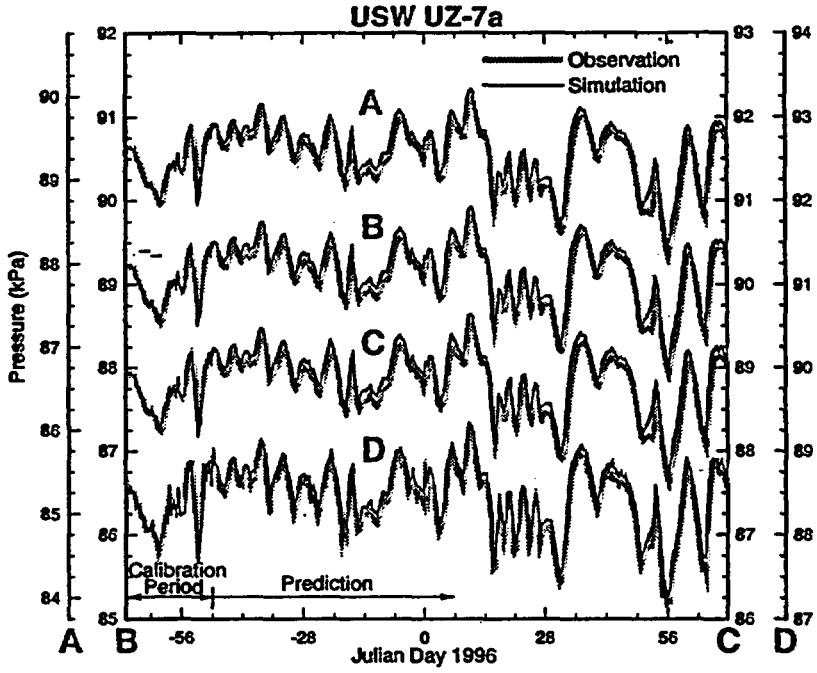

Figure 6.2.5.1. Comparison of simulation and observation in instrument stations A through D in borehole USW UZ-7a. Station locations are A-Tptpmn, B-Tptpmn, C-Tptpmn, D-Tptprn. Observed data obtained from USGS (Rousseau, 1996).

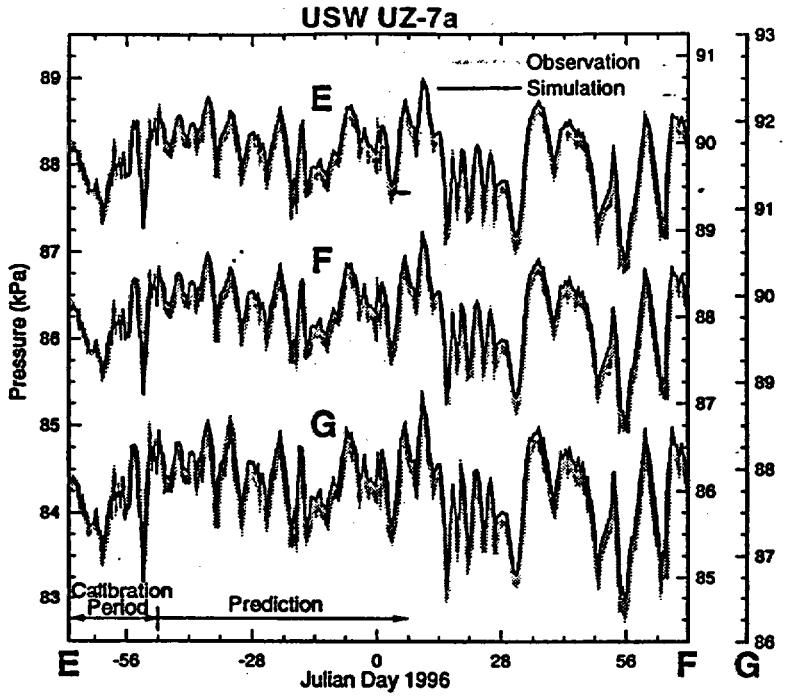

Figure 6.2.5.2. Comparison of simulation and observation in instrument stations E through G in borehole USW UZ-7a. Station locations are E-Tptrn, F-Tpp, G-Tpcpv. Observed data obtained from USGS (Rousseau, 1996).

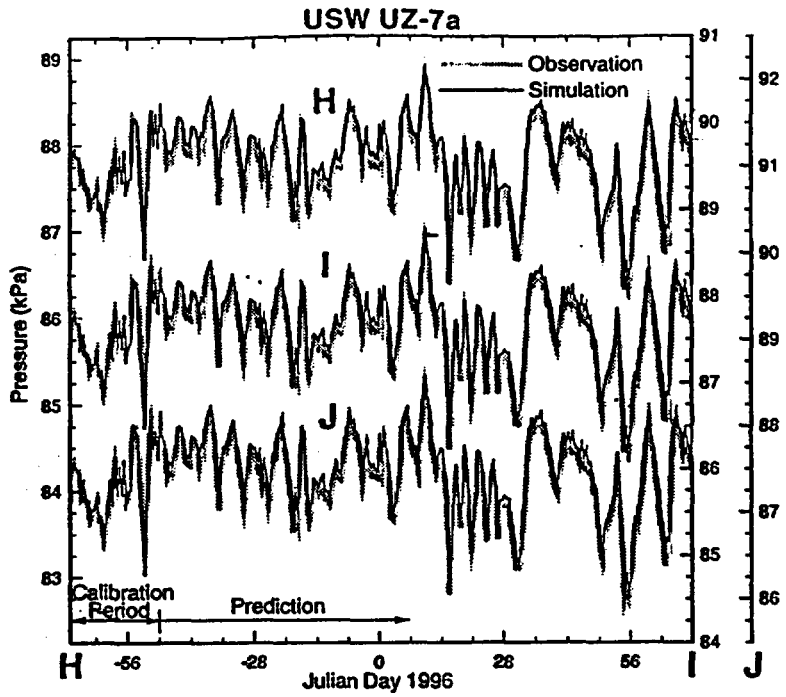

Figure 6.2.5.3. Comparison of simulation and observation in instrument stations H through J in borehole USW UZ-7a. Station locations are H-Tpcplnc, I-Tpcplnh, J-Tpcpll. Observed data obtained from USGS (Rousseau, 1996).

The estimated diffusivity of the welded portions of the Ghost Dance fault zone are the same as the estimated diffusivity for the welded portion of the Drill Hole Wash fault zone and is approximately 16 times lower than the diffusivity estimated for the welded portion of the imbricate fault at UZ#5. In this model, however, losses from the fault are accounted for. It appears that the diffusivity of the welded portion of the Ghost Dance fault zone is much less than the other two faults characterized in this section (because we expect that when fault losses are included in models of the Drill Hole Wash fault zone and the UZ#5 imbricate fault, the diffusivity will need to be much higher).

Note that in this simulation the diffusivity perpendicular to the plane of the fault, in the TSw portion of the fault zone, is four times less than the horizontal diffusivity of the TSw. The strength of the interaction between the fault and the TSw had to be reduced so that the signal propagating down the fault did not interfere too strongly with the response observed at stations A-C, outside the fault.

6.3. Discussion

All of the calibrated simulations represent one interpretation of the observed pneumatic response. These solutions are in no way unique. Where possible borehole geologic controls are used to define stratigraphy. Below the

bottom of the borehole, stratigraphy defined by Bandurraga et al. (1996a) is used. The location and width of fault zones in the subsurface is not well characterized, so there are few controls on the geometry used for the fault zones in these simulations.

As all of these simulations represent transient phenomena, gas diffusivity is the parameter with the most relevance. Reported permeability is only an estimate based on the effective drained porosity used in the simulations. Re-estimation of the permeability may be warranted if better estimates of effective drained porosity become available. Effective drained porosity is defined here as the porosity that equivalently represents the portion of drained fracture and matrix porosity that affects the transient pneumatic response in the mountain. The effective drained porosity may also be a function of the frequency of the driving signal. Higher frequency signals may be less affected by matrix porosity than lower frequency signals because of finite pressure diffusion rates into the matrix.

Except for NRG-7a there appears to be a fast pneumatic pathway in the form of a fault that affects the pneumatic response in the boreholes simulated in this section. SD-12 and UZ-7a both appear to be affected by the Ghost Dance Fault zone that conducts the surface signal deep into the Topopah Spring unit. This fast pneumatic pathway does not appear to significantly affect pneumatic response very far outside the fault zone. In modeling the Ghost Dance Fault zone it was necessary to give much lower permeability to the direction perpendicular to the fault plane. At UZ#5 and NRG-6 no evidence of nearby faults acting as fast pneumatic pathways was evident until the ESF penetrated the faults that are near the boreholes (i.e. UZ#5 imbricate fault and Drill Hole Wash fault). Estimation of the hydrologic thickness of the PTn at UZ#5 (see section 5.2) indicated atypical behavior, but this alone was not attributed to a fault acting as a fast pneumatic pathway. The ESF signal is transmitted over long distances along these fault zones. At the imbricate fault that intersects UZ#5 the ESF signal is transmitted more than 400 m. At NRG-6 the signal is transmitted more than 600 m along the Drill Hole Wash Fault zone and is still strong enough to be observed more than 100 m away from the fault. It must be restated that the discovery of ESF interference at NRG-6 was made only by comparison of observations to simulation that did not include ESF interference (see Figure 5.2.3). An analysis of the fault effects at UZ#5 and NRG-6 with a three-dimensional grid is discussed in the following section. Observations at UZ-7a, UZ#5, and NRG-6 show that the faults have a lower diffusivity when they penetrate the Paintbrush non-welded unit.

Due to the fact that four of the five boreholes are affected by faults it is not possible to draw any generalizations about the bulk rock properties further than two observed generalizations: 1) the Paintbrush non-welded unit has a lower gas diffusivity than the overlying Tiva or the underlying Topopah, and 2)

the Tpy and Tpp, where present, have higher diffusivity than the other PTn sub-layers.

7. Three-dimensional simulation and characterization

With satisfactory data sets from the one-dimensional and two-dimensional simulations, a three-dimensional simulation using a site-scale model was undertaken. The goals of the three-dimensional simulation are to test conclusions made based on the one and two-dimensional simulations were it is believed that the pneumatic flow is fully three-dimensional and the third dimension of flow is significant. Flow near NRG-7a is one such case. The ESF is assumed to approximate a line source in the two-dimensional simulations, but at NRG-7a the ESF is curving around the borehole. Another case is boreholes NRG-6 and UZ#5 which experience ESF interference via faults. As stated in the previous section, the pneumatic signal is expected to experience losses as it propagates along the fault. These losses were not simulated with the two-dimensional models. Conclusions regarding the Ghost Dance fault at UZ-7a will also be tested, as well as, analyzing ONC#1 pneumatic response near the Bow Ridge fault (a type of structure believed to be pneumatically similar to the Ghost Dance fault).

A three-dimensional grid is constructed using the geologic model described in Bandurraga et al. (1996a). The model includes elements along the alignment of the ESF, along the traces of the major faults. Elements are also centered on boreholes important to this investigation (i.e. NRG#4, UZ#5, NRG-6, NRG-7a, SD-9, SD-12, UZ-7a, SD-7, and ONC#1). The model also explicitly includes vertical offsets of major faults. Details of the methodology used to produce this grid and other grids for the unsaturated zone flow model are found in Haukwa et al. (1996). For the purposes of pneumatic simulations, three modifications are made to the grid. Three directions of anisotropy are introduced into the fault zones. The directions are vertical and horizontal parallel to the plane of the fault and horizontal perpendicular to the plane of the fault. Individual faults are separated vertically into four layers based on hydrogeologic unit (TCw, PTn, TSw, and below the TSw). Each layer is assigned only one pneumatic diffusivity tensor (three orthogonal pneumatic permeability vectors, and one value of drained porosity). Boundary elements are also added along the alignment of the ESF so that the presence of the ESF in the subsurface can be simulated. Like other numerical simulations in this report, the lateral and lower boundaries of the model are no-flow, and a time varying pressure is applied at the upper boundary and the ESF boundary (when appropriate).

Note in Figure 7.1.1 that the elements along the alignment of the simulated faults are not a constant width. Nor do they reflect the assumed width of the fault zone. In the case of the Ghost Dance fault zone, the modeled width of the fault zone and the assumed width of the fault zone are reasonably similar. The

models of the Drill Hole Wash fault zone and the imbricate fault at UZ#5 are much wider than the widths identified where the faults intersect the ESF (Day et al., 1996; Rousseau and Patterson, 1996b). By allowing anisotropy parallel and perpendicular to the fault, the effect of the modeled width of the fault zones should be minimized. Diffusivity in the direction perpendicular to the fault is the same as the horizontal diffusivity of the bulk tuff (fractured or unfractured).

Due to the large scale of the three-dimensional model, small scale interactions are not simulated as accurately as in the more refined one and two-dimensional models. Simulation of ESF interference at boreholes which are very close to the ESF alignment (i.e. NRG#4, NRG-7a, SD-9, SD-12, and SD-7) and the resultant estimates of pneumatic diffusivity are not expected to be as good as the one and two-dimensional simulations. The level of refinement in the three-dimensional grid means that only a few elements simulate the ESF interference at the nearby boreholes. More importantly, for large scale interactions, such as ESF interference via faults at NRG-6 and UZ#5, the three-dimensional model provides better estimates of pneumatic diffusivity in the faults. The three-dimensional simulations and estimates for boreholes near the ESF are also useful because they indicate how best to integrate the pneumatic model with the moisture flow model of the unsaturated zone. Finsterle et al. (1996) and Bandurraga et al. (1996b) discuss integrated pneumatic/moisture flow models with the unsaturated zone flow model.

Boreholes NRG#4, UZ#5, NRG-6, NRG-7a, SD-9, SD-12, UZ-7a, SD-7 and ONC#1 are used to calibrate the three-dimensional model. In order to match the pneumatic response at each of the boreholes, zones are extended several hundred meters around each of the boreholes and a unique set of material properties are assigned to each of these zones. This is an approximation of the heterogeneous pneumatic diffusivity field that is expected to exist within the mountain. Figures 7.1 through 7.5 show the matches between the calibrated three-dimensional simulation and the recorded pneumatic response in several boreholes.

For the three-dimensional simulation there are 210 independent values of diffusivity because of the zones around each of the boreholes and the four faults simulated. Initially all of the diffusivity values were set to values indicated by the one and two-dimensional estimations. These diffusivity values were varied where necessary in order to produce a match between the simulation and observations. In general this meant that diffusivity values were varied in the PTn and TSw, as this is where most of the pneumatic response data were taken. Rather than present the estimated diffusivity as a table, figures are presented showing contours of diffusivity along with discussion of the important results of the three-dimensional calibration in sections 7.1 and 7.2.

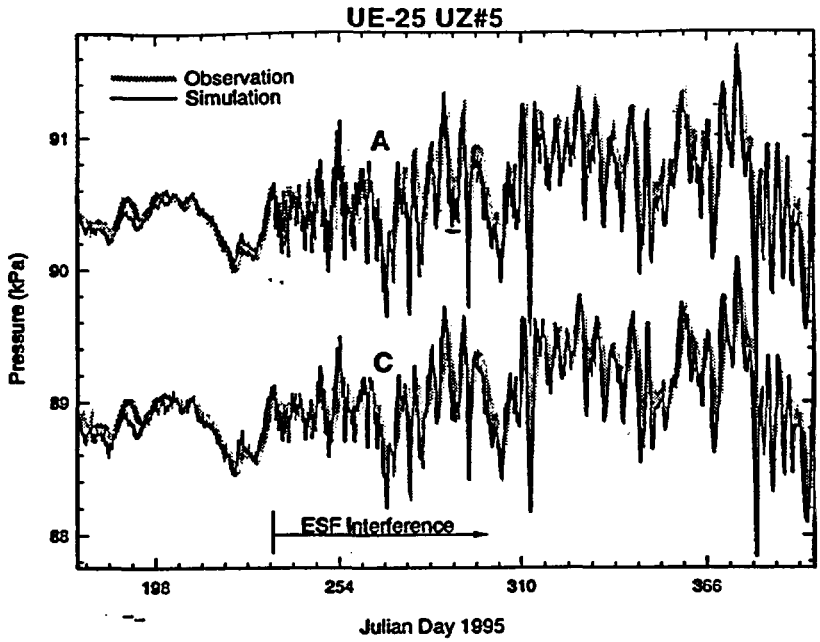

Figure 7.1. Matches between the three-dimensional simulation and observations in borehole UZ#5 at instrument stations A and C. Observations provided by USGS (Rousseau, 1996).

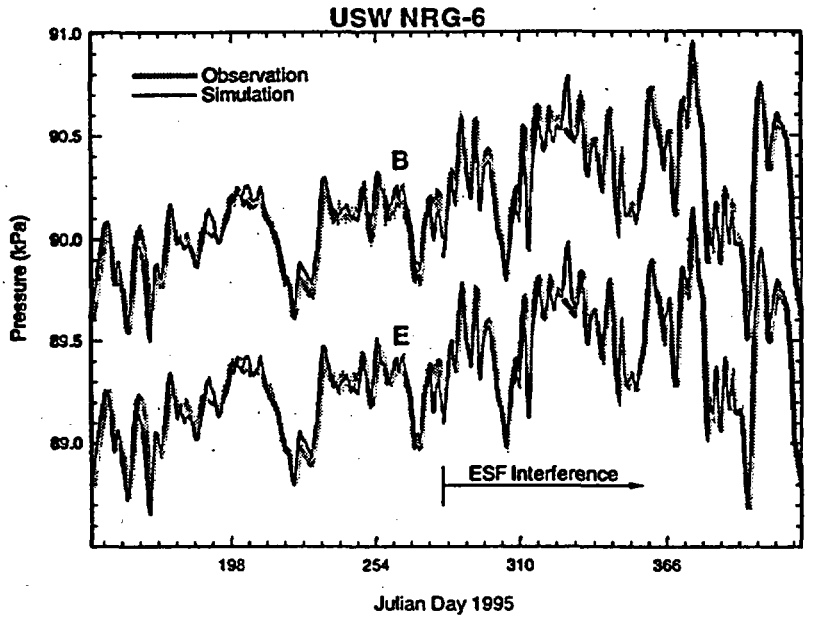

Figure 7.2. Matches between the three-dimensional simulation and observations in borehole NRG-6 at instrument stations B and E. Observations provided by USGS (Rousseau, 1996).

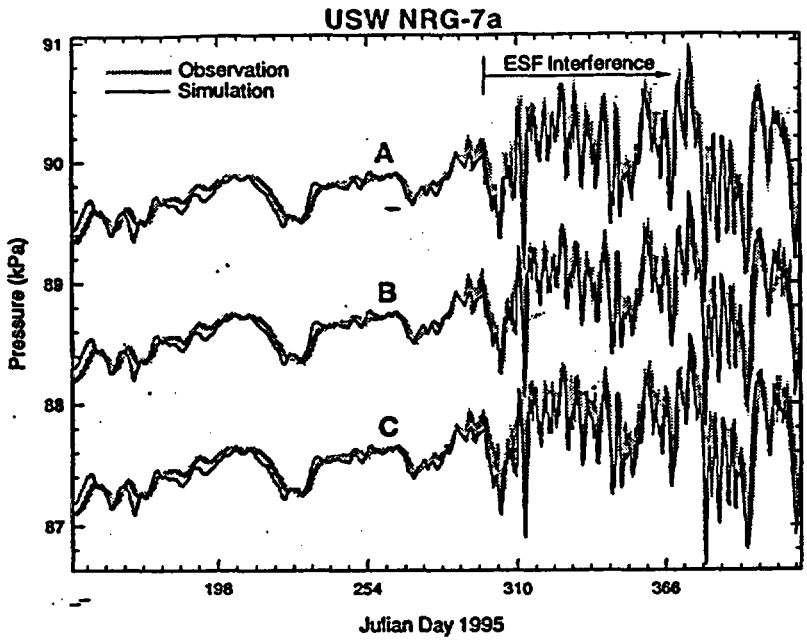

Figure 7.3. Matches between the three-dimensional simulation and observations in borehole NRG-7a at instrument stations A, B and C. Observations provided by USGS (Rousseau, 1996).

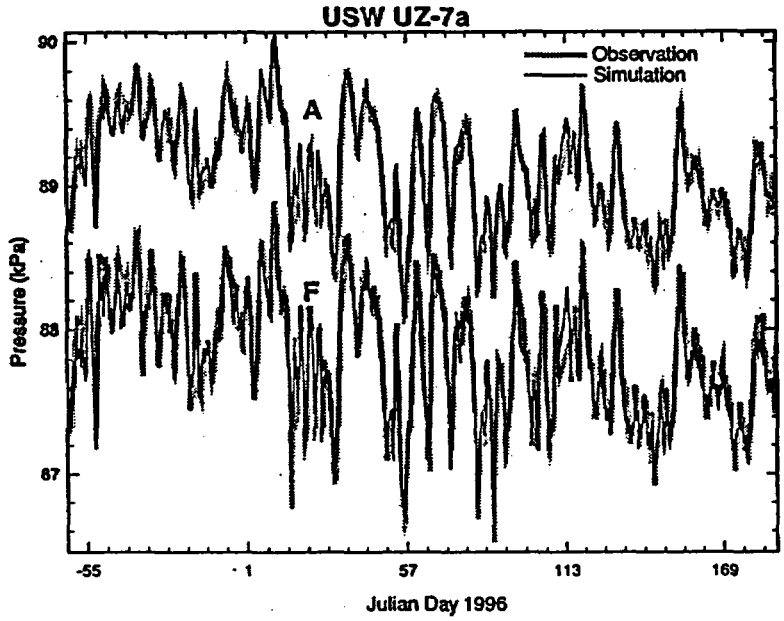

Figure 7.4. Matches between the three-dimensional simulation and observations in borehole UZ-7a at instrument stations A and F. Observations provided by USGS (Rousseau, 1996).

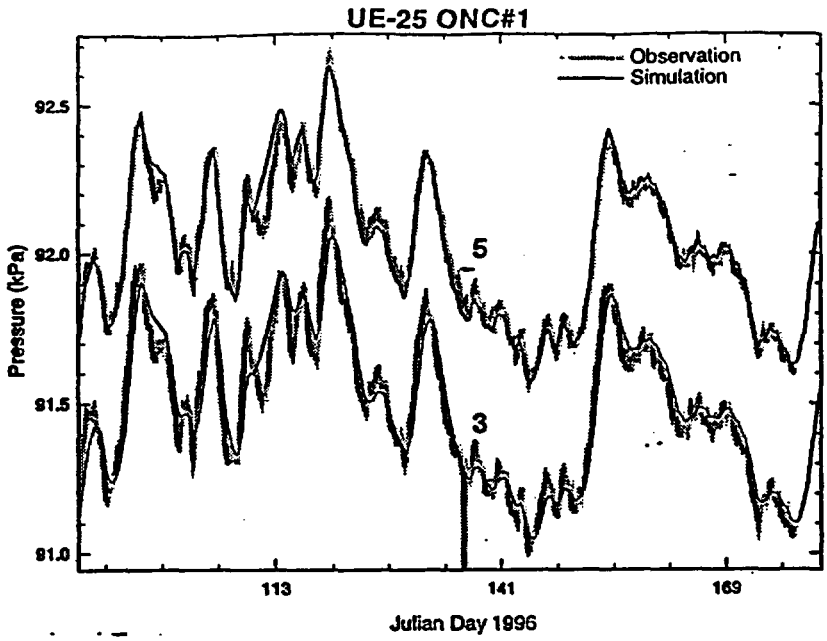

Figure 7.5. Matches between the three-dimensional simulation and observations in borehole ONC#1 at instrument stations 3 and 5. Observations provided by Nye County (Nye County, 1996).

7.1. Estimation of fault diffusivity

As discussed previously, the pneumatic response at some of the instrument stations in boreholes UZ#5, NRG-6, UZ-7a, and ONC#1 is due to the influence of faults. Each of the faults is modeled with a unique set of pneumatic diffusivity values. The pneumatic diffusivity estimated for the horizontal propagation of ESF interference to UZ#5 and NRG-6 is approximately 1500 m^2/s (k=600 d, n=0.2%). In contrast the diffusivity estimated for the vertical propagation of the surface barometric signal through the TSw portion of the Ghost Dance and Bow Ridge fault zones is estimated to be approximately 37 m^2/s (k=15 d, n= 0.2%) and 50 m^2/s (k=20 d, n=0.2%), respectively. Figure 7.1.1 shows the horizontal diffusivity estimated in the fault zones in the TSw as compared to the horizontal diffusivity estimated for the bulk tuff (fracture and matrix combined) in the TSw. Figure 7.1.2 shows the vertical diffusivity estimated in the fault zones in the TSw as compared to the vertical diffusivity estimated for the bulk tuff (fracture and matrix combined) in the TSw. Estimates for the Drill Hole Wash, UZ#5, and Ghost Dance faults are based on data that will be Q when submitted. Estimates for the Bow Ridge fault, though scientifically valid, are non-Q.

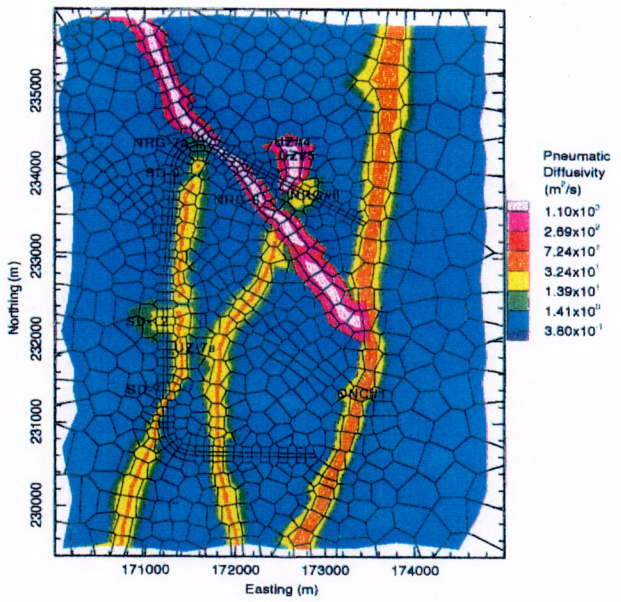

Figure 7.1.1. Plan view of horizontal pneumatic diffusivity distribution in the Topopah Spring hydrologic unit estimated by three-dimensional simulations. Pneumatic monitoring boreholes are indicated.

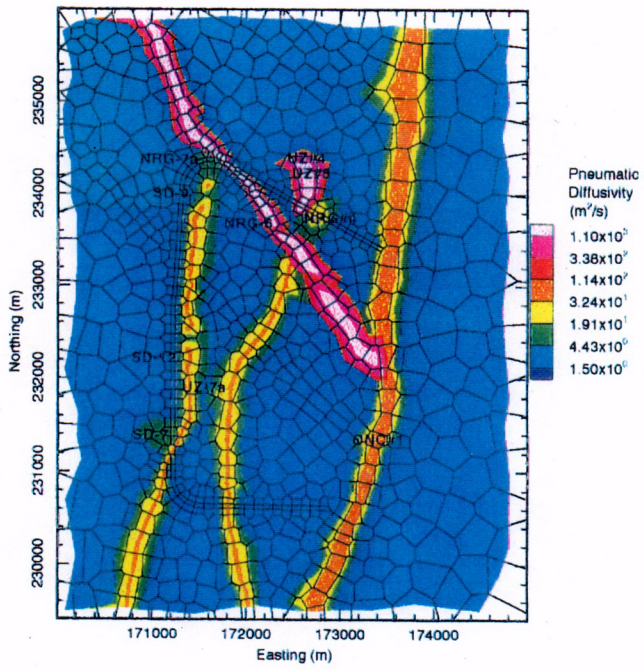

Figure 7.1.2. Plan view of vertical pneumatic diffusivity distribution in the Topopah Spring hydrologic unit estimated by three-dimensional simulations. Pneumatic monitoring boreholes are indicated.

C-01

Note that the vertical diffusivity estimated for the Ghost Dance and Bow Ridge faults is a much less sensitive parameter than the horizontal diffusivity estimated for the Drill Hole Wash and UZ#5 faults when matching pressure variations observed in the boreholes. Much more uncertainty is associated with the diffusivity estimated for the TSw portions of the Ghost Dance and Bow Ridge faults than with the estimates for the TSw portions of the Drill Hole Wash and UZ#5 faults. The uncertainty for the estimates has not been calculated. For lack of any means of characterization, the horizontal and vertical diffusivity parallel to the faults are given the same value.

For the Ghost Dance and Bow Ridge faults the vertical diffusivity through the PTn is the most sensitive parameter for matching the observed pressure response. At UZ#5 the fault PTn diffusivity is also the most sensitive parameter prior to ESF interference. In the Ghost Dance and Bow Ridge faults the estimated vertical diffusivity is 0.062 m^2/s (k=440 md, n=3.5%) and 0.0057 m^2/s (k=40 md, n=3.5%), respectively. In the Drill Hole Wash and UZ#5 faults the estimated vertical diffusivity is 0.028 m^2/s (k=800 md, n=3.5%) and is 0.11 m^2/s (k=200 md, n=3.5%), respectively. Figure 7.1.3 shows the estimated vertical diffusivity of the PTn portion of the fault zones compared to the estimated vertical diffusivity of the bulk tuff in the PTn. In the fault zone, one value of diffusivity is applied to the entire PTn. Outside the fault zone there are five sublayers in the PTn. In order to compare the two in Figure 7.1.3, the composite vertical diffusivity is calculated from the harmonic weighted mean of the PTn permeability values and the arithmetic weighted mean of porosity values. The means are weighted by layer thickness at each set of PTn grid elements in the three-dimensional model.

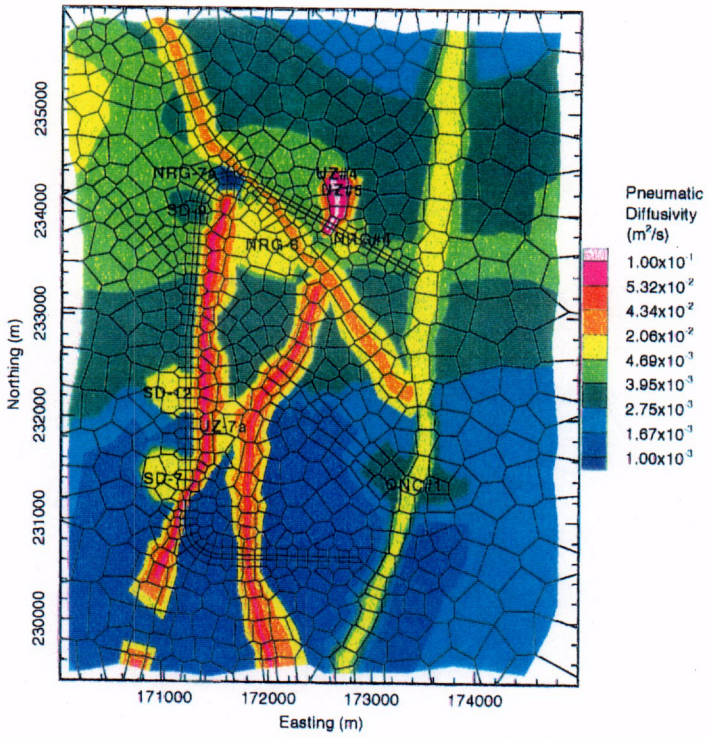

Figure 7.1.3. Plan view of composite vertical pneumatic diffusivity distribution in the Paintbrush non-welded hydrologic unit estimated by three-dimensional simulations. Note that diffusivity over the thickness of the PTn is calculated using the harmonic, weighted mean of permeability and the arithmetic, weighted mean of porosity. Pneumatic monitoring boreholes are indicated.

7.2. Estimates of PTn diffusivity

Prior to ESF interference, PTn diffusivity controls the pneumatic response in the PTn and below. For the three-dimensional simulation the composite vertical diffusivity of the PTn is varied in order to match pneumatic response in the TSw. Pneumatic response in the PTn was only roughly matched. Because of the coarseness of the three-dimensional model (necessary to model a large domain), exact instrument station elevation could not be simulated. In the PTn this proved to be a problem because of the large contrast in diffusivity between PTn sub-layers. For this reason, good matches were not pursued for pneumatic response recorded in PTn instrument stations. In general the ratios of diffusivity between sub-layers determined from one and two-dimensional simulations were retained in the three-dimensional simulation.

Figure 7.1.3 shows the variation in the composite vertical pneumatic diffusivity of the PTn estimated with the three-dimensional simulation. The variation is a function of not only the zones near the boreholes but also the thickness

C-02

of PTn sub-layers relative to the composite thickness of the PTn. For instance, the Tpy and Tpp make up more than half of the PTn thickness in the northern portion of Yucca Mountain but pinch out in the southern portion. Figure 7.2.1 shows a cross section of the PTn from the three-dimensional model grid along the north ramp and main drift of the ESF. Variation horizontally across the mountain and vertically within the PTn is shown. The presence of the Tpy and Tpp is also evident where higher diffusivity layers are shown.

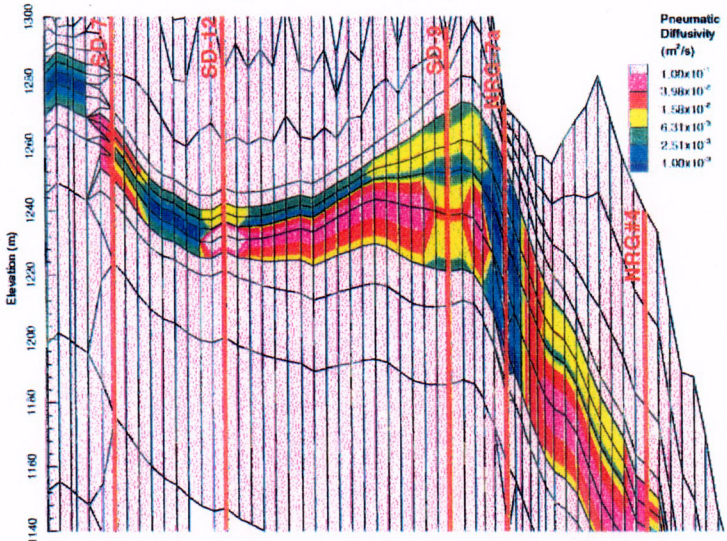

Figure 7.2.1. Vertical section along the north ramp and main drift of the ESF showing vertical diffusivity structure in the PTn. Note that diffusivity is contoured from node centers with one node center per layer, thus layer thickness is not represented in the contours. Location of pneumatic monitoring boreholes near ESF are shown. Horizontal axis (distance along ESF) is not to scale.

8. Blind predictions performed in cooperation with the USGS

During the course of this investigation periodic blind predictions of pneumatic response were made in cooperation with the USGS. Several sets of observations of time varying pneumatic pressure were received during the course of this investigation. These data sets represented from three to six months of data collection at various instrumented boreholes. The initial data set for any one borehole was used to calibrate simulations of that borehole. Subsequent data sets for previously calibrated borehole simulations were made available by first sending only the barometric signal (recorded at the surface). The barometric signal was used to simulate the pneumatic response in the borehole as a prediction of the observations not yet received. These predictions were forwarded to the USGS before the observations from the underground instrument stations were sent to LBNL.

This process was conducted with one-dimensional simulations of NRG-6 and NRG-7a, and two-dimensional simulations of UZ#5, NRG-6, NRG-7a, SD-

C-03

12, and UZ-7a. Predictions of SD-12 was not truly blind because the borehole only came on line at the end of 1995. The first data set for calibration was received in March, 1996. The first half of the data set was used for calibration, while the second half was used for comparison to the predictions. Figures 6.2.1.1 through 6.2.5.3 show the calibration period for the two-dimensional simulations and indicate the period over which predictions were made. Figures 6.2.4.1 through 6.2.5.3 also show a comparison of the predictions to observations at boreholes UZ-7a and SD-12. Figures 8.1 through 8.3 show comparisons of the predictions for selected instrument stations in boreholes UZ#5, NRG-6 and NRG-7a to observations. The comparison of predictions to observations is generally good.

The ability of the calibrated model to accurately predict pneumatic response is important to note. Correct predictions indicate that the calibrated model is capturing the pneumatic behavior of Yucca Mountain. Estimated pneumatic diffusivity can then be used to model the behavior of the mountain for transport of gaseos phase radionuclides and with altered conditions such as heat loading. Continued prediction of the pneumatic response is also important. If future predictions and observations do not agree, that may indicate a potential deficiency in the model to be corrected.

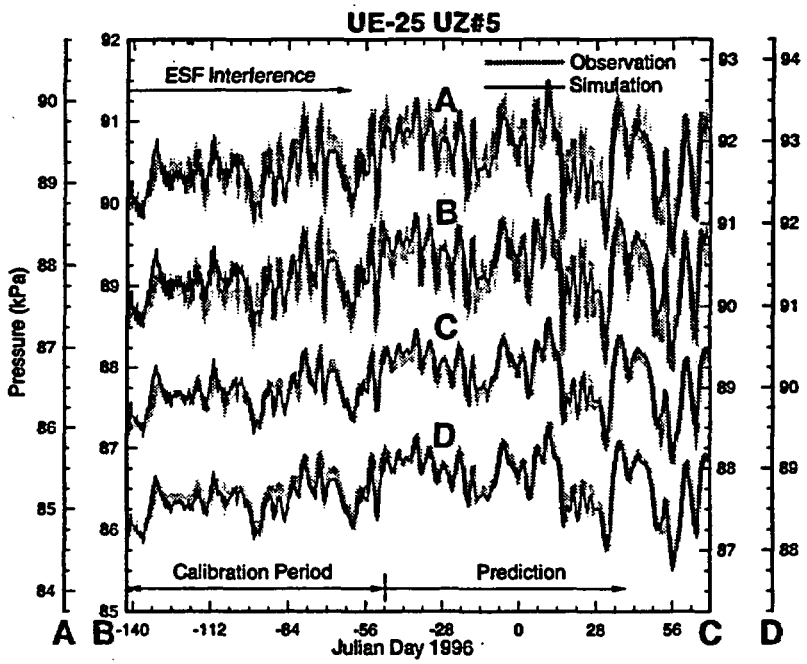

Figure 8.1. Comparison of predictions to observations at UZ#5 using a two-dimensional simulation. Predictions and observations for instrument stations A, B, C and D, below and in the lower section of the PTn, are shown. These stations are shown because they respond most strongly to ESF interference. Observations provided by the USGS (Rousseau, 1996).

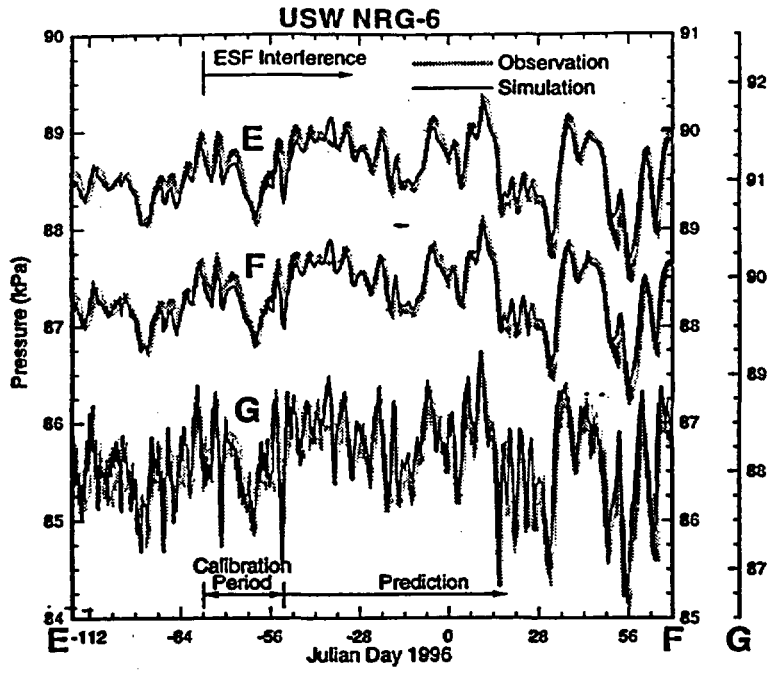

Figure 8.2. Comparison of predictions to observations at NRG-6 using a two-dimensional simulation. Predictions and observations for instrument stations E, F and G, below, within, and above the PTn, are shown. Observations provided by the USGS (Rousseau, 1996).

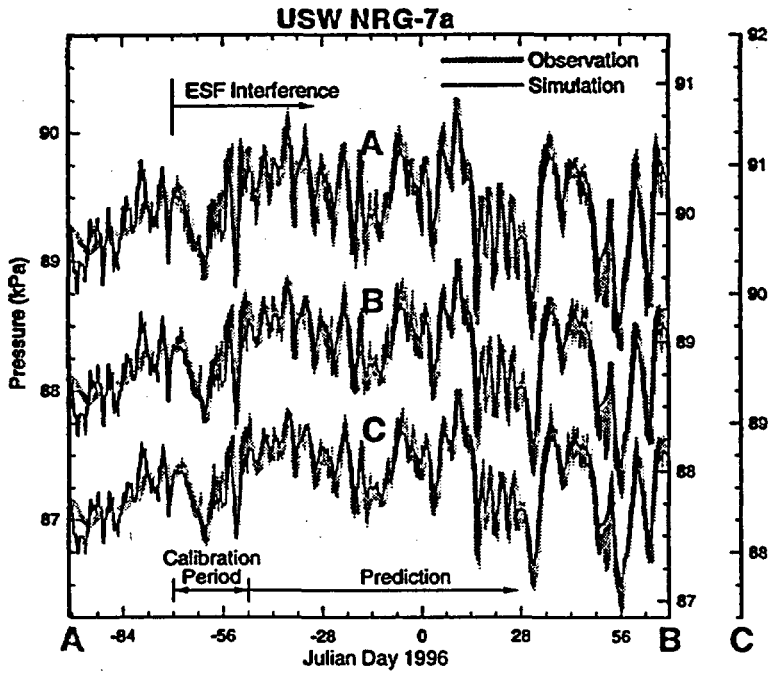

Figure 8.3. Comparison of predictions to observations at NRG-7a using a two-dimensional simulation. Predictions and observations for instrument stations A, B and C, all in the TSw, are shown. These stations are selected because varying response to ESF interference is observed at them. Observations provided by the USGS (Rousseau, 1996).

9. Pneumatic characterization implications for faults

Fault interference appears to contribute to pneumatic response in several boreholes at Yucca Mountain. UZ#4/5 appear to be influenced by an imbricate fault, NRG-6 by the Drill Hole Wash Fault and UZ-7a and SD-12 by the Ghost Dance Fault Zone.

These faults can be categorized into either NW trending strike-slip faults or N to NE trending normal faults. The normal faults can be further subdivided into those with large or small offsets.

The imbricate fault at UZ#4/5, if it is consistent with the other imbricate faults along the North Ramp, is a normal fault with a minor offset of less than 10 m. The thickness of the PTn in this area (> 80 m) means that the fault will not bring the bottom of the PTn on the upthrown foot wall above the top of the PTn in the downthrown hanging wall. Pneumatic response in UZ#4/5, prior to ESF interference, does not suggest, by itself, a fast pneumatic pathway through the PTn. However, comparison of estimated pneumatic thickness and logged thickness of the PTn at all pneumatic boreholes, based on a single value of effective PTn gas diffusivity, shows a poor correlation at UZ#4/5 (see section 5.3). The estimated pneumatic thickness is half of the logged thickness. Estimated gas diffusivity in the PTn at UZ#4/5 is high in comparison to other boreholes. This suggests a partial or weak fast pneumatic pathway through the PTn at UZ#4/5.

With the onset of ESF interference a strong pneumatic response is observed at UZ#4/5. The boreholes are located 400 to 500 m from the ESF. Horizontal gas diffusivity between the ESF and UZ#4/5 in the TSw is estimated, in three-dimensional simulations, to be more than 3.5 orders of magnitude higher than the bulk horizontal gas diffusivity of the TSw (estimated at NRG-7a). This suggests a significant fast pneumatic pathway along the imbricate fault in the TSw between the ESF and the boreholes.

There are two possible explanations for the different behavior of the fault in the PTn and the TSw. Movement by a fault should induce significant fracturing in the densely welded, brittle, TSw but less fracturing in the non to partially welded, more plastic PTn. The difference in the degree of fracturing would create a contrast in pneumatic diffusivity. It would also be possible to create the diffusivity contrast with higher saturation in PTn portion of the fault zone. The two factors may also work together. Smaller fractures in the PTn are likely to be at a higher saturation than the larger fractures in the TSw.

NRG-6 appears to respond to ESF interference via the Drill Hole Wash Fault. Data taken prior to ESF interference indicates that the fault does not act as a fast pneumatic pathway through the PTn, or if it does, the effect is not observed at NRG-6, approximately 100 m from the fault. Apparent pneumatic thickness and estimated diffusivity of the PTn correlate well with other bore-

holes. The Drill Hole Wash Fault is a strike-slip feature and produces little or no vertical offset of the strata. Estimated pneumatic diffusivity of the Drill Hole Wash Fault in the TSw between the ESF and 100 m from the borehole is estimated, in three-dimensional simulations, to be 3.5 orders of magnitude larger than the bulk horizontal diffusivity of the TSw.

A plausible explanation for the different pneumatic behavior of the fault in the PTn and the TSw is similar to the explanation for the imbricate fault at UZ#4/5. Less fracturing and higher saturation in the PTn lead to less of a contrast between fault diffusivity and bulk diffusivity than in the TSw.

The Ghost Dance Fault Zone is a series of north trending faults in a zone more than 300 m wide. Mapping by Spengler et al. (1994) ...suggest a total width of the Ghost Dance fault system of nearly 366 m... The largest total vertical offset across the zone is approximately 100 m. UZ-7a is located in the Ghost Dance Fault Zone and shows only minor attenuation of the pneumatic signal in the fault zone through the PTn. The PTn at UZ-7a is approximately 20 m thick. Outside the fault zone, in the TSw, the pneumatic response is more consistent with attenuation of the pneumatic signal through the PTn as shown in section 5.3. However, the apparent pneumatic thickness and the estimated diffusivity of the intact PTn suggest that the Ghost Dance Fault zone acts as a fast pneumatic pathway through the PTn. The pneumatic response within the fault zone, above, within and below the PTn, does show increased attenuation of the surface signal as it passes through the section of the fault in the PTn as compared to those sections in the TCw and the TSw. Like the two faults discussed above, decreased fracturing and increased saturation in the fault at the PTn can explain the lower apparent gas diffusivity in the PTn.

The estimated diffusivity in the TSw portion of the Ghost Dance fault zone is much lower than in the other two characterized faults. It is only 2 orders of magnitude greater than the TSw bulk horizontal diffusivity, 1.5 orders of magnitude less than the other two faults. Note that in this fault, the diffusivity is characterized by data which represent vertical pneumatic signal propagation. In the Drill Hole Wash fault and the imbricate fault at UZ#5, the pneumatic signal is propagated horizontally through the zone. The Ghost Dance fault zone is also characterized as a much wider fault zone, with multiple fault planes and brechiated zones (at least at the surface) (Spengler et al., 1994). The Drill Hole Wash fault and the imbricate fault at UZ#5 are interpreted as narrow fault zones at their intersection with the ESF in the TSw (Day et al., 1996; Rousseau and Patterson, 1996b). The differences in fracturing associated with the faults may also account for some differences in characterization.

Generally the faults that have been characterized by pneumatics show larger diffusivity than unfaulted tuffs. The effect of the PTn is to lower the diffusivity of the fault as it does in the rest of the mountain. In the densely welded TSw fault diffusivity is high, apparently allowing pneumatic signals from the

ESF to propagate 600 m or more. These conclusions are based on data which will be Q when submitted. Non-Q data from ONC#1, charaterizing the Bow Ridge fault, supports the conclusions about the Ghost Dance fault.

10. Pneumatic characterization implications for the Paintbrush non-welded hydrologic unit

The Paintbrush non-welded hydrologic unit (PTn) has been recognized as a layer which impedes pneumatic flow between the Tiva Canyon unit (TCw) at the surface of the mountain and the Topopah Spring unit (TSw) below the PTn (Lu et al., 1991, Ahlers et al., 1995, Rousseau and Patterson, 1996a, Kwicklis, 1996). Early efforts to characterize this layer led to the recognition that five pneumatic sub-layers appeared to be necessary in models of the PTn in order to properly simulate the pneumatic response observed in the PTn (Ahlers et al., 1995). These sub-layers are, from top to bottom,

1) the non-welded based of the Tiva Canyon member and the pre-Tiva Canyon bedded tuff (Tpcpv1 and Tpbt4)
2) the Yucca Mountain tuff (Tpy)
3) the pre-Yucca Mountain bedded tuff (Tpbt3)
4) the Pah Canyon tuff (Tpp)
5) the pre-Pah Canyon bedded tuff and the non-welded top of the Topopah Spring member (Tpbt2 and Tptrv3).

The major pneumatic distiction between these sub-layers appears to be degree of welding and resultant fracturing. Sub-layers 1, 3 and 5 above are characterized as non-welded with minor amounts of fracturing, if any. Sub-layers 2 and 4 are characterized as variably welded and fractured. The fracturing of the Tpy and Tpp increases their pneumatic permeability compared to the other PTn sub-layers. The estimated permeability difference between the Tpy and Tpp and the non-welded sub-layers is zero to two orders of magnitude. The variable welding and fracturing of the Tpy and Tpp in Yucca Mountain is attributed to their large variation in thickness from the north to south in Yucca Mountain. In the northern portions of Yucca Mountain the Tpy is 20 m thick or more and the Tpp is 40 m or more thick. In the southern portion of Yucca Mountain both sub-layers appear to pinch out (Moyer et al., 1995). The entire thickness of the PTn is over 80 m in the north and less than 20m in the south. Because the Tpy and Tpp make up variable portions of the PTn and have higher permeability than the other PTn sub-layers it is important to model them as separate layers.

Figure 7.1.3 shows the composite vertical diffusivity of the PTn layer as estimated by the three-dimensional simulation. Note that in the northern portion of the model the composite diffusivity is higher than in the southern portion of the model. This is due to the Tpy and Tpp making up a larger portion of the PTn in the north. In the southern portion it is only the lower permeability, non-welded

sub-layers, 1, 3 and 5 from above, that form the PTn. This skewing of the composite vertical diffusivity of the PTn is also evident in the one-dimensional joint inversion of nine boreholes described in section 5.3. As shown in Figures 5.3.1, 5.3.2 and 5.3.3 six boreholes that best characterize the PTn form a skewed line when true PTn thickness is plotted versus estimated hydrologic thickness. The skewing of this line is attributable to the variable portion of the PTn occupied by the Tpy and Tpp.

11. Density driven flow simulated at UZ-6 and UZ-6s

Since the flow at UZ-6 and UZ-6s is assumed to be mainly due to a density gradient across the west slope of Yucca Mountain (Weeks, 1987), it is assumed that most of the flow will be parallel to the slope (perpendicular to the crest). For this reason, a two-dimensional model aligned perpendicular to the crest is considered to be sufficient to capture the important aspects of the flow. The model is a cross section of the mountain from west to east through UZ-6 and UZ-6s (see Figure 11.1).

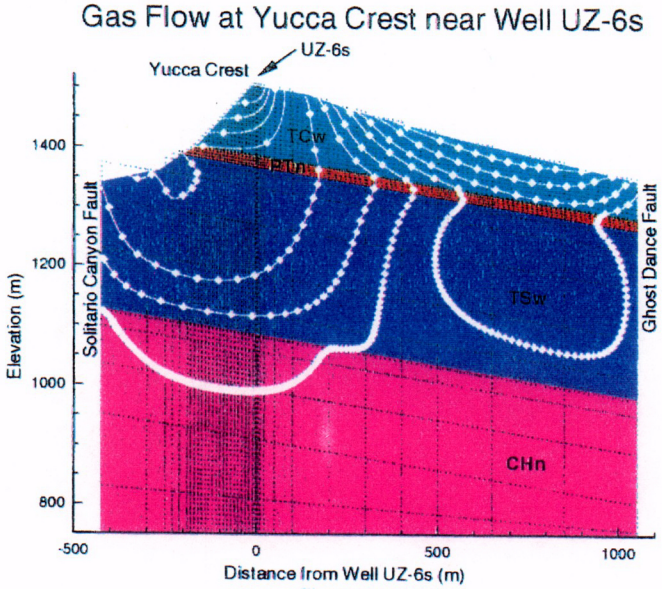

Figure 11.1. UZ-6s two-dimensional model showing gas travel times. There is a 250 year travel time between each mark on the gas flow streamlines.

The area of interest for this simulation is at Yucca Crest, mainly in the TCw, as this is where most of the data from UZ-6 and UZ-6s were taken. The surface of the mountain is the upper boundary of the model and the water table is a natural lower boundary. Both upper and lower boundaries are modeled as time-invariant pressure and temperature boundaries. The lateral boundaries need to be set far enough from the area of interest so that they do not significantly affect the simulation there. Since fault characteristics at Yucca Mountain are not well

C-04

known, the Solitario Canyon Fault and the Ghost Dance Fault are seen as natural lateral boundaries. The lateral boundaries are modeled as no-flow.

Gridding of the model is also dictated by the area of interest in the TCw at Yucca Crest. Vertical gridding is finer in the TCw in the upper portion of the model. In the lower portion of the model, vertical gridding is coarser and generally follows the geologic layering and gridding of the 3-D site-scale model (Wittwer et al., 1995). The horizontal gridding is finest near Yucca Crest and coarsest at the lateral boundaries. Temperature and pressure data from Yucca Crest (Thorstenson et al., 1989) are used to determine temperature and pressure boundary conditions at the atmospheric boundary. The temperature lower on the mountain is calculated using an assumption of 1C of temperature increase with every 100 meters of elevation loss (Kwicklis and Lu, 1994). The pressure on the mountain is calculated assuming gas static conditions in the atmosphere and a water vapor mass fraction corresponding to 20% relative humidity at Yucca Crest. The lower boundary temperature is based on temperature measurements at the water table (Ahlers et al., 1995). The lower boundary pressure is calculated assuming gas static conditions between the average top elevation and the bottom and 100% relative humidity everywhere in the mountain.

In order to simulate the two-phase conditions in the mountain, the model is used to calculate a steady-state saturation profile with 0.1 mm of infiltration per year as well as a steady-state geothermal gradient. Rock properties used in the model, including permeability, porosity, van Genuchten parameters, and thermal properties are taken from Wittwer et al. (1995). In the simulation, bulk fracture permeability in the welded layers is 10 darcy, and in the nonwelded layers the matrix permeability is 0.1 to 0.05 darcy which gives a gas permeability contrast between welded and nonwelded layers of 100 to 200 times. The multiphase, integrated finite difference numerical simulator, TOUGH2 (Pruess, 1991), is used for all flow and gas static calculations.

Gas flow can be evaluated once steady-state liquid conditions are reached because the simulation time necessary for reaching steady-state water saturation profiles is much longer than is needed to establish steady-state gas flow. Gas flow patterns and gas travel times from the atmosphere both meet the expectations of the data and the conceptual model. Stream lines of gas flow (see Figure 11.1) show that there is a distinct flow cell in the TCw. Air in this flow cell enters low on the sides of the mountain and exits high at the crest. Travel times through this flow cell are shown by the model to be approximately 300 years along the Solitario Canyon to Yucca Crest streamlines (see Figure 11.1). The PTn partially separates flow in the TCw from flow in the TSw. Travel times in the TSw are approximately 10000 years. The travel times are sensitive to both permeability and porosity. Because the model is mainly constructed to simulate flow in the TCw, flow patterns and travel times for the TSw may not be accurate.

In order to gain more information from the simulation for comparison to the data, borehole UZ-6s is included in the model. The borehole is simulated using an equivalent porous medium model with the dimensions of the elements the same as the borehole itself. The equivalent permeability of the borehole elements is calculated using a pipe flow approximation assuming a constant flow rate through the pipe and a roughness of the pipe. This gives a permeability which is correct only for the specified flow rate. Because of this, flows less than the assumed flow will be reduced even further.

Flow in the borehole is first evaluated with yearly average atmospheric temperature conditions. At the crest, this is a temperature of 15C (Thorstenson et al., 1989). Flow from the borehole is about 0.002 m/s once steady-state conditions are established in the borehole. The borehole flow is also evaluated under average winter atmospheric conditions, which is a crest temperature of 3C (Thorstenson et al., 1989). Borehole flow is increased with winter atmospheric conditions to 0.014 m/s. The simulation of gas flow in Yucca Mountain at boreholes UZ-6 and UZ-6s gave results that show less gas flow than the data suggest. Gas age data show travel times of less than 100 years for the TCw and less than 10000 years for the TSw. The simulation predicts longer travel times in both the TCw and the TSw. Data from borehole UZ-6s show flows averaging 3 m/s during the winter months. Model flow predictions at UZ-6s show flows 200 times less than this. In both cases, the simulation predicted flows in the mountain that are smaller than the data indicate. This suggests that the simulation uses permeabilities that are too low, that well bore modeling may not be accurate, that lateral boundary conditions may not be correct, or that there are other important driving forces for gas flow, such as wind and barometric pumping that are not considered in this simulation.

12. ESF moisture balance simulations

The presence of the ESF and the associated drilling operations perturb the ambient liquid saturation distribution near the tunnel. Water used to cool the drill head and spraying of the tunnel walls are two sources of water that can imbibe into the tunnel wall through rock fractures and matrix. Ponding of water on the tunnel floor may infiltrate through fractures. In contrast, when the relative humidity in the tunnel is lowered by ventilation, water vapor will flux into the tunnel from the surrounding rock. The potential influence of these processes on liquid saturation near the ESF and induced transport of fluids and isotopes must be assessed in order to properly interpret sampling of fluids and isotopes from the tunnel wall. This section describes initial numerical simulations of tunnel wall imbibition and drying aimed at addressing these issues.

12.1. Tunnel Ventilation Studies

The moisture flow in the vicinity of the ESF due to ventilation of the tunnel was investigated using a two-dimensional vertical mesh. Simulation of gravity, capillary and pressure driven evolution of saturation was carried using TOUGH-2 (Pruess, 1991).

12.1.1 The Radial Mesh.

An integrated finite difference mesh was constructed around the ESF. Concentric rings, divided into sectors, are placed near the ESF. It is necessary to divide the rings into sectors so that gravity can be included in the simulation. Away from the ESF, the rings are deformed so that the outer boundary of the mesh is square. Beginning with the known ESF radius of 3.81 m, several combinations of thickness and number of radial rings as well as number of sectors were investigated. The outer radius was selected to be sufficiently large such that that constant outer boundary conditions were maintained. The mesh described here consists of 16 sectors and a gradually increasing element thickness from 0.5 m to 100 m, extending to a total radius of 130.81 m. Beyond this radius 8 sectors were used with element thickness of 200 m, with a final transition to rectangular elements for a total radial extension of 450 m. A total of 438 elements were used in this model.

12.1.2 Natural State Simulation

In order to carry out ventilation studies, steady-state (natural state) conditions within the simulated domain were computed. The water table conditions with a liquid saturation nearly 1.0, a fixed pressure of 1.1 bar and a temperature of 25.8 C was maintained at the bottom of the model. An infiltration rate equivalent to 1 mm/year was maintained at the top. Uniform material properties, relative permeability and capillary pressure functions corresponding to Topopah Spring layer 3 from Wittwer et al. (1995) were used. Using initial conditions everywhere of .95 liquid saturation, 25 C and 1.0 bar pressure, steady-state saturation and pressure distribution was computed. After a simulated time of about .5 million years the computed steady-state pressure distribution is static and the saturation distribution is uniform. These steady-state conditions were assigned as initial conditions for the ventilation studies. Imbibition of construction water is not included in this simulation.

12.1.3 Ventilation Simulations

Explicit simulation of the tunnel ventilation process requires a knowledge of flowing air humidity, as well as the air flowrates. Since measurements of air humidity within the ventilated tunnel had not been made at the time of this study, a relative humidity that gives a reasonable initial capillary pressure within the tunnel boundary element was used. The relationship between capillary pressure and relative humidity was obtained from Kelvins equation (Hillel, 1980),

$$P_c = \frac{\ln(H)\rho RT}{M_w} \qquad (12.1.3.1)$$

where P_c = capillary pressure (Pa), ρ = water density (kg/m3), H = relative humidity, R = universal gas constant (J/mole K), T = temperature (K), and M_w = molecular weight of water (kg/mole).

From this relationship, an initial relative humidity of 95% gives a capillary pressure of 93.5 kPa. Based on the capillary pressure vs saturations function used in the model, this capillary pressure corresponds to a saturation that falls within the expected range for Topopah Spring layer 3. The design air flow rate of the ESF of 217.55 m^3/hour was used. For the tunnel ventilation this air contained moisture equivalent to a humidity of 95%. This quantity of moist air with enthalpy corresponding to a temperature of 16 C was injected into a dummy element connected to the tunnel element. Fluid was extracted from another dummy element connected to the tunnel, using the deliverability option in TOUGH2 against a back pressure of 90 kPa. This pressure is consistent with the assumption that initial tunnel pressure is below formation pressure at the start of the ventilation process and is equivalent to the estimated atmospheric pressure at 1100 masl, the elevation of the tunnel used in this study. Uniform material properties as in the natural state model were used except for the tunnel itself. For the tunnel material properties were assigned so that the ventilated air and water vapor would flow easily through the tunnel element.

Simulation was performed using the design ventilation rate and with the initial conditions calculated by the natural state simulation. Infiltration was maintained at the same rate as in natural state simulations. The distribution of saturation in the vicinity of the tunnel was computed for simulated times of 1, 10, 50, 100, 500, and 1000 years (Figures 12.1.3.1 through 12.1.3.6). The average change in saturation within the first layer of the tunnel is shown in Figure 12.1.3.7. The change in liquid inflow (from the tunnel walls) is shown in Figure 12.1.3.8.

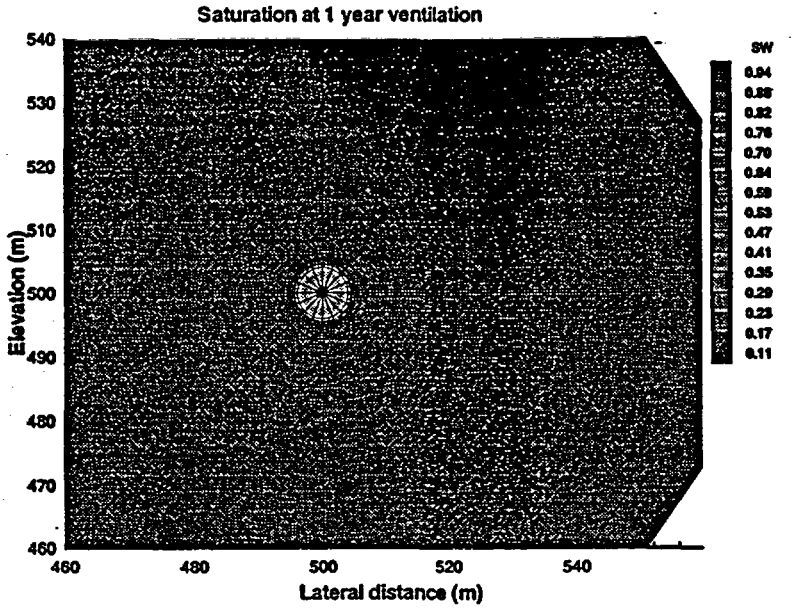

Figure 12.1.3.1. Saturation after one year of simulated ventilation.

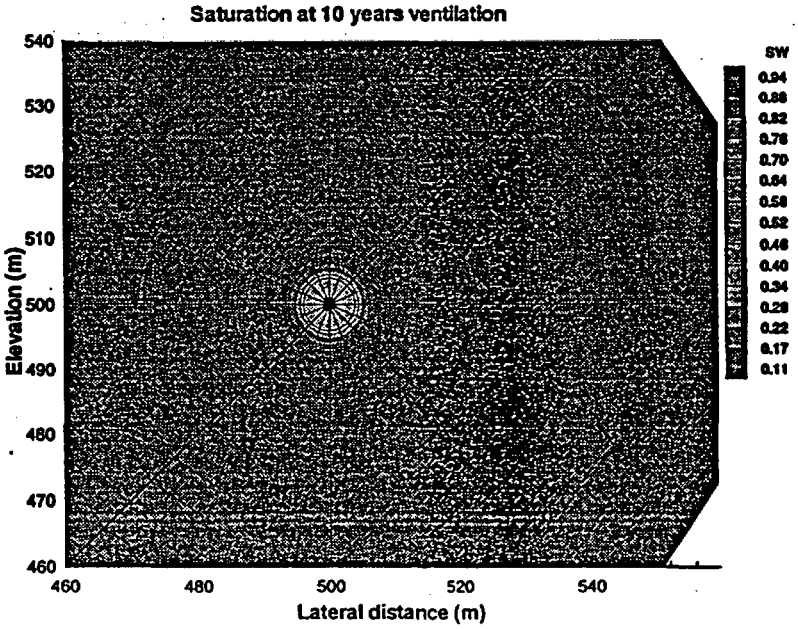

Figure 12.1.3.2. Saturation after ten years of simulated ventilation.

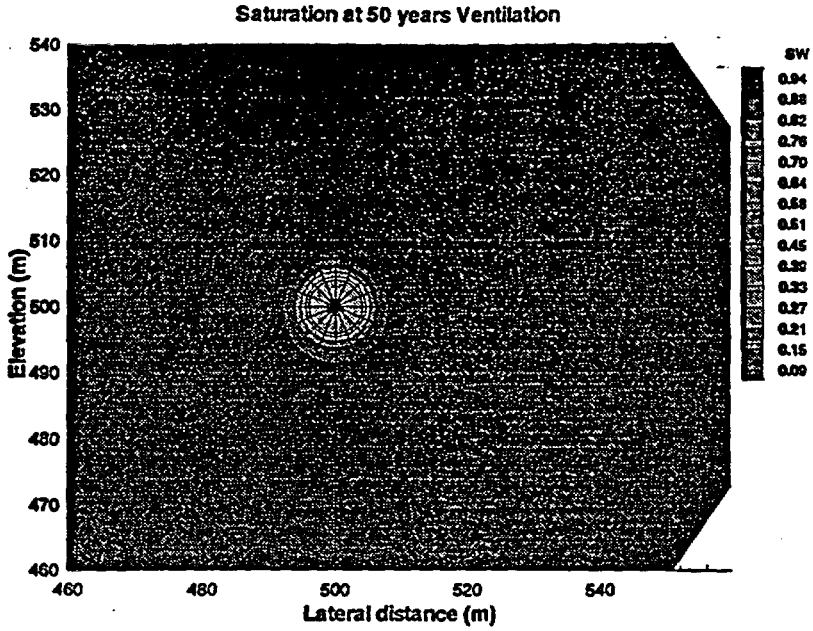

Figure 12.1.3.3. Saturation after 50 years of simulated ventilation.

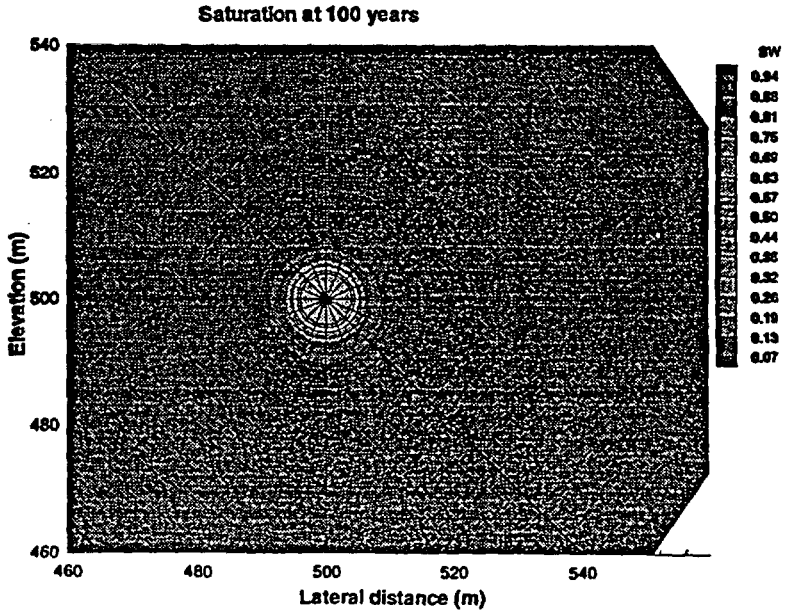

Figure 12.1.3.4. Saturation after 100 years of simulated ventilation.

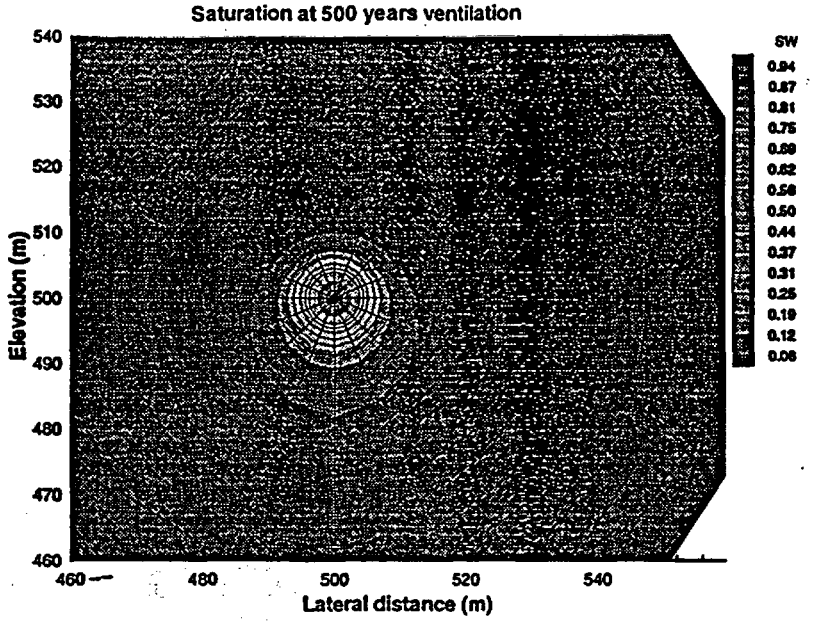

Figure 12.1.3.5. Saturation after 500 years of simulated ventilation.

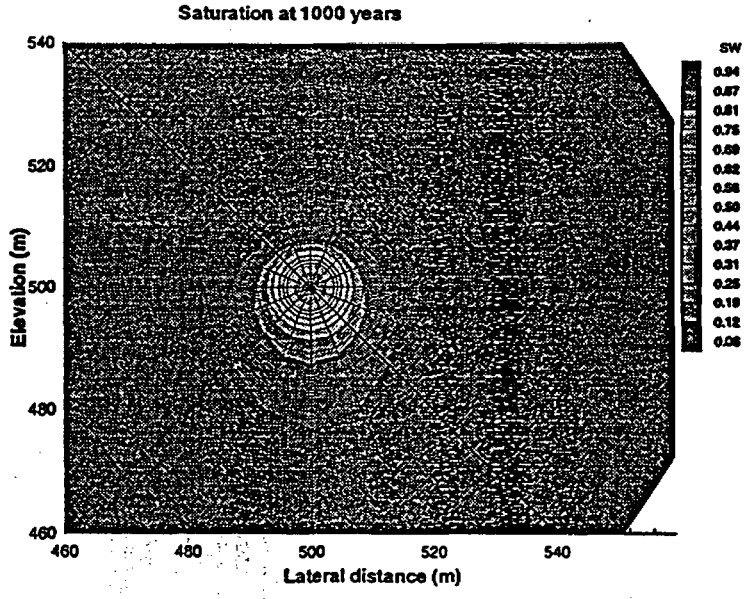

Figure 12.1.3.6. Saturation after 1000 years of simulated ventilation.

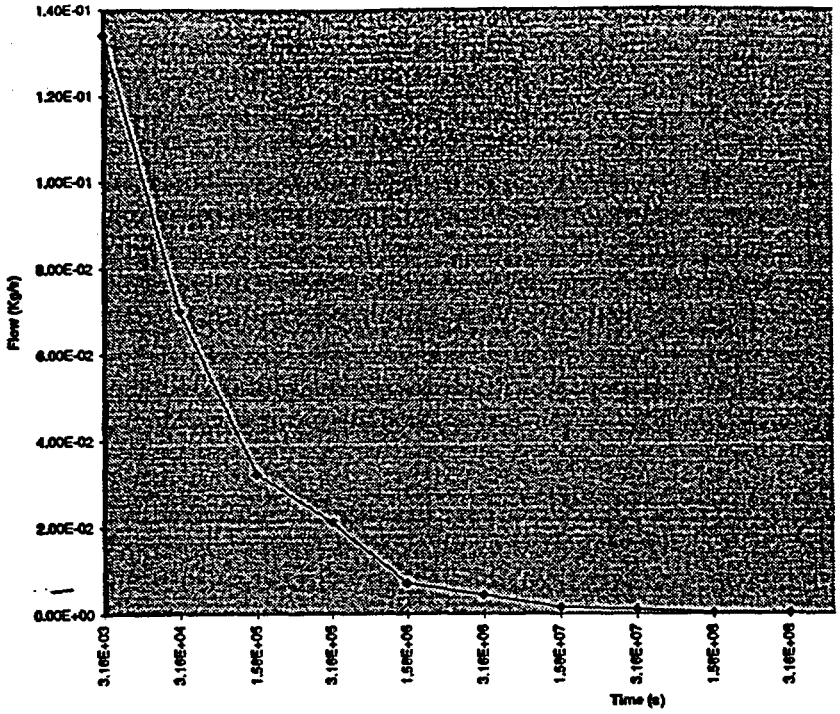

Figure 12.1.3.7. Saturation vs. time near the tunnel wall.

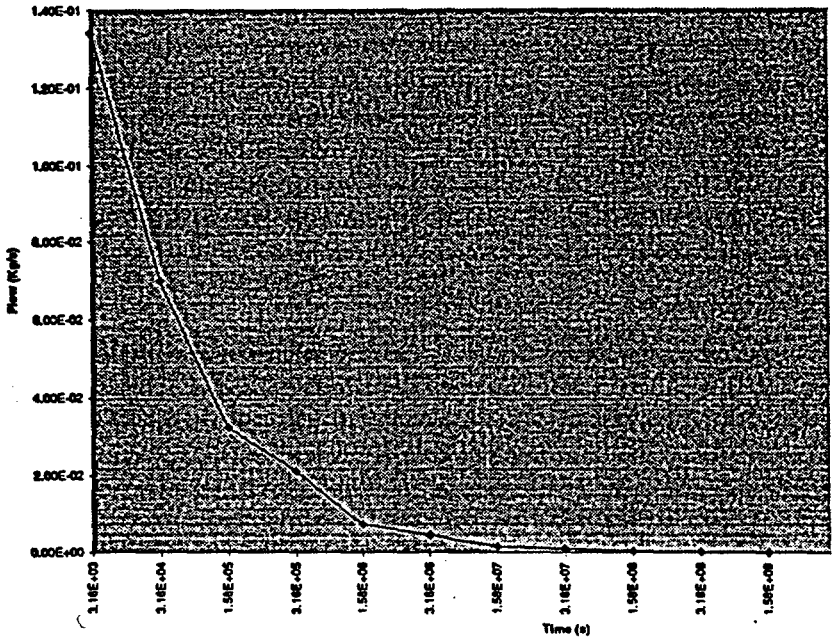

Figure 12.1.3.8. Flow of liquid into the tunnel.

The distribution of saturation (Figures 12.1.3.1 through 12.1.3.6) shows extensive drying of the tunnel during the simulated period. The liquid saturation within tunnel, however, increases during the first year of ventilation to a maximum of 0.057 (Figure 12.1.3.7). Beyond 1 year the liquid saturation declines continuously. After 100 years the desaturated zone around the tunnel extends to about 10 meters (Figure 12.1.3.4) and to about 20 meters after 1000 years (Figure 12.1.3.6). Beyond 500 years the liquid saturation at the walls of the tunnel is practically zero (Figure 12.1.3.7). The combination of gravity and infiltration from the top makes the de-saturation more extensive at the bottom of the tunnel than at the top. The total fluid flux into the tunnel through the tunnel walls (Figure 12.1.3.7) declines rapidly to a near steady state flow in about 10-15 days. The liquid inflow declines to near zero in about one year (Figure 12.1.3.8) as liquid saturation in the first layer of tunnel elements drops to near zero indicating that any liquid at the tunnel wall is instantaneously vaporized.

12.2. Dual-Permeability Simulations of ESF Ventilation

A second simulation is performed with a dual permeability model (as opposed to the effective continuum model used for simulation presented in section 12.1). The dual permeability formulation is chosen in order to simulate differential transient behavior in the fracture and matrix continua. Imbibition of construction water into the walls of the ESF is considered in this simulation. Boundary conditions at the tunnel wall are changed from the previous simulation to reflect data gathered in the ESF.

12.2.1. Modeling Approach and Methodology

The model described here is designed to simulate imbibition of construction water into the tunnel wall and subsequent drying of the tunnel wall due to ventilation. In order to capture the fractured structure of the rock, the MINC (Multiple INteracting Continua; Pruess and Narasimhan, 1985) method is employed in the TOUGH2 simulations. Specifically, a dual-continua mesh is used, wherein an element representing the fracture continuum is connected to each matrix continuum element. The flow area, volume, and porosity of these elements are appropriately scaled to preserve the intended fracture spacing and fracture porosity. Fluxes from fracture to fracture, matrix to fracture, and matrix to matrix are enabled. This formulation is known as the "dual-permeability" model (Pruess, 1991).

A one-dimensional radial mesh is used. The model represents a unit thickness cross section of rock that is perpendicular to the tunnel. The tunnel face element is 1 mm wide, and element widths increase logarithmically away from the wall. The furthest element is 90 m from the tunnel face. Transients do not reach this outer boundary for the time scales modeled. Gravity effects are not considered. This exclusion does do not impose significant errors since the simulated transients only persist several meters from the tunnel over the time scales considered. The model properties are homogeneous and represent the Topopah Spring unit. The capillary pressure and associated relative permeability functions correspond to the Topopah Spring unit 5, as it appears in the (Bandurraga

et al., 1996b). The van Genuchten model (1980) is used to describe the effective saturation to capillary pressure relationship. The parameters used are listed below (Table 12.2.1.1). The MINC mesh captures the effective properties of a matrix and two fracture sets with average spacing of 0.74 m and porosity of 0.00275 (Wilson, et al.,, 1994).

Table 12.2.1.1.
Parameters of the Van Genuchten module.

Parameter	Matrix Continuum	Fracture Continuum
k[m^2]	1.79×10^{-19}	4.97×10^{-11}
m	0.22	0.23
a	3.5×10^{-6}	1.2×10^{-3}

Typical matrix saturation within the Topopah Spring unit is on the order of 95%. Imbibition of construction water is modeled by applying a 99% matrix saturation and corresponding equilibrium fracture saturation boundary condition to the tunnel element. This formulation assumes fractures at the tunnel face do not maintain near saturated conditions, which is reasonable for imbibition resulting from spraying of construction water. Drying, due to ventilation, is simulated by applying a constant relative humidity (R.H.) to the tunnel element. The corresponding boundary saturation is calculated using Kelvins equation (12.1.3.1) and the rock capillary pressure functions.

12.2.3. Simulation and Results

This simulation first considers imbibition of construction water into the tunnel wall. The tunnel wall is initally at 25 C and 95% matrix saturation. Average temperature inside the tunnel is approximately 21C (Wang, 1996), and this is the temperature assigned to the tunnel boundary. Matirx saturation of the tunnel boundary condition is 99%. Figures 12.2.3.1 and 12.2.3.2 show the saturation profile with time in the matrix and fracture continua. The difference in maximum and minimum saturation on the y-axis is the same in both figures. The relative changes in fracture and matrix saturations are therefore apparent. Imbibition is simulated up to sixty days, as after this time, the TBM and related operations have advanced hundreds of meters. The cumulative fracture and matrix imbibition over 60 days is 0.18 m^3 per meter of tunnel length. As of July 13, 1996, the tunnel was 5979 m long, and a total of 35,456 m^3 of water had been used (Weekly drilling report, LA-EES-13-FO-07-96-004). An average water usage based on these values is 5.9 m^3/m. It is impossible to determine how much of this water was sprayed onto tunnel walls or allowed to seep into the rock at the drill face. Only 3% of this average is imbibed over 60 days in the model. Incorporation of tunnel ponding into the tunnel model and sensitivity analysis is required to bound an estimate of total water introduced into the mountain by drilling operations.

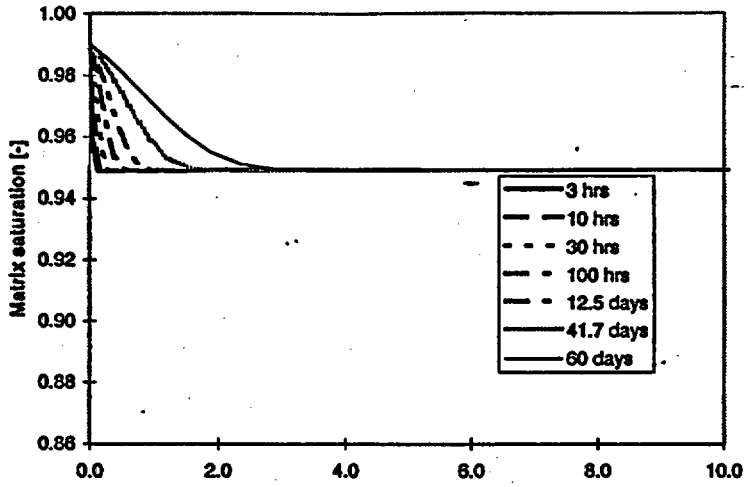

Figure 12.2.3.1. Matrix continuum saturation profile with time for 99% matrix saturation tunnel wall boundary condition. Matrix originally 95% saturated.

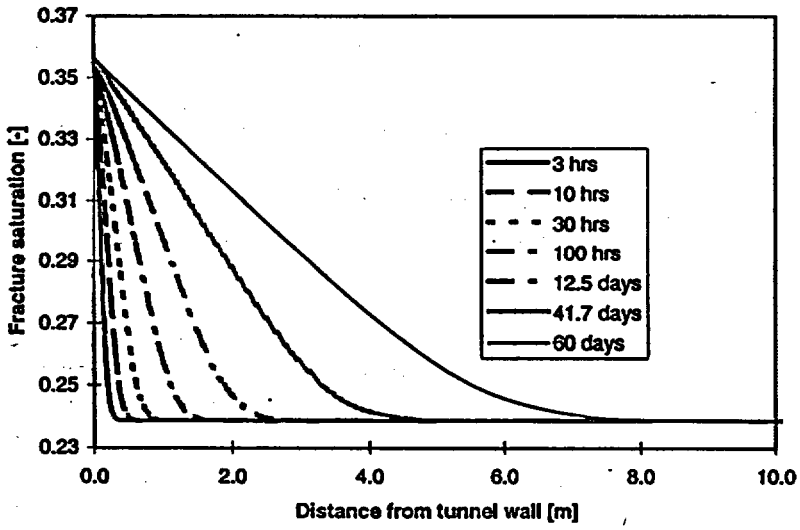

Figure 12.2.3.2. Fracture continuum saturation profile with time for 99% matrix saturation tunnel wall boundary condition. Matrix originally 95% saturated.

We chose 12.5 days as a representative time scale over which a section of tunnel wall is exposed to imbibition conditions. Figure 12.2.3.1 shows the wetting front advanced 1 m in the matrix and approximately 2 m in the fractures over this time.

A second simulation considers tunnel wall drying due to ventilation. Saturation conditions after 12.5 days of imbibition, as shown in Figures 12.2.3.1 and 12.2.3.2, were used as initial conditions. The average relative humidity in the tunnel on time scales greater than 1 week is approximately 50% (Wang, 1996). This value was used as the boundary condition in the drying simulations. Kelvins equation (12.1.3.1) is used to calculate the corresponding constant saturations at the tunnel wall, as described earlier. These saturations are 24.4% and 95.4% for the fracture and matrix continua, respectively. Note that these values are very similar to the ambient values. For the drying simulations, a constant gas pressure of 89.9 kPa is set in the tunnel. The initial gas pressure in the surrounding elements is 90 kPa. This condition is set in order to allow vapor transport to the tunnel. Figures 12.2.3.3 and 12.2.3.4 show the saturation profiles with time for this drying condition. The simulation shows that in 60 days near ambient conditions are reached. The simulation suggests that elevated liquid saturations and contamination from construction water produced by application of construction water to the tunnel walls may be minimal and relatively short-term.

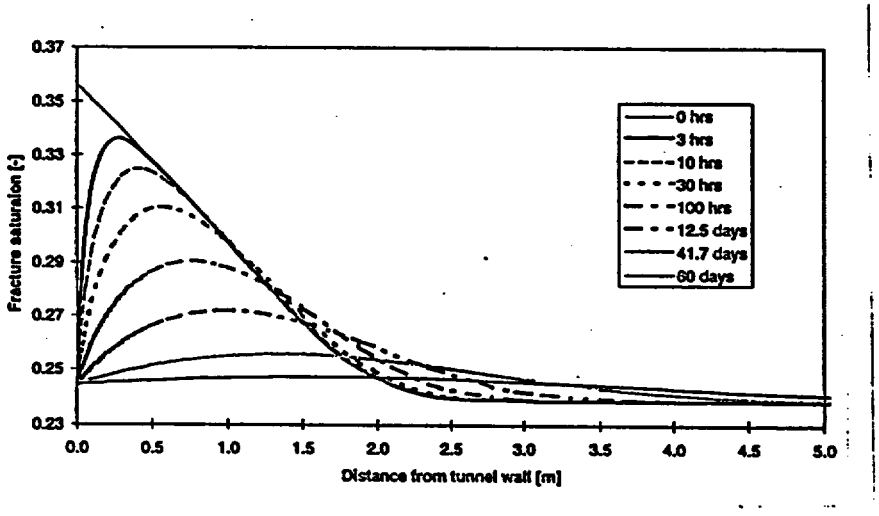

Figure 12.2.3.3. Matrix continuum saturation profile with time for tunnel wall drying conditions at R.H. = 50%.

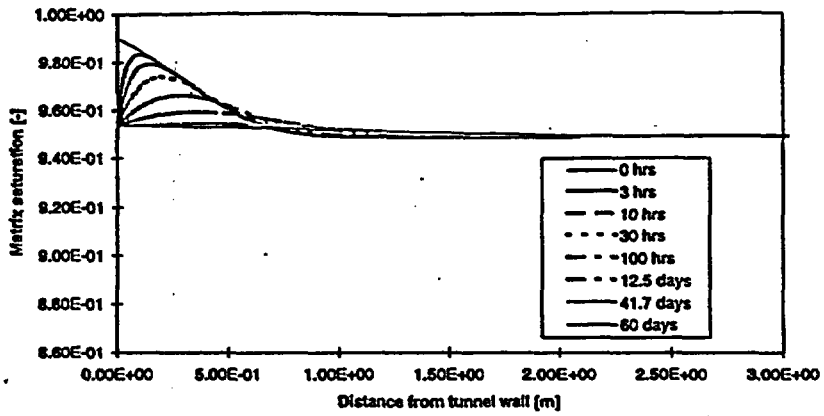

Figure 12.2.3.4. Fracture continuum saturation profile with time for tunnel wall drying conditions at R.H. = 50%.

12.2.5. Summary and Conclusions

This section described initial simulations of imbibition of construction water into the ESF tunnel wall and drying of the ESF tunnel wall due to ventilation. A dual-permeability model was used to represent the fractured structure of the Topopah Springs unit. Simulations considered imbibition into the tunnel face for 12.5 days, and then drying under constant tunnel relative humidity of 50%. Imbibition into an 95% originally saturated rock for 12.5 days produce a

wetting front that extends on the order of 1 m into the tunnel wall. The elevated saturation from imbibition of construction water returned to near ambient conditions after 60 days of tunnel ventilation. Future simulations should account for tunnel floor ponding, oscillating tunnel relative humidity, and consider differing rock properties in order to more exactly model potential effects of tunnel presence and operations on the moisture balance within the mountain.

13. Conclusions

Characterization of gas flow at Yucca Mountain, Nevada is important. Some radionuclides, that are produced by spent fuel, are present and can be transported in the gas phase. The thermal response of the system to heating from a repository depends significantly on gas circulation. Gas outflow may occur during heating from the repository, and near surface temperature change could alter the ecosystem.

In response to the NRC, the DOE initiated a pneumatic monitoring program. Boreholes are instrumented to monitor the pneumatic response in the subsurface to barometric pressure fluctuations at the surface of the mountain and in the ESF. Barometric pressure fluctuations occur due to daily changes in temperature and due to passing weather systems. Monitoring of pneumatic response to the surface signal allows estimation of vertical pneumatic diffusivity. With the response to the ESF signal also monitored, horizontal pneumatic diffusivity can also be estimated. Very good quality data has been obtained from boreholes instrumented and monitored by the USGS (Rousseau, 1995, Rousseau, 1996, Rousseau and Patterson, 1996a). Nye County has also instrumented and monitored boreholes (MET, 1995).

Successful data analysis has been performed with the unsaturated zone flow model. One and two-dimensional simulations are used as the first step of pneumatic characterization. Use of three-dimensional, site-scale simulations allows fully three-dimensional characterization. Blind predictions using recorded surface signals have been performed with calibrated simulations as an exercise to build confidence in the models. The pneumatic characterization has given much useful information about the diffusivity of fractures, effects of faults as pneumatic pathways, and the role of the PTn.

The objectives of this work are to

1) analyze the pneumatic data in order to determine pneumatic diffusivity,
2) determine the roles of faults with respect to pneumatics,
3) determine global gas flow patterns and characteristics at Yucca Mountain,
4) develop a predictive history for pneumatic response as a confidence building exercise, and

5) provide the basis for integrating the three-dimensional model of liquid flow in the unsaturated zone with a calibrated model of gas flow.

Conditions near the ESF due to tunnel ventilation are also investigated with respect to moisture flow from the tunnel walls.Estimates of pneumatic diffusivity, mainly for the PTn and the TSw, are provided in this report. Five layers in the PTn have been identified as being pneumatically important. The overall thickness of the PTn has been shown to control the pneumatic response in the TSw. In the TSw, both vertical and horizontal diffusivity have been estimated. Horizontal pneumatic diffusivity is estimated to be 5 times less than vertical pneumatic diffusivity in the TSw. Estimates of pneumatic permeability from air injection testing in the welded tuffs (LeCain, 1996b) show similar permeability ranges as estimated in this report.

Faults have been identified as fast pneumatic pathways in the PTn and the TSw. Faults have been observed to conduct pneumatic signals from the surface to the TSw and from the ESF to distant boreholes in the TSw. Estimation of pneumatic diffusivity in the faults gives values from one to 3.5 orders of magnitude higher than the estimated pneumatic diffusivity of the bulk tuffs (fractures and matrix combined). The faults have the same pneumatic structure as the rest of the mountain. Pneumatic diffusivity is higher where the faults penetrate welded units (TCw and TSw) and is lower where they penetrate the non-welded tuffs of the PTn.

Global gas flow patterns in and below the PTn have been shown to be dominated by the thickness of the PTn. Faults control the pneumatic response locally, but volumetric expansion below the PTn rapidly attenuates the influence of the fault away from the fault zone. Similarly, ESF interference in attenuated by volumetric expansion. Note that some boreholes far from the ESF record interference where a fault connects the borehole and the ESF.

Blind predictions performed with one and two-dimensional models have been very successful. Predictions have built confidence in the models of the pneumatic response of Yucca Mountain not only by matching the observed data well, but also by showing possible inadequacies in the model, such as ESF interference at NRG-6 via the Ghost Dance Fault.

These simulations and calibration have provided the first step toward integrating the model of the pneumatic response at Yucca Mountain with the model of unsaturated liquid flow at Yucca Mountain.

14. References

Advance Resources International, Inc., An analysis of air permeability testing in borehole UZ-16, Yucca Mountain, Nevada, prepared for the Nye County Nuclear Waste Repository Project Office, 1994.

Advance Resources International, Inc., An analysis of air permeability testing in borehole SD-12, Yucca Mountain, Nevada, prepared for the Nye County Nuclear Waste Repository Project Office, 1995.

Ahlers, C. F., T. M. Bandurraga, G. S. Bodvarsson, G. Chen, S. Finsterle, Y-S. Wu, Summary of model calibration and sensitivity studies using the LBNL/USGS three-dimensional unsaturated zone site-scale model, Yucca Mountain Project milestone 3GLM107M, LB092995312293.001, MOL.19960208.0091-0097, 1995,

Bandurraga, T. M., Geologic model development and vertical layering scheme for the numerical grid, in Development and calibration of the three-dimensional site-scale unsaturated zone model of Yucca Mountain, YMP Milestone OB02, 1996a.

Bandurraga, T. M., S. Finsterle, and G. S. Bodvarsson, Saturation and capillary pressure analysis, in Development and calibration of the three-dimensional site-scale unsaturated zone model of Yucca Mountain, YMP Milestone OB02, 1996b.

Day, W. C., D. Sweetkind, C. J. Potter, S. C. Beason, and R. W. Spengler, Structural setting of the north ramp of the exploratory studies facility, in Hydrogeology of the unsaturated zone, north ramp area of the Exploratory Studies Facility, Yucca Mountain, Nevada, Rousseau, J. P., E. M. Kwicklis, and C. Gillies eds., USGS WRI-96xxxx (preliminary), 1996.

Flint, L. E., Pneumatic properties derived from core analysis, in Hydrogeology of the unsaturated zone, north ramp area of the Exploratory Studies Facility, Yucca Mountain, Nevada, Rousseau, J. P., E. M. Kwicklis, and C. Gillies eds., USGS WRI-96xxxx (preliminary), 1996.

Finsterle, S., ITOUGH2 user's guide version 2.2, LBL-34581, MOL.19941026.0075, 1993.

Finsterle, S., T. M. Bandurraga, C. Doughty, and G. S. Bodvarsson, Simulation of coupled processes in a two-dimensional west-east cross-section of Yucca Mountain, Nevada, in Development and calibration of the three-dimensional site-scale unsaturated zone model of Yucca Mountain, YMP Milestone OB02, 1996.

Freeze, R. A. and J. A. Cherry, Groundwater, Prentice-Hall, HQS.19880517.1763, 1979.

Haukwa, C., et al., Grid Developement, in Calibration of the unsaturated zone model, YMP Milestone XXXXX, 1996.

Hillel, D., Fundamentals of soil physics, Academic Press, Inc., HQS.19880517.1776, 1980.

Kwicklis, E. M., Determination of pneumatic diffusivity, in Hydrogeology of the unsaturated zone, north ramp area of the Exploratory Studies Facility, Yucca Mountain, Nevada, Rousseau, J. P., E. M. Kwicklis, and C. Gillies eds., USGS WRI-96xxxx (preliminary), 1996.

LeCain, G. D. and J. N. Walker, Results of air-permeability testing in a vertical borehole at Yucca Mountain, Nevada, Proceedings of the Fifth Annual International Conference on High Level Radioactive Waste Management, pp. 2782-2788 , 1994.

LeCain, G. D., In-situ pneumatic testing of boreholes, in Hydrogeology of the unsaturated zone, north ramp area of the Exploratory Studies Facility, Yucca Mountain, Nevada, Rousseau, J. P., E. M. Kwicklis, and C. Gillies eds., USGS WRI-96xxxx (preliminary), 1996a.

LeCain, G. D., written communication from G. LeCain to G. Bodvarsson showing air permeability for boreholes USW NRG-6, USW NRG-7a, USW UZ-16, and USW SD-12, Yucca Mountain, Nevada, four (4) figures, US Geologic Survey, July 12, 1996b.

Moyer, T. C., J. K. Geslin, and L. E. Flint, Stratigraphic relations and hydrologic properties of the Paintbrush Tuff nonwelded (PTn) hydrologic unit, Yucca Mountain, Nevada, US Geologic Survey, Open-File Report 95-397, 1995.

Multimedia Environmental Technology, Inc., Interim report on results of instrumentation and monitoring of UE-25 ONC#1 and USW NRG-4 boreholes, Yucca Mountain, Nevada, prepared for the Nye County Nuclear Waste Repository Project Office, 1995.

Nye County Independent Scientific Investigation Program, Borehole UE-25 ONC#1 and USW NRG-4 Drilling and Instrumentation Report, Yucca Mountain, Nevada, Prepared for The Nye County Nuclear Waste Repository Project Office, 1995.

Pruess, K., TOUGH2 – a general purpose numerical simulator for multiphase fluid and heat flow, LBL-29400, NNA.19940202.0088, 1991.

Rousseau, J. P., M. Kurzmack, and A. Greengard, Results of prototype borehole instrumentation at the Hydrologic Research Facility, Area 25, NTS, Proceedings of the Fifth Annual International Conference on High Level Radioactive Waste Management, pp. 2764-2773, 1994.

Rousseau, J. P, C. L. Loskot, J. Kume, M. Kurzmack, N. D. Brian, K. Thomas, A. J. Greengard, In-situ borehole instrumentation and monitoring data for

USW NRG-7a and USW NRG-6, Yucca Mountain, Nye County, Nevada, 1995.

Rousseau, J. P. and G. L. Patterson, In-situ pneumatic-pressure response to atmospheric-pressure change, in Hydrogeology of the unsaturated zone, north ramp area of the Exploratory Studies Facility, Yucca Mountain, Nevada, Rousseau, J. P., E. M. Kwicklis, and C. Gillies eds., USGS WRI-96xxxx (preliminary), 1996a.

Rousseau, J. P. and G. L. Patterson, Effects of excavation of the north ramp on in-situ pneumatic-pressure measurements, in Hydrogeology of the unsaturated zone, north ramp area of the Exploratory Studies Facility, Yucca Mountain, Nevada, Rousseau, J. P., E. M. Kwicklis, and C. Gillies eds., USGS WRI-96xxxx (preliminary), 1996b.

Rousseau, J. P., Data transmittal of pneumatic pressure records from October 24, 1994 through July 14, 1996 for boreholes UE-25 UZ#4, UE-25 UZ#5, USW NRG-6, USW NRG-7a, USW SD-12, and USW UZ-7a, Yucca Mountain, Nevada, US Geologic Survey, July 15, 1996.

Shan, C., Analytical solutions for determining vertical air permeability in unsaturated soils, Water Resources Research, vol. 31, no. 9, pp. 2193-2200, September, 1995.

Simmons, A., Fracture coatings and fracture characteristics with implications for flow along fast pathways, in Development and calibration of the three-dimensional site-scale unsaturated zone model of Yucca Mountain, YMP Milestone OB02, 1996.

Spengler, R. W., C. A. Braun, R. M. Linden, L. G. Martin, D. M. Ross-Brown, R. L. Blackburn, Structural character of the Ghost Dance fault, Yucca Mountain, Nevada, High Level Radioactive Waste Management, pp. 653-659, 1993.

Thorstenson, D. C., E. P. Weeks, H. Haas, and J. C. Woodward, Physical and chemical characteristics of topographically affected airflow in an open borehole at Yucca Mountain, Nevada, Proceedings of the Topical Meeting on Nuclear Waste Isolation in the Unsaturated Zone, Focus '89, American Nuclear Society, Inc., pp. 256-270, GS930508312261.004, NNA.19900723.0196, 1990.

van Genuchten, M. Th., A closed-form equation for predicting the hydraulic conductivity of unsaturated soils, Soil Sci. Soc. Am. J., vol. 44, pp. 892-898, 1980.

Wilson, M. J., J. H. Gauthier, R. W. Barnard, G. E. Barr, J. A. Dockery, E. Dunn, R. R. Eaton, D. C. Guerin, N. Lu, M. J. Martinez, R. Nilson, C. A. Rautman, T. H. Robey, B. Ross, E. E. Ryder, A. R. Schenker, S. A. Shannon, L. H. Skinner, W. G. Halsey, J. D. Gansemer, L. C. Lewis, A. D. Lamont, I. R. Triay, A. Meijer, D. E. Morris, Total-system performance assessment for Yucca Moun-

tain – SNL second iteration (TSPA-1993), Sandia Report SAND93-2675, pp. 7-28, 7-30, 1994.

Wang, J., A. L. Flint, J. J. Nitao, D. A. Chesnut, P. Cook, N. G. W. Cook, B. Freifeld, L. E. Flint, K. Ellet, A. J. Mitchell, E. F. Homuth, G. J. Griego, J. A. Cerny, C. L. Johnson, Ventilation-induced rock drying in the ESF, YMP Milestone TR31K6M, 1996.

Weeks, E. P., Does the wind blow through Yucca Mountain?, Proceedings of workshop V: Flow and transport through unsaturated fractured rock - related to high-level radioactive waste disposal, eds. Evans, D. D. And T. J. Nicholson, pp. 43-53, GS940608312261.003, MOL.19941006.0033, 1993.

Weeks, E. P., Effects of topography on gas flow in unsaturated fractured rocks: concepts and observation, in Flow and transport through unsaturated rocks, eds. Evans and Nicholson, AGU Geophysical Monograph 42, pp. 165-170, HQS19880517.3214, 1987.

Weeks, E. P., Field determination of vertical permeability to air in the unsaturated zone, Geological Survey Professional Paper 1051, 1978.

Yang, I. C., C. A. Peters, and D. C. Thorstenson, Carbon isotopic data from test hole USW UZ-1, Yucca Mountain, Nevada, Proceedings of the Fourth Annual International Conference on High Level Radioactive Waste Management, pp. 401-406, GJ930508312271.021, NNA.19900403.0266, 1993.

Yang, I. C.; H. H. Haas, E. P. Weeks, and D. C. Thorstenson, Analysis of gaseous-phase stable and radioactive isotopes in the unsaturated zone, Yucca Mountain, Nevada, Proceedings of the NWWA Conference on Characterization and Monitoring of the Vadose (Unsaturated) Zone, pp. 488-506, 1985.

Yang, I.C., Flow and transport through unsaturated rock – data from two test holes, Yucca Mountain, Nevada, Proceedings of the Third Annual International Conference on High Level Radioactive Waste Management, pp. 732-737, 1992.